Heinrich Heine
Universität
Düsseldorf

Development of Laser Driven Proton Sources and Their Medical Applications

Inaugural-Dissertation

zur Erlangung des Doktorgrades der
Mathematisch-Naturwissenschaftlichen Fakultät der
Heinrich-Heine-Universität Düsseldorf

vorgelegt von

Jens Ehlert
aus Paderborn

Düsseldorf, März 2022

aus dem Institut für Laser- und Plasmaphysik
und der Klinik für Hämatologie, Onkologie und Klinische Immunologie
der Heinrich-Heine-Universität Düsseldorf

Gedruckt mit der Genehmigung der Mathematisch-Naturwissenschaftlichen Fakultät
der Heinrich-Heine-Universität Düsseldorf

Berichterstatter:

1. Prof. Dr. Oswald Willi

2. Prof. Dr. Rainer Haas

Tag der mündlichen Prüfung: 24. Juni 2022

Contents

List of Abbreviations

AFM	atomic force microscopy
APF	3‘(p-aminophenyl) fluorescein
ASE	amplified spontaneous emission
ATI	above-threshold ionization
BSI	barrier suppression ionization
CAP	conventionally accelerated proton
CD34+ cells	normal hematopoietic CD34+ progenitor and stem cells
CPA	chirped pulse amplification
DCF	2‘,7‘-dichlorofluorescein
DCFH-DA	2‘,7‘-dichlorodihydrofluorescein diacetate
DMF	dimethylformamid
DMSO	dimethylsulfoxid
DNA	Deoxyribonucleic acid
DSB	DNA double strand break
f	focal length
FACS	fluorescence-activated cell sorting
FC	flow cytometry
FITC	fluorescein isothiocyanate
fps	frames per second
FSC	forward-scattered light
FWHM	full width at half maximum
g	gravitational acceleration 9.8 m/s^2

IP	image plate
LAP	laser accelerated proton
LET	linear energy transfer
MACS	magnetic-activated cell sorting
MCP	micro-channel plate
MPI	multi-photon ionisation
NA	numerical aperture
PBMC	peripheral blood mononuclear cell
PBS	phosphate-buffered saline
PI	propidium iodide
PM	plasma mirror
PSL	photostimulated luminescence
QUB	Queen's University Belfast
RBE	relative biological effectiveness
RCF	radiochromic film
RIN	RNA integrity number
RNA	ribonucleic acid
ROS	reactive oxygen species
RT	radiotherapy
SD	standard deviation
SRIM	the stopping and range of ions in matter
SSB	DNA single strand break
SSC	side-scattered light
TNSA	target normal sheath acceleration
TOF	time of flight
TPS	Thomson parabola spectrometer
WD	working distance
WPE	Westdeutsches Protonentherapiezentrum Essen
XPW	cross polarized wave

Abstract

Particle therapy or hadron therapy is an important pillar of cancer treatment and offers patients advantages due to a better dose distribution compared to photons or electrons. For the necessary particle acceleration, mostly of protons or carbon ions, either a cyclotron or a synchrotron has been used so far. As a result of the expensive infrastructure required, extensive radiation protection measures and continuous maintenance, the share of patients treated by hadron therapy in radiation therapy is relatively small. A comparatively new approach is acceleration by using short, high-intensity laser pulses. Even if this approach still needs some development work, among other things to generate the particle energies necessary for radiotherapy, the irradiation is interesting due to the completely different beam characteristics, as much higher dose rates are achieved compared to conventional irradiation.

This thesis deals with laser accelerated protons (LAPs) for *in vitro* irradiation. For this purpose, different aspects are considered, from the structure of the irradiation chamber with the diagnostics used and partly directly connected, to the modification of the proton radiation by using two timed laser pulses, and to the performance and evaluation of cell experiments.

The experiments were carried out at the Arcturus laser facility of the Heinrich Heine University Düsseldorf. For proton acceleration, a laser pulse ($\approx 10^{20}$ W/cm^2 and 30 fs) hits a thin titanium foil in a vacuum chamber. A resulting static electric field on the back of the foil causes ion acceleration during the so-called TNSA process. The fast ions pass through a magnetic chicane, which defines the energy range and separates them from other types of radiation (electrons, X-rays), so that only protons hit the cell sample at the selected setting. It is shown that the cells in the sample holder find viable conditions (e.g. cell division of a HeLa cell). During irradiation, the cells can be examined with a fluorescence microscope developed in the course of this work. Immunofluorescence images of this are shown.

In the following chapter, the proton pulse modifications are examined. For this purpose, both laser beams are focused on the titanium foil. With spatially overlap-

ping interaction points the proton flux triggered by the second laser pulse decreases rapidly, so that this configuration is not effective for the desired pulse delays. With a spatial separation of 1 mm, a longer pulse delay can be set. Additionally, the modification of the proton pulses with timed pulsed electric fields was investigated. Compared to the static magnetic fields this arrangement potentially improves the flexibility of the irradiation platform.

The last experimental chapter deals with the cell irradiation experiments. Gene expression analysis of LAP irradiated CD34+ stem cells showed that radiation-specific genes are expressed, such as GADD45A. Furthermore, various immunofluorescence measurements were carried out both microscopically and via FACS. The most interesting result here is the different fluorescence intensity of two reactive oxygen species (ROS) markers when comparing X-rays and LAPs, indicating that oxidative stress is lower at the high dose rate of LAPs.

Zusammenfassung

Die Partikel- oder Hadronentherapie ist eine wichtige Säule der Krebsbehandlung und bietet Patienten Vorteile aufgrund einer besseren Dosisverteilung im Vergleich zur Bestrahlung mit Photonen oder Elektronen. Für die nötige Teilchenbeschleunigung von zumeist Protonen oder Kohlenstoffionen wird bisher entweder ein Zyklotron oder ein Synchrotron verwendet. Infolge der benötigten teuren Infrastruktur, umfangreichen Strahlenschutzmaßnahmen und einer kontinuierlichen Wartung hat die Hadronentherapie jedoch nur einen verhältnismäßig kleinen Patientenanteil in der Strahlentherapie. Einen vergleichsweise neuen Ansatz stellt die Beschleunigung mittels kurzer hochintensiver Laserpulse dar. Auch wenn dieser Ansatz noch etwas Entwicklungsarbeit benötigt, unter anderem um die für die Strahlentherapie nötigen Teilchenenergien zu erzeugen, ist die Strahlung aufgrund der gänzlich anderen Strahlcharakteristik interessant, da im Vergleich zur konventionellen Bestrahlung weit höhere Dosisleistungen erreicht werden.

Diese Arbeit befasst sich mit der Anwendung Laser-beschleunigter Protonen (LAPs) für die *in vitro* Bestrahlung. Hierfür werden unterschiedliche Aspekte berücksichtigt, von dem Aufbau der Bestrahlungskammer mit den verwendeten und zum Teil direkt angeschlossenen Diagnostiken, über die Modifikation der Protonenstrahlung durch die Verwendung zweier zeitlich aufeinander abgestimmter Laserpulse bis zu der Durchführung und Auswertung von Zellexperimenten.

Die Versuche wurden an der Arcturus Lasereinrichtung der Heinrich-Heine-Universität Düsseldorf durchgeführt. Für die Protonenbeschleunigung trifft ein Laserpuls ($\approx 10^{20}$ W/cm^2 und 30 fs) in einer Vakuumkammer auf eine dünne Titanfolie (5 µm). Durch ein resultierendes statisches elektrisches Feld auf der Folienrückseite kommt es zur Ionenbeschleunigung bei dem sogenannten TNSA Prozess. Die schnellen Ionen durchlaufen eine magnetische Schikane, wodurch der Energiebereich definiert wird und sie von anderen Strahlungsarten (Elektronen, Röntgenstrahlung) getrennt werden, so dass bei der gewählten Einstellung nur Protonen auf die Zellprobe treffen. Es wird gezeigt, dass die Zellen in dem Probenhalter vitale Bedin-

gungen vorfinden (z.B. Zellteilung einer HeLa Zelle). Während der Bestrahlung lassen sich die Zellen außerdem mit einem im Laufe dieser Arbeit entwickelten Fluoreszenzmikroskop untersuchen. Hiervon werden Immunfluoreszenzaufnahmen gezeigt.

Im darauffolgenden Teil der Arbeit wurden die Protonenpulsmodifikationen untersucht. Hierfür wurden beide Laserstrahlen auf die Titanfolie fokussiert. Bei räumlich überlappenden Interaktionspunkten nimmt der Protonenfluss, der durch den zweiten Laserpuls ausgelöst wird, schnell ab, sodass diese Konfiguration für die angestrebten Pulsverzögerungen nicht effizient ist. Bei einer räumlichen Separation von 1 mm lässt sich eine längere Pulsverzögerung einstellen. Außerdem wurde die Modifikation der Protonenpulse mit zeitlich gepulsten elektrischen Feldern untersucht. Im Vergleich zu den statischen Magnetfeldern verbessert diese Anordnung potenziell die Flexibilität der Bestrahlungsplattform.

Im letzten experimentellen Kapitel werden die Zellbestrahlungsversuche behandelt. Bei der Genexpressionsanalyse LAP bestrahlter CD34+ Stammzellen konnte gezeigt werden, dass strahlungsspezifische Gene exprimiert werden, wie beispielsweise GADD45A. Des Weiteren wurden verschiedene Immunfluoreszenzmessungen sowohl mikroskopisch als auch via FACS durchgeführt. Das interessanteste Ergebnis ist hier die unterschiedliche Fluoreszenzintensität zweier Marker für reaktive Sauerstoffspezies (ROS) beim Vergleich von Röntgenstrahlung und LAPs, die darauf hindeuten, dass der oxidative Stress bei der hohen Dosisleistung der LAPs geringer ausfällt.

1. Introduction and Motivation

Particle acceleration for proton therapy [1] is typically performed with cyclotrons. This requires an expensive infra-structure, extensive radiation protection measures and continuous maintenance. In the last decade, the FLASH effect became of high scientific and medical interest due to its potential in providing radiotherapy with reduced normal tissue toxicities compared to conventional radiotherapy [2, 3]. This effect is based on a significantly higher dose rate. First investigations on the FLASH proton beam therapy were conducted with a dose rate of up to 94 Gy/s in classical proton accelerators and also showed sparing of healthy cells while maintaining the same level of tumour control [4].

Another approach for delivering high dose rates employs laser accelerated proton bursts. In the area of LAPs, various groups [5–9] worldwide are presently investigating the radiobiological effects on single cells or cell layers. Even though this technique is still far from a clinical application, its major advantage is that owing to the principle of their generation, LAPs could provide inherently and without further modifications the high dose rates required for FLASH therapy.

Previous studies investigated in detail DNA double-strand breaks (DSBs) induced by LAPs[7]. The results indicate that the number of DSBs increases linearly with dose and the obtained yields are similar to those of conventionally accelerated protons (CAPs) at same dose level [6]. In contrast, initial studies show that the nitroxidative stress of cells exposed to LAPs is lower than in cells irradiated with CAPs [9].[1]

This leads to interesting questions from the physical side as well as from the medical-biological side, which are reflected in the structure of this work and presented schematically below.

[1] The introduction is in large parts identical with the article [10] published in the context of this work.

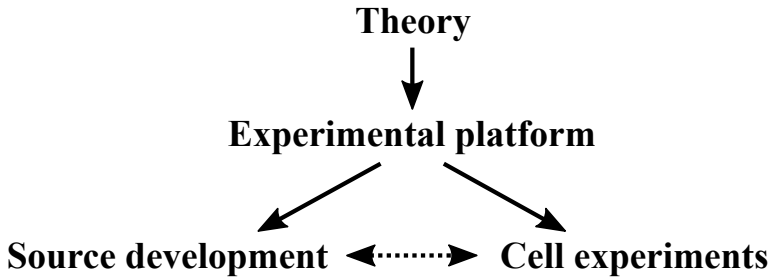

The theoretical fundamentals, both the physical and the medical-biological, are discussed in **Chapter 2**. The physical basics are composed of three parts, first the theory for the generation of ultrashort high intensity laser pulses, based on the chirped pulse amplification (CPA) technique, followed by the theory of the interaction between the laser pulse and the target leading to the proton acceleration. Last but not least, the energy release of the accelerated protons in the irradiated sample and the dose distribution is discussed. In the following part regarding the medical-biological basics, the human cell is discussed as the foundation for the later shown medical experiments. Subsequently the basics of radiobiology are examined.

In **Chapter 3** the CPA dual beam Ti:Sa laser system Arcturus is described in more detail since this system provides the basis for proton acceleration and the laser parameters have a direct impact on the proton spectrum. Next, the diagnostics used for the measurements of the accelerated protons are outlined. Afterwards, the experimental platform developed to investigate the radiobiological effects of LAPs on human cells is described. The platform includes a vacuum chamber housing, the focusing parabola of the laser beam, an innovative tape target driver for multiple shots, a dipole magnet system for the energy-dependent dispersion of protons and ports for cell exposures and absorbed radiation dose measurements. In addition, an epifluorescence microscope was developed for live cell imaging during irradiation, which enables to investigate radiation damages on different time scales and via several imaging modes. The microscope can operate at a multi-Hz frequency and has a theoretical spatial and temporal resolution of 260 nm and 129 µs, respectively. First test images are shown.

Chapter 4 deals with the radiation source and its modifications. These are on the one hand the results of the modification of the proton pulse by a second laser pulse. The timing of the laser pulses was varied in the range of a few nanoseconds and then they were either superimposed on the target or had a spatial separation of one millimetre. On the other hand the proton beam was modified by a pulsed electric field to influence a specific proton energy range.

The last experimental **Chapter 5** describes the performed cell irradiation experiments. Long time recordings on HeLa cells were carried out to demonstrate that cells proliferate well over times longer than those required for a typical experiment. Furthermore, several biological proof of principle tests were carried out to demonstrate the functionality of the platform. Subsequently, experiments were conducted to investigate the specific effects of LAPs on cells.

DSBs were investigated as the most relevant form of DNA damages induced by ionising radiation by detecting proteins on DSB sites on chromatin. Additional markers were also used to investigate other cell properties. Oxidative stress resulting from the irradiation was investigated with various markers, as it is held responsible for a large proportion of cellular damage in radiotherapy. Here, preliminary measurements showed lower oxidative stress for LAPs in contrast to X-ray irradiation. Last but not least, gene expression analyses of irradiated and non-irradiated haematopoietic stem cells were performed and the evaluation showed that different radiation damage response pathways were activated.

Finally, the experimental results are summarised in **Chapter 6** and an outlook on possible improvements of the setup and on further interesting experiments is given.

1.1. Role of the Author

The author was involved in the performance of all the experiments shown, as well as in their evaluation (unless explicitly stated otherwise). Of course, such experiments cannot be carried out alone. The people who contributed to this work are named in the chapter **Acknowledgement**. If I have forgotten anyone, I apologise.

The scientific background necessary for understanding the work has been summarised by the author in chapter **2. Theoretical Background**.

The following chapter **3. Laser System, Diagnostics and Radiation Chamber** describes the experimental setup. The basic experimental structure was already established, but it was optimised or extended in the course of this work, for example by a fluorescence microscope, which was mainly set up and tested by the author. Furthermore, the author was closely involved in the trails of an improved tape target and a new temperature controlled cell flange.

In the two-beam experiments described in chapter **4. Source Development: Two Beam Configuration**, the author was actively involved in setting up, improving and carrying out the experiments, as well as in evaluating the results and

supervising the Masters' students.

In the last experimental part **5. Cell Irradiation Experiments**, the author was mainly responsible for the cell handling. This included cell culture, immunostaining, RNA purification, as well as microscopy and FACS measurements. The following evaluation was also mainly carried out by the author.

2. Theoretical Background

This work originated from a cooperation between the "Department of haematology, oncology and clinical immunology" - Prof. Dr. Rainer Haas and the "Laser and Plasma Physics" group - Prof. Dr. Oswald Willi. At its fundamentals, the research presented in this thesis addresses an interdisciplinary field of the LAP applications in cell irradiation and associated effects. Consequently, the basic principles of both fields are summarized bellow. First, the basic principles of laser and plasma physics are discussed and in the second part the biological characteristics of human cells are described. This is followed by a brief discussion of radiation biology.

2.1. Basic Principles of Laser and Plasma Physics

Ultrashort laser pulses are able to generate plasmas due to extreme electric field strengths, which can exceed the field strength of an atom at the Bohr radius by many orders of magnitude. If these pulses interact with a thin target it is possible to accelerate ions in a beam like fashion. In the following, the basics for the generation of such a laser pulse are briefly outlined, as well as the interaction with the target, which leads to the acceleration of ions.

2.1.1. Chirped Pulse Amplification

Theodore H. Maiman invented the laser by demonstrating population inversion and stimulated emission in the optical range (694,3 nm and 692,9 nm) with a ruby crystal [11]. Soon after the invention, laser intensities ramped up and reached a plateau given by the damage threshold. Therefore, the maximal laser intensities were mainly limited by the size of the laser components, until Gérard Mourou and Donna Strickland came up with the idea of chirped pulse amplification (CPA), which they demonstrated in the publication [12]. The basic idea is to extract a short laser pulse and reduce its intensity by stretching it in time. The stretched pulse is amplified and afterwards the pulse is compressed again to increase its intensity.

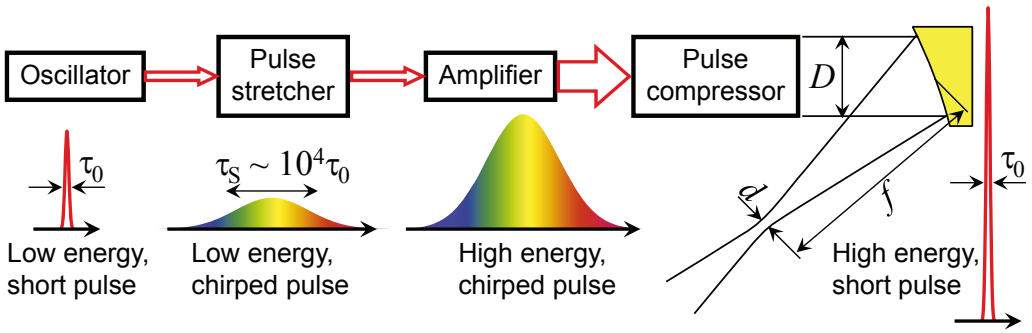

Figure 2.1.: The steps of CPA are shown schematically. From left to right: A single short pulse is extracted from an oscillator, which is stretched in time frequency dependent, resulting in a much longer chirped signal with a greatly reduced intensity. This pulse is amplified and the chirp is kept constant. In the compressor, the dispersive effects of the stretcher are reversed and the pulse is recompressed, which increases the intensity enormously. The pulse is focused by an off axis parabola (from [13]).

A schematic illustration can be found in figure 2.1. On the left a short pulse with the full width at half maximum (FWHM) duration τ_0 (commonly less than a few tens of femtoseconds) is shown. This pulse is stretched in time $\tau_s \sim 10^4\ \tau_0$ by letting it acquire a chirp. In the original work the chirp was acquired by dispersion, when sending the pulse through a long fibre. Due to group velocity dispersion in the fibre the red shifted part travels faster than the blue shifted part, as indicated by the rainbow colour of the stretched pulse (see figure 2.1). Nowadays usually a combination of gratings is used. Here, the chirp is generated by different wavelength-dependent path lengths. Another combination of gratings is used to recompress the pulse. The duration of the recompressed pulse τ_L is usually $\neq \tau_0$ due to e.g. gain narrowing. This is counteracted, e.g. by an cross polarized wave (XPW) module and acousto-optical modulators. These components are described for the laser used here in publication [14] and briefly in chapter 3.1. Stretching is very effective for short pulses due to their broad bandwidth. The shorter a pulse becomes, the broader the spectral bandwidth has to be. For a Gaussian laser pulse

$$E(t) = E_L cos(\omega_L t + \alpha) \exp\left(-\frac{t^2}{2\sigma^2}\right), \tag{2.1}$$

(example only time dependent) where E_L is the laser amplitude, t is the time, α a phase shift and σ gives the signal width, an example is shown in figure 2.2. The pulse is displayed both in the time domain and in the frequency domain. On the

left the time dependent electric field with a Gaussian envelope is shown and on the right the normalised power of the Fourier transformed signal over the frequency. For a Gaussian pulse the product $\Delta\omega\Delta t \geq 4\ln(2)$ reaches its minimum if the pulse is Fourier-transform-limited.

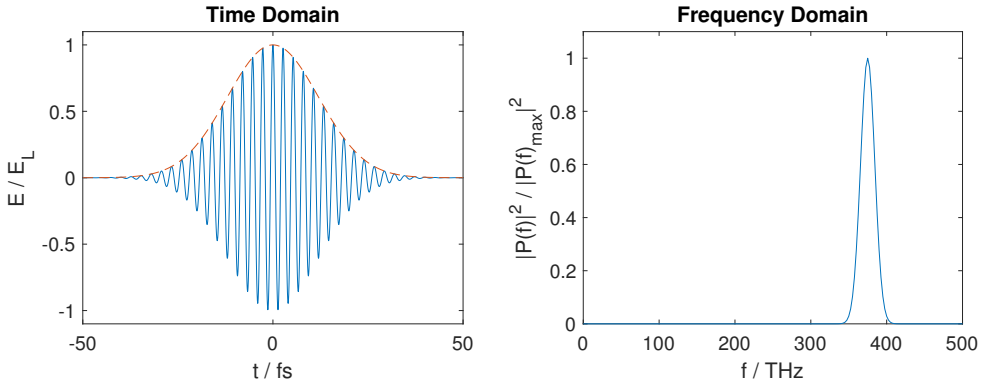

Figure 2.2.: Gaussian laser pulse. *left:* electric field (continuous blue line) with a Gaussian envelope (broken red line) *right:* the normalized power of the Fourier transformed signal over the frequency. The central frequency of the shown pulse is 375 THz (≈800 nm) and the FWHM of the intensity is Δt =20 fs, $\sigma \approx 12$ fs.

In addition to stretching the pulse in time, the intensity is also reduced by expanding the pulse spatially. During the amplification the beam diameter of the chirped pulse is generally enlarged stepwise.

On the target, in turn, the aim is usually to achieve the highest possible intensity. For this purpose, the pulse is focused with a parabolic mirror. The laser intensity at the target is further dependent on the F-number of the parabola used to focus the beam. This number together with the wave length of the focused light λ defines the minimal diameter of the focal spot

$$d \approx \lambda F \qquad \text{with} \qquad F = \frac{f}{D}, \tag{2.2}$$

which depends on the ratio of the focal length f to the beam diameter D.

2.1.2. Electron in Electromagnetic Fields

Since the movement of an electron in an electromagnetic field is the basic principle for the laser-matter interaction, the fundamentals are briefly shown here.

The motion of an electron in an electric field $\mathbf{E}$ and a magnetic field $\mathbf{B}$ can be described by the Lorentz force:

$$\mathbf{F}_L = \frac{d\mathbf{p}}{dt} = -\mathrm{e}(\mathbf{E} + \mathbf{v} \times \mathbf{B}) \tag{2.3}$$

For the non relativistic case, i.e. particle velocities far below the speed of light and a therefore negligible $\mathbf{v} \times \mathbf{B}$ term, $\mathbf{F}_L \approx -\mathrm{e}\mathbf{E}$ and a linearly polarized laser, the quiver velocity of an electron is:

$$v_{qu} = \frac{\mathrm{e}E_L}{m_\mathrm{e}\omega_L} \cos(\omega_L t) \tag{2.4}$$

By normalizing the maximum quiver velocity ($\cos(\omega_L t) = 1$) with c we get the dimensionless laser amplitude :

$$a_0 = \frac{\mathrm{e}E_L}{m_\mathrm{e}\omega_L c} = \sqrt{\frac{I_L}{I_1}}; \qquad I_1 = 1.37 \times 10^{18} \mathrm{W\ cm^{-2}} \left(\frac{\lambda_L}{\mu\mathrm{m}}\right)^{-2} \tag{2.5}$$

This amplitude defines whether the electrons reach relativistic velocities ($a_0 \geq 1$) and a "relativistic plasma" is formed or ($a_0 \ll 1$) and a non-relativistic plasma is formed. [13]. a_0 can be calculated analogous for ions, but due to the mass in the denominator a_0 is much smaller for ions. Therefore, ions do not reach a quiver velocity in the relativistic regime with current laser systems.

2.1.3. Laser Ionisation Processes

The following descriptions are based on chapter 2 of reference [15]. The peak laser intensity of an ultrashort laser pulse can generate electric fields much higher than the electric field from the nucleus at the position of the electron. To estimate the laser intensity threshold of the direct field ionisation, one starts with the Bohr radius a_B of an hydrogen atom

$$a_\mathrm{B} = \frac{4\pi\epsilon_0\hbar^2}{m_\mathrm{e}\mathrm{e}^2} \approx 5.3 \times 10^{-9}\ \mathrm{cm} \tag{2.6}$$

and calculates the electric field at this distance. $\hbar$ is the reduced Planck constant, ϵ_0 is the vacuum permittivity, e is the charge of an electron and m_e its mass.

$$E_\mathrm{B} = \frac{\mathrm{e}}{4\pi\epsilon_0 a_B^2} \approx 5.1 \times 10^9\ \frac{\mathrm{V}}{\mathrm{cm}} \tag{2.7}$$

In the next step the intensity of a laser field that matches the electric field at the Bohr radius of the atom is determined:

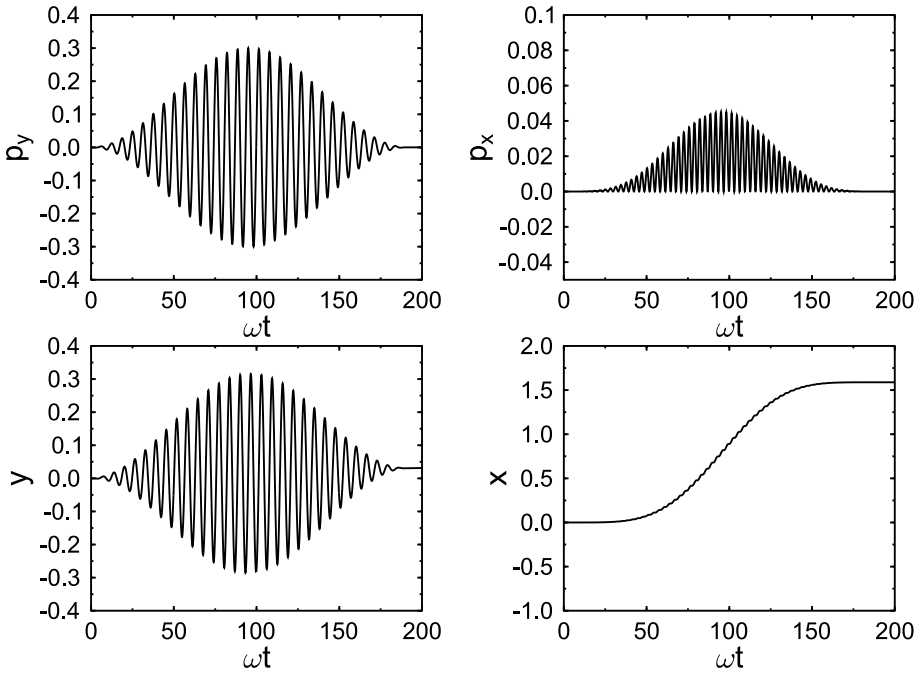

Figure 2.3.: Momentum (top) and trajectory (bottom) of an electron in a short laser pulse. *left:* In direction of the electric field; *right:* In propagation direction of the laser (from [15, p. 37]).

$$I_{\mathrm{B}} = \frac{c\epsilon_0 E_B^2}{2} \approx 3.5 \times 10^{16} \ \frac{\mathrm{W}}{\mathrm{cm}^2} \tag{2.8}$$

This means that as soon as the intensity of the laser $I_L > I_{\mathrm{B}}$, atoms in this field will definitely be ionised (figure 2.4 d). Even though, for high intensity laser pulses, the peak intensity is well above this there are other possible ionisation processes, which take place at far lower laser intensities. These mechanisms are in particular relevant as high intensity laser pulses are accompanied by amplified spontaneous emission (ASE), which can be able to ionize the material sample before the peak of pulse reaches the target.

Multi-photon Ionisation

The possibility of ionising an atom with a single photon is known since the beginning of the 20th century [16]. For this process an atom absorbs a photon that has a higher energy $\hbar\omega \geq I_{\mathrm{P}}$ than the binding energy of the electron. The frequencies of Ti:Sa lasers are generally too low for the photoelectric effect, but since the intensity is very high ($> 10^{10}$ Wcm^{-2}) many photons can interact at the same time with an atom and match the ionisation energy, the so-called multi-photon ionisation (MPI). It is also

possible that even more photons interact at the same time and the electron leaves the atom with a considerable amount of kinetic energy, the so-called above-threshold ionization (ATI). Both processes are shown schematically in figure 2.4 (b).

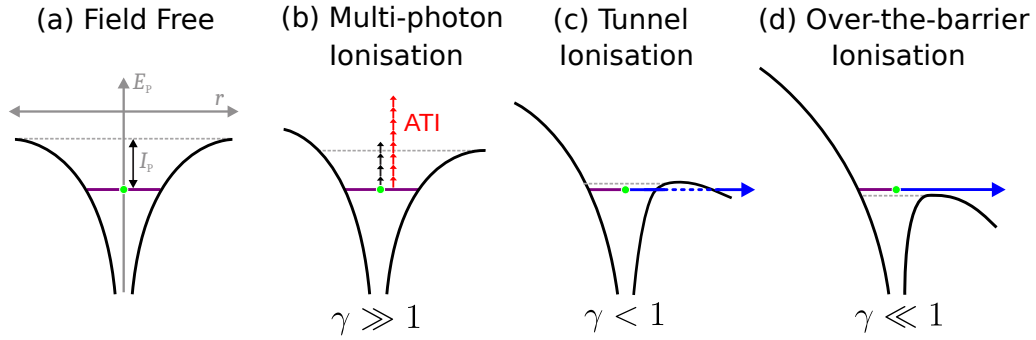

Figure 2.4.: The electric potential of an atom under the influence of increasing laser fields from left to right. I_P is the ionisation potential, and γ is the Keldysh parameter (see equation 2.10). (from [17])

The kinetic energy of the escaping electron can be calculated with an adjusted version of the photoelectric effect-formula:

$$E_\mathrm{kin} = (n+s)\hbar\omega_L - I_\mathrm{P} \tag{2.9}$$

n is the number of photons needed for MPI and s is the number of photons that are absorbed in addition.

Tunneling Ionisation

If the electric field of the nucleus is deformed strongly by the laser, it is possible that an electron tunnels through the remaining potential barrier as shown in figure 2.4 (c). For the estimation, which regime is responsible for the ionisation process the Keldysh parameter γ is used [17]:

$$\gamma = \sqrt{\frac{I_\mathrm{P}}{2U_\mathrm{pond}}}, \tag{2.10}$$

with the ponderomotive energy

$$U_\mathrm{pond} = \frac{I_L \mathrm{e}^2 \lambda_L^2}{8\pi^2 m_\mathrm{e} \epsilon_0 c^3} = 9.337 \times 10^{-20} I_L \lambda_L^2 \, \frac{\mathrm{eV}}{\mathrm{W\ cm^{-2}\ nm^2}}, \tag{2.11}$$

which is the averaged kinetic quiver energy of an electron. λ_L is the wavelength of the laser. If $\gamma \gg 1$ MPI is the main process, for $\gamma < 1$ tunnel ionisation becomes

important until the field is strong enough to deform the Coulomb barrier of the atom below the binding energy, the so-called barrier suppression ionization (BSI) (figure 2.4 (d)) happens for $\gamma \ll 1$. BSI occurs long before the laser field is stronger than the field from the nucleus at the Bohr radius.

The Coulomb potential for an electron of the atom is deformed by adding a stationary homogeneous electric field:

$$V(x) = -\frac{Z\mathrm{e}^2}{4\pi\epsilon_0|x|} - \mathrm{e}\epsilon x, \tag{2.12}$$

with atomic number Z and the constant electric field ϵ in x direction. By calculating the derivative of $V(x)$ and equating it to zero one finds the position of the highest potential on the right-hand side (see figure 2.4 (c) and (d))

$$x_{hp} = \sqrt{\frac{Z\mathrm{e}}{4\pi\epsilon_0\epsilon}}. \tag{2.13}$$

In order to calculate the field strength ϵ_c at which the potential barrier is suppressed below the ionisation potential one inserts x_{hg} in the equation 2.12:

$$V(x_{hg}) = I_\mathrm{P} \qquad \rightarrow \qquad \epsilon_c = \frac{\pi\epsilon_0 I_\mathrm{P}^2}{Z\mathrm{e}^3}. \tag{2.14}$$

Analogous to equation 2.8 we calculate the laser intensity from which the potential barrier is suppressed:

$$I_{BSI} = \frac{I_B}{256} \approx 1.4 \times 10^{14}\ \frac{\mathrm{W}}{\mathrm{cm}^2} \tag{2.15}$$

It is obvious from the last equation that significant ionisation of the target happens well before laser intensities match I_B. I_{BSI} values for other atoms and degrees of ionisation can be found e.g. in reference [15] chapter 2.2.

Even though all the ionisation processes mentioned above take place far below the maximum laser intensity, they cannot be neglected as they influence the physical parameters of the target when the high intensities arrive.

2.1.4. Plasma Parameters

Plasma is a state of matter which contains free electrons, neutrals and partially (or fully) ionised particles. When observed from outside, a plasma is characterised by quasi-neutrality, since the net electrical charge remains the same. Due to the free

charge carriers (electrons and ions) and the relative long range of the electric fields, a plasma is characterised by new properties, which will be briefly discussed below.

The Saha equation describes the relationship between density, temperature and the ionisation state of a gas in local thermal equilibrium. An approximation of the Saha equation [18] can be written as follows:

$$\frac{n_i}{n_n} \approx 2.4 \times 10^{21} \frac{T^{3/2}}{n_i} \exp\left(\frac{-U_i}{k_\mathrm{B} T}\right), \tag{2.16}$$

with the density of ionised n_i and neutral n_n atoms, the ionisation energy U_i, the temperature T and the Boltzmann constant k_B. For room temperature $T \approx 300\,^\circ\mathrm{K}$ and a density of $n_n \approx 3 \times 10^{25}\ \mathrm{m}^{-3}$ the fraction of ionised atoms is $n_i/n_n \approx 10^{-122}$, so almost no atom is ionised. When the temperature reaches the energy level: $k_\mathrm{B}T = 1$ eV the fraction of ionised atoms increases rapidly e.g. from to 0.7 % for a temperature of 1 eV to 11 % for 1.5 eV. There is thus no defined phase transition and it depends to a certain extent on the context when one starts to speaks of a plasma. For the interaction of ultrashort laser pulses with matter the assumption of a local thermodynamic equilibrium is usually not valid. Mainly the electrons are accelerated due to the much bigger charge to mass ratio and the time is to short to transfer much energy from electrons to nuclei by collisions.

Debye length

If an electric charge is inserted into a plasma the electric potential is shielded by the plasma. The characteristic length over which the electric potential decays due to the shielding by e^{-1} (e is Euler's number) is called the Debye length:

$$\lambda_D = \sqrt{\frac{\epsilon_0 k_\mathrm{B} T_\mathrm{e}}{n_\mathrm{e} \mathrm{e}^2}} \tag{2.17}$$

Apart from the constants the Debye length only depends on the electron temperature T_e and the electron density n_e. For the approximation it is considered that the ions are immobile due to their higher mass and short timescales. Therefore only the electrons will be taken into account. This approximation is used throughout the scope of this work, since it is valid for ultrashort laser plasma interactions. The derivation of λ_D can be found in chapter 1 of reference [18].

Plasma Frequency

If an electric charge is removed spontaneously from the plasma an electric field occurs due to the electron density gradient created by this charge. This field accelerates electrons and due to the conservation of momentum these electrons do not stop at the position where the plasma would be neutral but they overshot. Thus, an electric field builds up again and so on. The frequency of this oscillation is:

$$\omega_p = \sqrt{\frac{n_\mathrm{e} \mathrm{e}^2}{\epsilon_0 m_\mathrm{e}}} \tag{2.18}$$

it is characteristic for a plasma and depends in the non relativistic case only on constants (m_e: electron mass) and the electron density. The derivation can be found in chapter 4.3 of reference [18].

Critical Density

The critical density is defined as the density at which the frequency of the incoming electromagnetic wave ω_L is equal to the plasma frequency:

$$n_c = \frac{m_\mathrm{e} \epsilon_0 \omega_L^2}{\mathrm{e}^2} \approx 1.11 \times 10^{21}\ \mathrm{cm}^{-3} \left(\frac{\lambda_L}{\mu\mathrm{m}}\right)^{-2} \tag{2.19}$$

In combination with the dispersion relation $\omega^2 = \omega_p^2 + c^2 k^2$, k is the wavenumber, it can be seen that there are only imaginary solutions for k if $\omega_L < \omega_p$, respectively if $n_\mathrm{e} > n_c$. This means that an electromagnetic wave with $\omega_L < \omega_p$ cannot penetrate through a plasma and will decay exponentially. On the other hand an electromagnetic wave with $\omega_L > \omega_p$ can penetrate through a plasma. This results in the classification of underdense plasma $n_\mathrm{e} < n_c$, which is transparent and overdense plasma $n_\mathrm{e} > n_c$, which is opaque and reflects the electromagnetic waves.

The derivations can be found in chapter 4.12 of reference [18]

2.1.5. Absorption Processes

The following section describes how the laser energy is absorbed, especially by the target electrons. As their charge-to-mass ratio is much higher than for the ions they gain far more kinetic energy. The following derivations are based on the references [15, 18–21], which can be consulted for a more detailed description.

Resonance Absorption

If a p-polarised laser pulse (electric field vector in the plane of incidence) impinges on a preplasma with an incidence angle θ the beam is reflected before it reaches n_c. The preplasma is the plasma created by the laser pedestal and prepulses due to ASEs. It expands in front of the target prior the main laser peak interaction. The density at the turning point is $n_{\text{refl}} = n_c \cos^2\theta$, therefore the beam does not reach the density where ω_L matches ω_p. Nevertheless the evanescent electric field can excite an electron oscillation normal to the target surface at n_c. Under optimal conditions, the absorption of the incident laser beam can reach up to 60 % [15, p. 156]. However, our experimental conditions are far from being optimal for resonance absorption. A femtosecond laser pulse which impinges on an a solid target with a high laser contrast leads to a preplasma with a very steep density gradient $L = (\partial \ln n_e/\partial x)^{-1}$. Further the distance the electrons travel due to the quiver velocity $d = v_{qu}/\omega_L$ is comparably large due to the high laser pulse intensities. If $d > L$ an electron experiences a different ω_p along its path through the density gradient. Therefore the resonance condition is no longer fulfilled.

Vacuum Heating

In the publication "Not-So-Resonant, Resonant Absorption" [22] F. Brunel describes an absorption mechanism for an overdense plasma and a steep density gradient, therefore also the synonyms "Brunel effect" or "Brunel heating" are used instead of "vacuum heating".

For this absorption mechanism laser intensities $I_L\lambda_L^2 \geq 10^{16}$ W μm^2/cm^2 much higher than I_{BSI} (see equation 2.15) are needed as well as a dense target ($n \gg n_c$). If a p-polarised laser pulse impinges on the dense target in vacuum the electrons are dragged out of the target by the field:

$$E_0 = E_L[1 + \sqrt{1-f}]\sin\theta \tag{2.20}$$

For a perfect conductor (the ratio of the absorbed power $f = 0$) the electrons see the field $E_0 = 2E_L \sin\theta$, which is the superposition of the impinging and the reflected wave, θ is the angle of incidence. As the electric field reverses the electrons are pushed into the target again. Because of the high density of the target $n \gg n_c$ the laser cannot propagate in the target and the electrons only experience the evanescent wave when the electric field reverses again, so they keep most of their velocity. Due

to the formation of preplasma there is no perfect steep density gradient. But as an estimation the scale length L on which the density of the target changes in the region around n_c has to be smaller than the trajectory of the electron (cf. figure 2.3 lower left) due to the quiver velocity ($v_{qu}/\omega_L > L$). Otherwise, different absorption mechanisms might be dominant.

A significantly higher absorption of p-polarised compared to s-polarised light (electric field vector orthogonal to the plane of incidence) can be confirmed experimentally, cf. reference [15, p. 170] where Paul Gibbon compared the absorption fraction for several publications.

$\mathbf{j} \times \mathbf{B}$ Heating

In the case of a high density target and a steep density gradient but a normal incidence angle or s-polarised light "vacuum heating" drops out as an absorption process, because the electric field does not have a component normal to the target. In this case "$\mathbf{j} \times \mathbf{B}$ heating" is the dominant absorption process [23]. Due to the magnetic component of the Lorentz force (2.3) the electrons also undergo an oscillation in the direction of the laser. This drift velocity oscillates between zero and a positive value. Therefore, in contrast to the electric field, the position of the electron changes after it is passed by a laser pulse. On the right side of figure 2.3 the momentum and position of an electron are shown without a dense plasma. The oscillation frequency is $2\omega_L$, which can be found by solving the Lorentz equation (2.3) for linear polarised light (see chapter 3 reference [15]). If instead of free space a dense target gets in the way of the electrons, they are pushed in the target. As in the case of "Vacuum Heating", the electrons retain their momentum and travel through the target.

W.L. Kruer and K. Estabrook [23] show that the absorption grows strongly with the laser intensity, but decreases with a higher electron background temperature. In order to keep the absorption as high as possible, the preplasma should be as cold as possible. This requires a very good laser contrast.

2.1.6. Target Normal Sheath Acceleration

There are several different ion acceleration processes, which can be induced by a short high energetic laser pulse (e.g. chapter 5 of the book [19] provides an overview). On basis of the experimental parameters, the target normal sheath acceleration

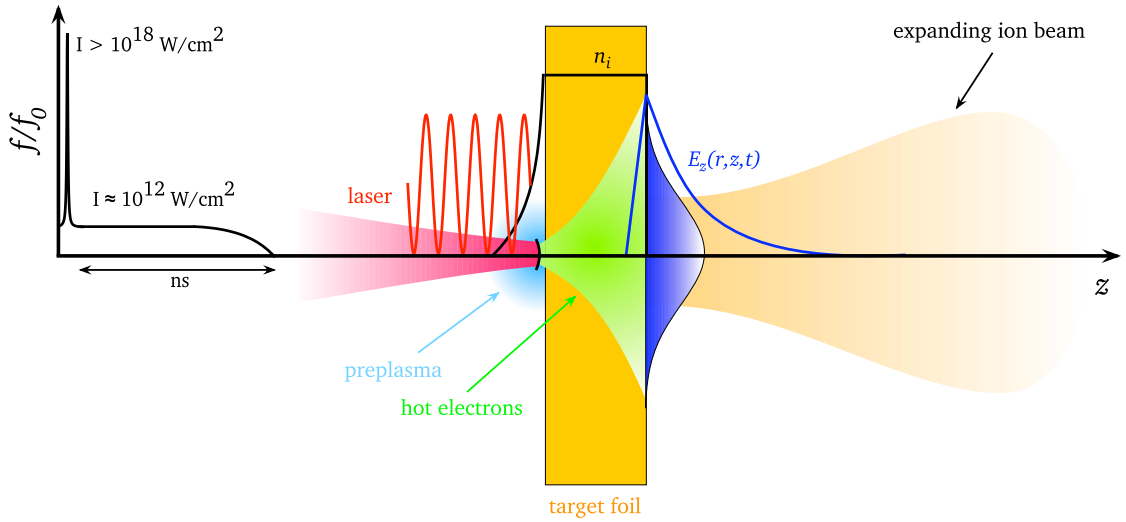

Figure 2.5.: TNSA process: The temporal profile of a laser pulse is shown on the left. The laser pulse (red) impinges on the surface of a target foil (yellow) with a high density $n_i \gg n_c$. Due to the pedestal of the pulse a preplasma (light blue) is formed long before the highest intensities, reach the target. With increasing laser intensity, electrons gain higher kinetic energies. These hot electrons (green) penetrate through the target and leave it at the rear side. This creates an electric field (blue) at the target rear, the so called sheath field, which ionises the surface and ions are accelerated normal to the surface (orange becoming more transparent). (from [26])

(TNSA) mechanism [24, 25] is the most relevant and is therefore explained in more detail below. A schematic representation of the TNSA process is shown in figure 2.5.

When a high power laser pulse impinges on a solid target with a high density $n_i \gg n_c$ a proportion of the laser energy is absorbed by the target electrons, which gain high kinetic energies. These suprathermal electrons are referred to as hot electrons. However, the ions have a much larger mass-to-charge ratio and therefore their quiver velocity can be neglected.

The most important process for generating hot electrons for a p-polarised laser pulse with a high contrast and a target at an incident angle of about 45° is vacuum heating. In the case of a normal incidence on the target it is $\mathbf{j} \times \mathbf{B}$ heating (see chapter 2.1.5). For all cell irradiation experiments shown in this thesis, the first configuration mentioned was utilised. In both cases, the hot electrons propagate through the target and form a highly charged sheath close (on the order of microns)

to the target surface.

$$E \sim \frac{T_\mathrm{e}}{\mathrm{e}L} \tag{2.21}$$

This field E in the order of TV/m [27] is strong enough to ionise the surface atoms and depends on the temperature T_e of the hot electrons and the density scale length L on the target rear [28]. The electric field is perpendicular to the backside and leads to a normal acceleration of the target rear ions as a secondary effect. The stronger this sheath field is, the higher are the energies to which ions can be accelerated. Thus, for the TNSA process, high laser absorption must be ensured on the front side of the target to generate high electron temperatures and, at the same time, the back side of the target must remain intact to maintain a steep density gradient. The accelerated ions originate from an impurity layer on the target surface [29], since only these ions are exposed to the strong electric field and shield the ions behind them. The ions are accelerated from the surface in a cone. The angular width narrows for higher ion energies in a range of 10° to 40° [30]. The duration of ion acceleration is estimated to be about $t_{acc} \approx 1.3\tau_L$ (see publication [13]). The resultant ion spectrum has generally an exponential decay. The target has to be thick enough (usually thicker than a few µm) thus the integrity of the rear side is still given when the sheath field is formed.

2.1.7. Bragg Peak

William H. Bragg and Richard Kleeman investigated the ionising effects of α particles from a radium source with an ionisation chamber. They discovered that the ionisation potential rises near the end of the particle tracks [31]. The tip of the ionisation potential of ions is thus called the Bragg peak. This peak that occurs for all ion types is also the reason why fast ions are of great interest for radiotherapy [1, 6, 7]. By adjusting the kinetic energy of the particle, the position of the Bragg peak can be adjusted very precisely. Thus, a tumour to be irradiated is usually scanned by varying the particle energy. Unlike photons, ions allow the highest dose to be delivered to the tumour and not to healthy tissue, without having to change the beam path. With particle therapy, the total dose in healthy tissue can thus be significantly reduced.

The mean energy loss of a fast ion per distance travelled through a material was theoretically investigated by Hans Bethe [32]. The equation that describes the

dispensed energy of fast ions is therefore called the Bethe formula (sometimes also called Bethe-Bloch formula). In non relativistic form:

$$\frac{dE}{dx} = \frac{4\pi n_e Z^2}{m_e v^2} \left(\frac{e^2}{4\pi\epsilon_0} \right)^2 \ln\left(\frac{2m_e v^2}{I} \right), \tag{2.22}$$

where Z is the charge in multiples of the elementary charge e (in the case of protons: $Z = 1$) and v is the particle velocity. I is the mean excitation potential, which is typically a few tens of eV. Reference [33] is recommended for derivation, medical relation and values for the mean excitation potentials (additional values can be found here [1,2]). In the experiments presented in this thesis, the LAPs are interacting with different materials and have a broad energy range. Therefore, the dosimetry was carried out with a Monte Carlo code. This is necessary to estimate both the number of particles and the particle energy to expose the cells to a defined dose. The programme is described in Chapter 3.2.6.

However, not only the total dose has an influence on the radiation effect, but also the energy deposited by the ionising ion along its path, the linear energy transfer

$$LET_\Delta(x) = \frac{dE_\Delta}{dx}. \tag{2.23}$$

The Δ indicates that energy losses above a certain threshold are neglected. This means that secondary particles, very fast electrons, that could leave the particle track too far can be discarded. These electrons are therefore called delta rays. Since we operate with comparatively small particle energies no threshold is needed and the nuclear effects can be neglected. Thus, the LET is equal to the stopping power. Most studies [34, 35] show an increase in the relative biological effectiveness (RBE) with LET. This means that at a higher linear energy transfer (LET), the survival rate of cells decreases compared to the same dose at a lower LET. For very high dose rates, this effect decreases again, but this is not relevant due to the comparatively low LET of protons.

2.2. Medical-biological Background

Due to the cooperation of two different disciplines, biological basics are also briefly presented. Not only effects of ultra-short pulsed proton bunches on normal hematopoi-

[1] https://physics.nist.gov/PhysRefData/XrayMassCoef/tab1.html
[2] https://physics.nist.gov/PhysRefData/XrayMassCoef/tab2.html

etic CD34+ progenitor and stem cells were studied, but to improve reproducibility and availability also other primary cells and cell lines were used. Therefore, in the following, the basics of the human cell will be described and, more specifically, the blood cells. Subsequently, the effects of radiation on the cells will be discussed, as well as the associated detection methods. The background of this section is based on the book [36].

2.2.1. The Human Cell

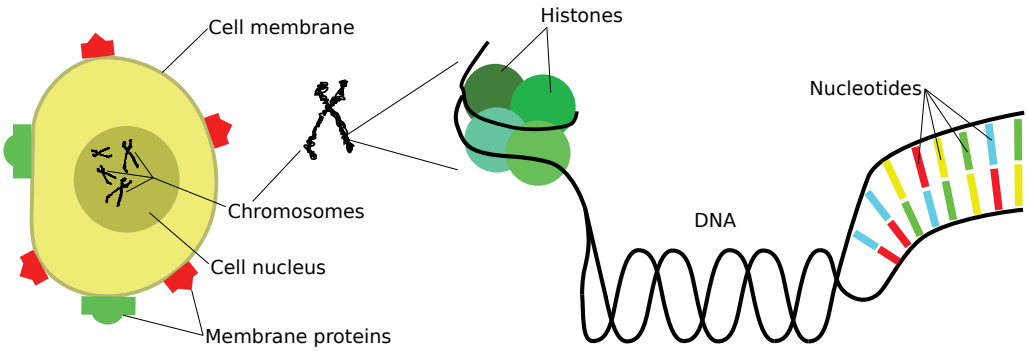

Figure 2.6.: Schematic representation of a human cell. *left:* The cell is separated by the cell membrane, on which various proteins are located. The cell nucleus is the only organelle depicted. It contains the chromosomes, which in turn contain or organise the DNA mainly through histones. *right:* Zooming in further reveals the double helix structure of DNA, which in itself is made up of four different nucleotides.

The cell forms the basic structural and physiological unit of the human being, as well as of all other organisms. It forms a closed unit via its membrane and serves as a building block for organs and the entire organism. Since the biological experiments shown examine the effect of ionising radiation at a cellular level, the basics of a human cell are presented here.

A highly simplified illustration of the human cell can be found in figure 2.6. The inner cell environment, also called cytoplasm, is separated from the outer environment by a cell membrane (also known as plasma membrane). The membrane mainly consists of a phospholipid bilayer structure that contains membrane proteins, which perform a wide range of functions including particle transport, adhesion and signal transduction. There are membrane proteins that are specific to cell types, therefore these proteins are marked by specific antibodies and used to determine different cell types.

In the cytoplasm there are the organelles, one of them being the Nucleus. It is enclosed by its own membrane and contains the chromosomes. Since the Deoxyribonucleic acid (DNA) is a long molecule (almost 2 m divided over 46 chromosomes), it is organised in the chromosomes by packing proteins, which are called histones. One of these histones is H2A.X, which plays a significant role in the detection of radiation damage. Furthermore, the DNA is rolled up in the shape of a double helix, which exists due to hydrogen bonds between the nucleotides. The DNA is composed of four different nucleotides, which always occur in pairs. Adenine binds to thymine and guanine to cytosine. The purpose of the DNA is to store the biological information. Before cell division, the DNA is replicated so that both cells have the complete genetic information after division. The other form of passing on information from the DNA runs via RNA. An example is the production of a specific protein. For this, the DNA is first transcribed to RNA and from there to a protein. RNA also consists of four different nucleotides, but here thymine is replaced by uracil and it is made up of only one strand. All RNA transcripts that are present in a cell at the same time are called the transcriptome. It shows which genes are currently active. Unlike the genome, which is the same in every cell, the transcriptome differs greatly among different cell types and cell states. The changes due to irradiation are of particular interest here.

2.2.2. Hematopoietic Cells

The cells of the blood can be divided into three subgroups [36, p. 1395]. Red blood cells, also known as erythrocytes, are responsible for the transport of oxygen and CO_2 and are the most abundant cells in the blood with 4 to 6 million per mm^3. Platelets, also called thrombocytes, are responsible for blood clotting. In one mm^3 blood 250 to 400 thousand thrombocytes can be found. These two groups are extremely specialized and have no longer a nucleus or cell organelles, therefore they were not used for the investigations in this work. The third group is formed by white blood cells, also called leukocytes, which are much rarer at 5 to 10 thousand per mm^3, but have both organelles and nuclei and are therefore, along with stem cells, the primary cells used for experiments in this work. The group of leukocytes is in turn divided into further subgroups, which perform specific functions in the defence against pathogens. These can be distinguished morphologically or by cell surface markers. All the previously mentioned cells have the same progenitor cell, which are the normal hematopoietic CD34+ progenitor and stem cells (CD34+ cells).

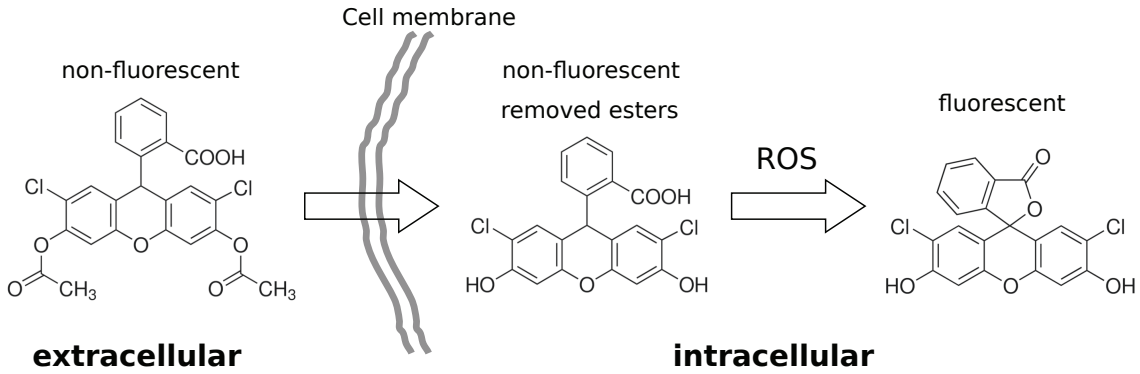

Figure 2.7.: The molecule DCFH-DA passes the cell membrane, its esters are removed and its trapped intracellular. On contact with ROS, the molecule becomes strongly fluorescent. (The illustration is based on [37, 38].)

2.2.3. Radiobiology

Ionising radiation has many effects on living cells. In the following, the two most characteristic effects are examined in more detail: firstly, the production of free radicals and secondly, the damage to the genetic material.

Oxidative Stress

The absorption of ionising radiation in the cell causes dissociation of molecules, called radiolysis. The particles created in this process are usually highly reactive and are termed radicals. Since water is the most common molecule in a cell, the radiolysis of water is of particular interest. The resulting ROS cause the radiation damage in a secondary effect, e.g. by interacting with proteins or DNA.

To quantify the ROS produced by ionising radiation, there are several molecules that change their fluorescence properties when exposed to ROS. In the following, the verification with 2‘,7‘-dichlorodihydrofluorescein diacetate (DCFH-DA) is discussed in more detail [37, 38]. Extracellular dissolved DCFH-DA can cross the cell membrane. Intracellular, the esters are removed by esterases and as a result the molecule is trapped in the cell. If this molecule is now oxidised by ROS to 2‘,7‘-dichlorofluorescein (DCF) it shows bright green fluorescence (figure 2.7 shows this process schematically). A linear relationship between the concentration of hydrogen peroxide (10 µM to 100 µM) and the fluorescence intensity is observed [38]. The dose range studied in this work will lead to concentrations due to radiolysis below these values, but there is no reason to assume a significantly different trend.

DNA Damage

The genetic material can be damaged by ionising radiation indirectly, for example, by the interaction with ROS or directly, for example, by the hit of a fast proton. Both processes can lead to a wide variety of damages, such as point mutations, unreadability of nucleotides by DNA polymerases, or DNA strand breaks. These breaks are divided into two categories: if only one stand breaks it is a DNA single strand break (SSB) and if also the complementary DNA strand breaks it is a DNA double strand break (DSB). In the literature, a range of 10 to 25 base pairs can be found, as the maximum distance between two SSBs for a DSB [39–41]. DSBs are among the most lethal cell lesions caused by ionising radiation. The probability of the occurrence of a DSBs depends on the LET and increases for ions with higher values (an estimate of the increase in DSB can be found in reference [40]). Experimentally, the proof of DSBs is usually conducted via γH2A.X [41]. As mentioned earlier, H2A.X is a histone and in the event of a DSB it is phosphorylated to γH2A.X. The formation of γH2A.X foci takes place within the first minutes after irradiation and reaches its maximum after about 30 minutes with a subsequent plateau phase of about one hour. This is followed by a slow decay over several hours [41].

The process described above is only a small part of the DNA damage response to DSBs. As a consequence, the cell can induce cell death via apoptosis, induce cell cycle arrest or repair the DSB. The repair can be carried via different pathways, the dominating once are the more common non-homologous end-joining and homologous recombination. Further information on this can be found in the review articles [42, 43].

2.2.4. FLASH Effect

The phenomenon that tumour control remains the same while healthy tissue is spared during irradiation with high dose rates is called the FLASH effect [3, 44, 45]. FLASH-radiotherapy (RT) aims to benefit from this effect for tumour irradiation, either by reducing the side effects for patients or by allowing higher doses to be applied. Currently, FLASH-RT is a very active field of research, as recently the first patient has been successfully treated [46] and further clinical trials are being carried out[3]. In the first published clinical study, one of the patient's tumours was

[3]ClinicalTrials.gov Identifier: NCT04592887

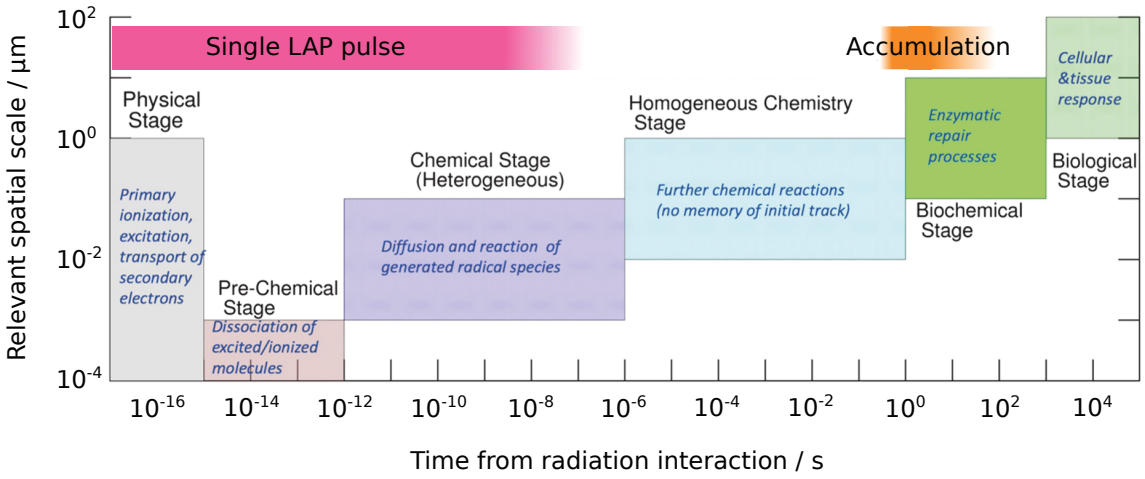

Figure 2.8.: Temporal and spatial scales for the various radiation interaction processes (physical, chemical, biological) compared to the pulse duration of a single LAP pulse (pink), and to the accumulation of multiple shots (orange). The pulse duration depends, among other things, on the energy resolution and the distance between the laser/target interaction and the cell sample. For multiple shots, the time scale depends on the shot frequency and the number of shots. (Basic structure from [48])

irradiated in 90 ms with an electron beam dose of 15 Gy. In addition to complete tumour control (follow-up 5 months), there were also significantly fewer side effects in the healthy tissue. On the other hand, the causes of the FLASH effect are still largely not understood, even though the first experimental evidence of a dose rate-dependent radiation effect on human cells with electron pulses is already over 50 years old [47]. The FLASH effect has now been demonstrated for different types of radiation: electron, X-ray and proton radiation. Recently, the FLASH effect is also being investigated for heavier ions [48]. This work focuses on the irradiation with protons, but the other types of radiation mentioned could also be produced at high dose rates with ultrashort pulse lasers.

FLASH irradiation starts from dose rates of 30 to 40 Gy/s. This corresponds to more than 100 times the conventionally used dose rates, which are in the range of a few Gy per min [3]. Besides the lower toxicity to healthy tissue, also other effects are associated with FLASH, for example the “sparing of memory in mice after whole brain irradiation with dose rates above 100 Gy/s” [2].

One possible and most frequently discussed cause of the FLASH effect is the oxygen consumption, but other causes, such as a different and lower level of chromosomal damage, different form of cell cycle arrest or varying activation of certain

proteins are also discussed [49–51]. Even if not all FLASH effects that show up *in vivo* are also detectable *in vitro*, the effects must relate to the different radiation interaction times and thus to the temporal and spatial scales of the processes taking place. Figure 2.8 compares the time scale with the spatial scale on which the radiation effects occur. The FLASH effect begins at irradiation time scales shorter than a few hundred milliseconds. Usually, single or several microsecond long pulses are used for irradiation, which come at a high frequency ($\geq$ 100 Hz). LAP irradiation involves shorter pulses in the nanosecond range, but the repetition rate is limited to 5 Hz (for the Arcturus laser system). The conventional irradiation is rather in the minute range and thus the reason for the FLASH effect should be temporally in the windows of "Further chemical reactions" and "Enzymatic repair processes" (cf. figure 2.8). Also, due to spatial scales, both effects could take place, since at the high dose rates in combination with a sufficient dose it is likely that two independent events have a sufficient spatial proximity.

Since oxygen consumption, which is one of the probable causes of the FLASH effect, is related to ROS (see chapter 2.2.3), which is an essential part of the work (see chapter 5.5), it will be discussed in more detail below. Tumour tissue is often affected by hypoxia. In healthy tissue, the cell supply with oxygen and nutrients, as well as the removal of metabolic waste products, is ensured by a functioning blood vessel system. Due to the rapid cell growth in a tumour, the oxygen supply cannot be sufficiently ensured because the blood vessels do not grow at a sufficient speed or are dysfunctionally created. Many tumour cells are therefore only supplied with oxygen via diffusion, which is greatly reduced after a few cell layers. What sounds like an advantage at first, however, has the distinct disadvantage that radiotherapy shows significantly reduced effectiveness to hypoxic cells. In order to achieve the same proportion of surviving cells after irradiation, the dose for cells lacking oxygen must be higher by a factor of 2.5 to 3 [52]. FLASH-RT causes a rapid loss of oxygen molecules in the cell. Due to the short duration of the irradiation, this loss cannot be compensated for during the irradiation. In the case of conventional RT, on the other hand, this loss can be replaced during the irradiation, so that the FLASH effect is likely based on a temporary hypoxia [49]. As a result of the oxygen depletion, fewer ROS are generated and thus do not contribute to cell damage. For low LET radiation, most of the DNA damage is caused by ROS (60 - 70 %), so that a reduction in the level of ROS would have a significant impact [51]. Unlike *in vivo*, many studies *in vitro* do not observe cell sparing due to the FLASH effect

[53]. The probable explanation for this is the oxygen concentration in the cell. In *in vitro* experiments, the oxygen concentration is usually at the atmospheric level ($\approx$ 20 %), but in organisms it is significantly lower ($3 - 7$ %) [51]. This explains why *in vivo* oxygen depletion can occur sooner than *in vitro*. The relationship between the relative partial pressure of oxygen was recently investigated in a study that found the greatest differences in survival rates (up to 2.5) between FLASH and conventional irradiation at a value in the range of 3 - 4 % [54].

3. Laser System, Diagnostics and Radiation Chamber

High power lasers are used for various applications e.g. particle acceleration or X-ray generation. For most of the experiments presented in this thesis laser accelerated ions were investigated. These particles were further used to irradiate biological cells. In the following brief overviews of the laser facility and of the main diagnostics are given.

3.1. Düsseldorf Arcturus Laser Facility

The dual beam Ti:Sa laser system Arcturus [14] using the CPA technique [12] is located at the Heinrich-Heine-University Düsseldorf. The laser system has two CPA stages, which can be seen in figure 3.1.

The seed pulses with a bandwidth of about 100 nm ($<$ 20 fs) and a repetition rate of 76 MHz originate from a commercial Ti:Sa oscillator. In the first stage, background highlighted in grey, the pulse is stretched and its energy is increased from 5 nJ to 3 mJ before compression. Further, the repetition rate is reduced to 10 Hz.

The amplified pulse is compressed and sent to the "XPW module"[55]. The bandwidth of the input pulse is reduced to about 35 nm ($\approx$ 40 fs) due to gain narrowing during the amplification. XPW generation is a third order process. This means that the input intensity is proportional to the cubed output intensity [56]. As the name already indicates, the generated wave is polarised perpendicular to the input wave and these two waves can be separated with polarisers. This improves the Arcturus laser contrast by up to three orders of magnitude, but reduces the pulse energy by about 90 percent. Further, the spectrum of the laser pulse is broadened (factor 1.7 $\rightarrow$ 60 nm), which leads to a shorter Fourier limited output pulse. The shortening of the pulse is related to the chirp of the input pulse, which should

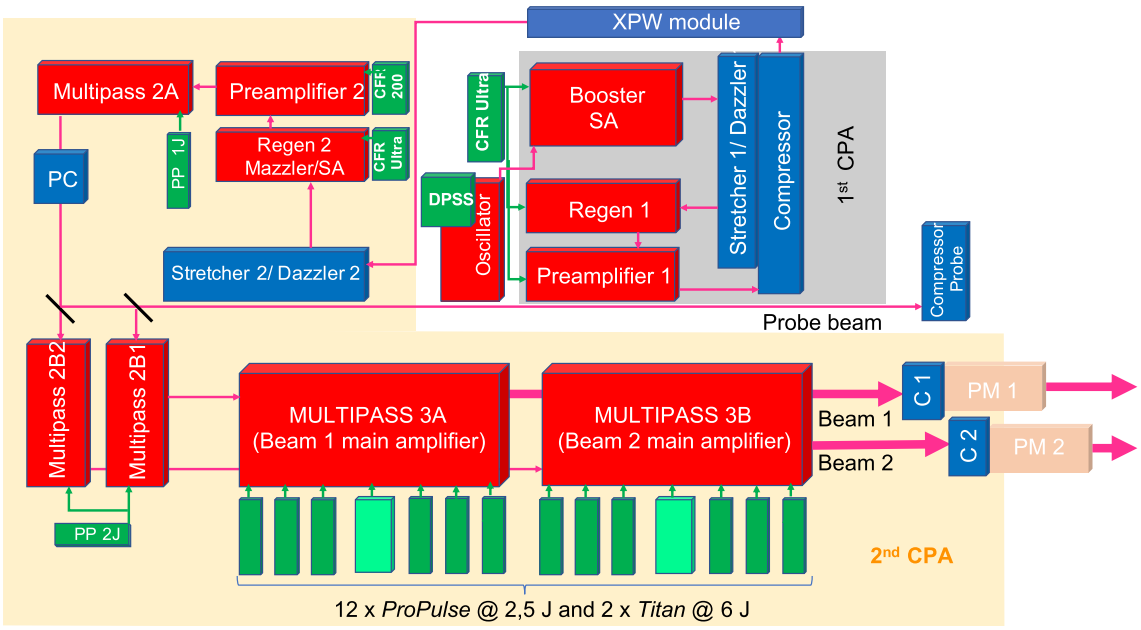

Figure 3.1.: A schematic drawing of the Arcturus laser system. The additional pump lasers (*Titian*) in the two beam lines after the upgrade are drawn in light green. (from [14])

be as small as possible for an ideal result. The broadening of the spectrum is a consequence of the so-called four wave mixing process, the interaction of three waves in the non-linear BaF_2 crystal produces a fourth: $\omega_4 = \omega_1 + \omega_2 - \omega_3$ (due to phase mismatching, the sum of all three frequencies can be neglected). Since a short pulse is never monochromatic, the generated pulse has an even broader spectrum due to the mixing process of the frequencies. In publication [57], the possible shortening of $\sqrt{3}$ is estimated by taking the convolution of the frequency-dependent electric fields with a Gaussian shape for the mixing process. By Fourier transformation, one gets the time-dependent electric field and the convolution becomes a multiplication operation. By transforming, the factor 3 comes into the exponent of the electric field, from which one obtains the intensity falling faster by the factor $\sqrt{3}$.

In the second stage, background highlighted in yellow, the pulse is stretched again and amplified. Before the pulse is fed into the regenerative amplifier, it passes through a "Dazzler" (one is also implemented in the first CPA stage) and, in the regenerative amplifier, repeatedly through the "Mazzler" [58] (both devices from *Fastlite*). They are acousto-optic modulators that modulate the phase and frequency-dependent gain, respectively. In other words, higher order dispersion as well as gain narrowing can be compensated. The acousto-optic modulators are ad-

justed via a feedback loop with the pulse compression diagnostics. Since this process is relatively stable, it does not have to be repeated every time the laser is operated.

The pulse repetition rate is further reduced to 5 Hz. Since the laser pulse is split in front of the last two amplification stages, which are in duplicate, it is possible to perform two beam experiments with nearly identical beam parameters. In both high power laser beams pulses with up to 7 J in energy before compression are generated. Each beam line has its own compressor in which gratings compensate for the linear chirp, shortening the output pulse to about 30 fs FWHM. In the course of the time in which this work was carried out, a laser upgrade was performed. The relevant change for this work is the installation of a stronger additional pump laser in each of the two beam lines (see figure 3.1), so that the pulse energies before the upgrade were only about half as high.

The contrast of the laser pulses can be enhanced optionally by a plasma mirror (PM), which is behind each compressor. Here, it is taken advantage of the fact that a high power laser pulse can induce a plasma on an antireflection coated glass. As long as the laser intensity is below a threshold nearly no light is reflected (0.1 % - 0.2 %), but above the threshold a plasma is formed on the surface and the reflection rises up to 80 % [59, 60]. Theoretically, the contrast could be improved by almost three orders of magnitude. But since a PM has to be moved to a new position after each shot, a PM is only used for low repetition rates. The energy on target is between 30 % and 50 % depending on the optical components used such as PM, parabolae and gratings. The 10 cm in diameter beams are guided to the chamber in vacuum to prevent dispersion and focussed by f/2 parabolae onto solid, gaseous or cluster targets. Thus, the laser beams reach an intensity of 10^{20} Wcm^{-2} within a focal spot diameter of about 5 µm. With a high contrast laser pulse (10^{-11} in 100s of ps time scale) protons with energies of several MeVs can be accelerated.

The delay between the two pulses can be controlled by varying the distance they travel between zero and 6 ns, but the distance can be increased without major effort to reach delays up to 40 ns. Further, the intensity of the beams can be adjusted independently by varying the pumping power or by using attenuators (more detailed data on the laser system, including laser contrast, focus size and pointing stability, can be found in reference [14]).

3.2. Diagnostics for Laser and Plasma Physics

The following is a description of the pool of devices, methods and techniques used in this work, most of which are standard in laser plasma diagnostics.

3.2.1. Thomson Parabola Spectrometer

To analyse the accelerated ions it is common to use a Thomson parabola spectrometer (TPS) [61]. This device discriminates ion species due to their different charge-to-mass ratio (see traces in figure 3.2 right) and also gives an energy spectrum of the individual species.

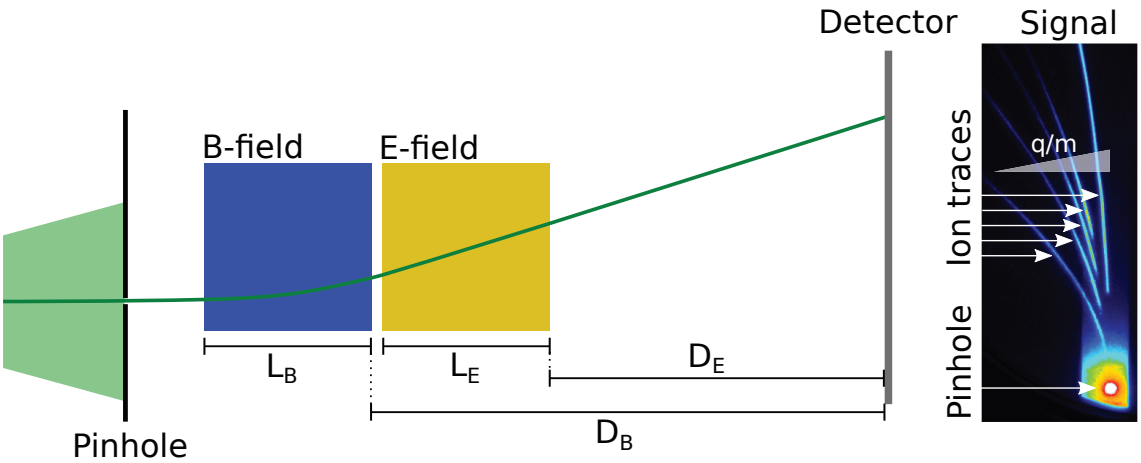

Figure 3.2.: Setup of a Thomson parabola spectrometer. A pencil beam (green) is created from the divergent ion flow (transparent green) using a pinhole aperture. The pencil beam is first deflected by a magnetic field and then by an electric field (for better representation, the green line corresponds to an ion species and an energy). Depending on energy and charge-to-mass ratio, the ions hit the detector in a certain position. A recorded TNSA spectrum can be seen on the *right*. The ions were deflected upwards by the magnetic field and to the left by the E-field. Each track corresponds to a constant charge-to-mass ratio, this ratio increases from left to right tracks.

The construction of a TPS can be seen in figure 3.2 and its generated spectrum on the right. A pinhole is used to generate a pencil beam from an ion beam with a large opening angle. These ions are first deflected by a magnetic field and then by an electric field orthogonal before they impinge on the detector. Since both the dimensions and the field strengths are known, the Lorentz equation 2.3 can be used to determine their impact location. Two assumptions are made for the following formulae. Firstly, the magnetic field is significantly smaller than the Larmor radius

of the ion and secondly, the ion energies do not lie in the relativistic range. Both requirements are fulfilled for the shown experiments.

The deflection due to the electric field is

$$x = \frac{qE_0L_E}{mv^2}\left(\frac{L_E}{2} + D_E\right) = \frac{qE_0L_E}{2E_{kin}}\left(\frac{L_E}{2} + D_E\right), \tag{3.1}$$

and due to the magnetic field

$$y = \frac{qB_0L_B}{mv}\left(\frac{L_B}{2} + D_B\right) = \frac{qB_0L_B}{\sqrt{2mE_{kin}}}\left(\frac{L_B}{2} + D_B\right), \tag{3.2}$$

where L_E and L_B are the lengths of the electric and the magnetic fields and E_0 and B_0 are their corresponding field strengths. D_E and D_B are the distances from the detector to the rear of the electric field and the magnetic field, respectively. q is the net charge of the ion and m its mass. The ion defection is inversely proportional due to the electric field to v^2 or rather to E_{kin} and due to the magnetic field to v or to $\sqrt{E_{kin}}$. This means that the traces converge towards the zero point, i.e. the impact point of an undeflected particle, the higher the particle energy becomes. Since protons have the highest charge-to-mass ratio of the ions, its track is on the right-hand side.

For the analysis of the data, it is important to determine the position of deflected ions relative to the zero point as accurately as possible. Since the magnetic field cannot simply be switched off, the fact that X-rays are also produced during the laser-target interaction is exploited here. Since photons are not deflected by the fields, they image the pinhole on the detector at the zero point. The impression that the pinhole appears to have a much larger diameter than the ion tracks is due to the fact that the signal here is intentionally oversaturated in order to represent the ion tracks as well as possible.

The lengths of the electric field L_E and the magnetic field L_B were 5 cm each. The electric field strength was around a few kV and the magnetic field strength was up to 0.5 Tesla. The sequence, first the magnetic field and then the electric field, was chosen to prevent the ions from hitting the plates.

3.2.2. Microchannel Plate Detector

A micro-channel plate (MCP) is often used as a detector for a Thomson parabola, as it has two major advantages: the outcome is quickly displayed and the vacuum

does not have to be broken. Therefore, the functional principle is briefly explained below.

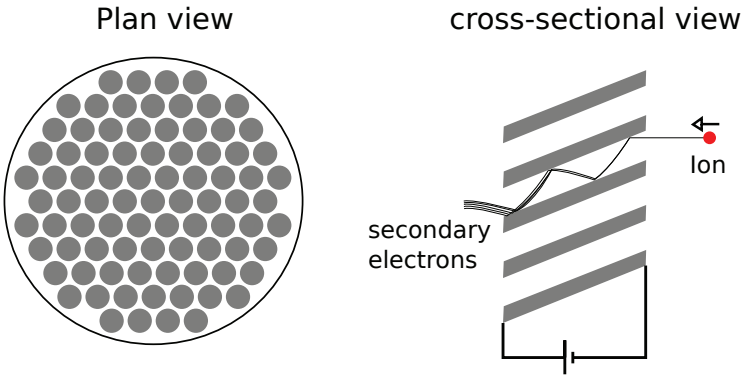

Figure 3.3.: Schematic drawing of an MCP. *left:* plan view of the MCP. A round disc with perforations (microchannels) that are displayed in grey. *right:* cross-sectional view of the microchannels. A fast ion impinges on the wall of a microchannel and generates secondary electrons. These electrons are accelerated by a high voltage along the microchannel and generate further secondary electrons, so that an electron multiplication occurs at the end of the tube.

The MCP consists of a disc with a regular array of small holes. These holes do not go straight through the plate, but are tilted by a small angle to increase the electron yield (see figure 3.3). The diameter of the holes or microchannels is typically a few µm and the thickness of the disc is typically in the mm range. The smaller the channel spacing, the higher is the possible resolution. One of the MCPs used, the *F1942-04 HAMAMATSU*, has a channel diameter of 25 µm with a bias angle of 8°, a thickness of 1 mm and a channel pitch of 31 µm. A high voltage is applied to the channels. When a fast ion hits a channel, it triggers secondary electrons at this point. These electrons are accelerated in turn by the applied voltage and release further electrons when they hit the channel wall. This process is repeated until the end of the channel and the number of electrons is highly increased (schematically shown in figure 3.3 on the right). For the mentioned MCP, this multiplication is estimated with at least 10^4. These output electrons impinge on a readout device.

Two different systems were used here. On the one hand a phosphor screen and on the other an anode. With the phosphor screen, the spatial distribution of the impacting ions can be traced, but there is no temporal resolution. If the output electrons impinge on a single anode, we get a temporal resolution (*HAMAMATSU F9892-31/-32:* 700 ps), but the spacial resolution is lost. Therefore, this is called time of flight (TOF)-MCP.

3.2.3. CR39

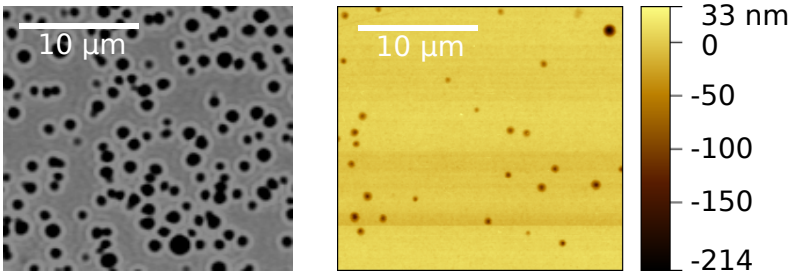

Figure 3.4.: Images of CR39 plates with different track densities *left:* section of a bright field image and *right:* section of the same size of an AFM image with scale for the etching depth.

CR39 is a plastic polymer and can be used as a solid state nuclear track detector [62, 63]. The functional principle is to make the path of a charged particle visible. On its path trough the CR39 plate the fast particle loses most of its energy by ionisation and leaves a track of damages on the particles way [64]. When these plates are etched, the etch rate of the bulk material differs from that of the track, which is significantly higher. This makes the particle tracks visible in the form of small holes, which can be seen under a bright-field microscope or, less commonly, detectable with atomic force microscopy (AFM). Example images are shown in figure 3.4: on the left bright-field microscopy and on the right AFM. Since the etch rate is LET dependent, therefore the detectability also depends on the initial particle energy. This is also the reason why the detector is extremely insensitive to other types of radiation (low LET radiation) such as electrons and X-rays. In publication [65] track diameters are systematically measured as a function of the proton energy and the etching time and it can be seen that the maximum diameter shifts to higher energies for increasing etching times. At low energies, the detectability is limited due to the insufficient penetration depth of the protons, but since it is below 100 keV [66], the range is more than sufficient for cell experiments. On the high energy side, i.e. for a decreasing LET, the detection limit is much higher ($\gg$ 5MeV) than the maximal LAP energy utilised in this work. Furthermore, it is dependent on the angle of impact. Since the LAPs have a very steep angle of incidence, the detection limit should have little influence on the measurement.

Here the CR39 plates were etched in a sodium hydroxide solution with a molar concentration of 6 mol/l and at a temperature of 78 °C. The duration of the etching process ranged from 30 minutes to several hours, depending on the track density

and the initial particle (proton) energy.

3.2.4. Image Plates

The underlying principle on which image plates (IPs) are based is photostimulated luminescence (PSL) [67–72]. A schematic representation of the process can be seen in figure 3.5. The IPs (*BAS-TR2040 Fuji*) are irradiated with ionising radiation. Electrons of the active layer, which is composed of BaFBrI:Eu^{2+} phosphor and urethane resin, absorb energy and are trapped in lattice defects, so called F-centers. These states are metastable and the electrons can be liberated form here to the conduction band with red light. By decaying to the ground state form the conduction band higher-energy photons (ultraviolet) are emitted. Due to the different energies of the photons, the PSL can be well separated from the excitation light with a filter. These blue photons are collected and from this the image is created.

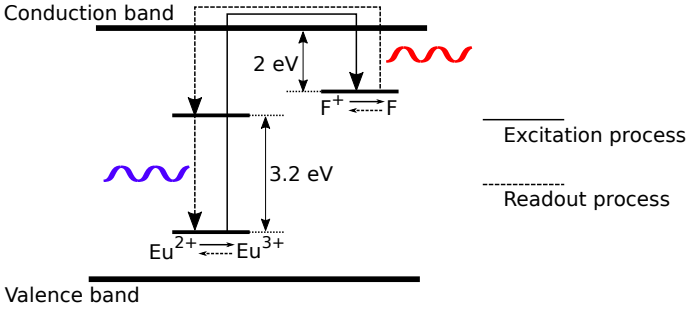

Figure 3.5.: Representation of the energy levels involved. An electron is lifted to the conduction band by ionising radiation and can be trapped by an F-center. In the readout process this electron is liberated to the conduction band by absorbing red light and returns to the Eu atom by emitting a blue photon.

The IPs used here consist of 3 different layers [73], an active phosphor layer, a support layer and a magnetic layer. There is no additional protective coating on the active layer to be able to detect even small ion energies. However, the IPs are usually wrapped in aluminium foil to protect the active area from light, which would lead to a strong signal decay.

As the active layer is 50 µm thick and the intensity of the PSL is dependent on the absorbed energy, the luminescence in turn depends on the ion energy. A calibration curve for protons can be found in reference [70]. The maximum is reached for protons with an energy of about 1.5 MeV. Furthermore, 2 calibration curves are provided. For proton energies (E_{proton}) smaller than 2.11 MeV:

$$FIT_1(E_{proton}) = 0.22039 \exp\left\{-\left(\frac{E_{proton} - 1.5049}{1.1842}\right)^2\right\} \tag{3.3}$$

And for proton energies in the range from 2.11 MeV to 20 MeV:

$$FIT_2(E_{proton}) = 0.33357 E_{proton}^{-0.91377}. \tag{3.4}$$

Since there is a linear relationship between the PSL and the grey values of the image obtained [73], these calibration curves can be used directly on the image data.

3.2.5. Radiochromic Films

The use of radiochromic films (RCFs) is widespread in medicine [74] and laser plasma physics [75]. They are one of the standard diagnostics, as they are usually easy to implement in the experimental setup, self-developing and give a direct feedback on the dose without post-procession, which makes them convenient to use. There are many publications related to the dose calibration [76–78].

In this work the *GAFChromic HD-V2* film was used. The film consists of two layers, a 97 µm thick polyester substrate on which an active layer with a thickness of 12 µm is attached. When the active layer is exposed to radiation a blue polymer is formed and can be easily detected with the eye. The absorption maximum is at about 670 nm. For a more dedicated analysation the films are scanned with a flatbed scanner.

For deployment, the films were usually placed in a stack wrapped in aluminium foil a few centimeters behind the interaction point in proton acceleration direction. In this way, the signal intensity in the different stack positions can already be used to make statements about the proton energy spectrum and thus whether the TNSA process was successful or the interaction parameters need to be changed. Since the dynamic range of the film turned out to be too high (indicated range: 10-1000 Gy) to determine the dose used in cell experiments precisely and other films for smaller doses had the disadvantage of a relatively thick surface layer before the active layer, a dosimetry based on RCFs was not considered.

3.2.6. SRIM

In this work the ionising effects were calculated with the Monte Carlo program “the stopping and range of ions in matter (SRIM)” [79], instead of finding an analytic

solution for the Bethe formula. This brings several advantages besides the stated enhanced experimental agreement, for example due to the charge state of the proton which is taken into account and for compounds are corrections available. Further, the scattering in the material can be observed as well as the momentum distribution after passing through a target. The particle energies and also the material compositions and thicknesses can be specified in a user-friendly manner very precisely. A SRIM calculation for the layered setup can be seen in figure 3.10. It shows the energy loss of 2 MeV protons due to ionisations, nuclear effects can be neglected in this energy range. The energy loss is given in eV/Å. To evaluate the dose this has to be multiplied by the particle number and integrated over the range selected.

3.3. Radiation Chamber

An experimental platform was designed to study the effects of laser accelerated protons (LAPs) on mammalian cells. The protons, in the MeV energy range, originate from the rear side of a thin 5 µm Ti foil target following the interaction with a high power laser pulse, and are accelerated by the target normal sheath mechanism (TNSA). A tape Ti foil target was developed allowing a shot repetition rate of up to 5 Hz, which corresponds to the repetition rate of the laser system. A dipole magnet arrangement was used for energy dispersion and to separate the proton burst from electrons and X-rays. The first chamber design was already described in the diploma thesis [80] by Philipp Weiß, which was optimized in the course of time. The absorbed radiation dose at the cell port was repetitively measured with CR39 plastic detectors and calibrated imaging plates.

In the course of this work, an epifluorescence microscope with compact open-beam optics was developed and added to the chamber to image live cells and their spatio-temporal properties during and after irradiation. To demonstrate the functionality of all platform's components, biological proof of concept experiments were carried out using two suspension (Jurkat, Ramos) and two adherent (HeLa, A-549) cell lines. A multitude of biological procedures and analytical techniques were established on site or in laboratories nearby. For example, DNA double strand break (DSB) induction and repair was analysed by detecting the γH2A.X signal with fluorescence microscopy and flow cytometry. The observed dose-dependent increase in DSB induction confirms that DNA damage is induced in cells after exposure to LAPs. In the following, the structure and functioning of the chamber with its supplementary elements will be discussed in more detail.

The design and operation of the platform has already been published in the *AIP Advances* journal [10]. The author's contribution to this publication is discussed in appendix A.

3.3.1. Setup of the Radiation Chamber

The experimental platform (figure 3.6) has been developed with a laser-based proton source at the Arcturus Laser Facility of the University of Düsseldorf [14, 81]. A vacuum chamber specifically built for radiobiological cell studies includes various components primarily for focusing of the laser and guiding the proton beam. The chamber is located in a radiation protection bunker next to the laser room [82].

The laser accelerated protons (as well as other ions) in the MeV energy range leave the target perpendicularly to its rear side. Then they enter a dipole magnet for energy selection consisting of two yokes with magnetic fields oriented opposite to each other which, by way of dispersion, separate the protons according to their energy. These particles then enter the cell port. The protons propagate through a number of thin layers before interacting with the cells. In the following subsections these parts and their functions are described in detail.

3.3.2. Laser Proton Acceleration for Irradiation

As described in chapter 3.1, the Arcturus laser is a dual beam Ti:Sa system using CPA [12]. In the cell experiments shown here only one of the two available Arcturus beams was used. The beam with a diameter of 10 cm is guided to the chamber in vacuum and focused by an f/2 parabola onto the Ti target foil. Thus, the laser beam reaches an intensity of 10^{20} Wcm^{-2} within a focal spot diameter of about 5 µm. With a high contrast laser pulse, protons with energies of several MeVs can be accelerated. The properties of the accelerated protons are discussed in more detail in chapter 4. The ASE laser contrast is for the conducted cell experiments in the range of 10^{-9} in 100s of ps time scale. Since no PM was used, the contrast does not correspond to the maximum achievable. Due to the experimental conditions, the possible rapid shot sequence without a PM was more crucial for cell experiments than a further improved contrast. A more detailed description of the laser contrast can be found in reference [14]. Further, the energy of the beam can be adjusted independently by varying the pumping power or by using attenuators.

There are several different ion acceleration processes, which can be induced by a short high energetic laser pulse. On basis of the experimental parameters, the TNSA mechanism [24, 25] is the most relevant and is therefore described in more detail in chapter 2.1.6.

3.3.3. Tape Target System

Tape targets have been used in our institute for several years [83] and technical improvements have been made constantly, aiming for a stable operation, a high shot repetition rate (particularly for live cell experiments) and a convenient handling.

The working principle of the tape target system is comparable with a cassette recorder. There are two big wheels (diameter 4 cm), on the left is the supply wheel

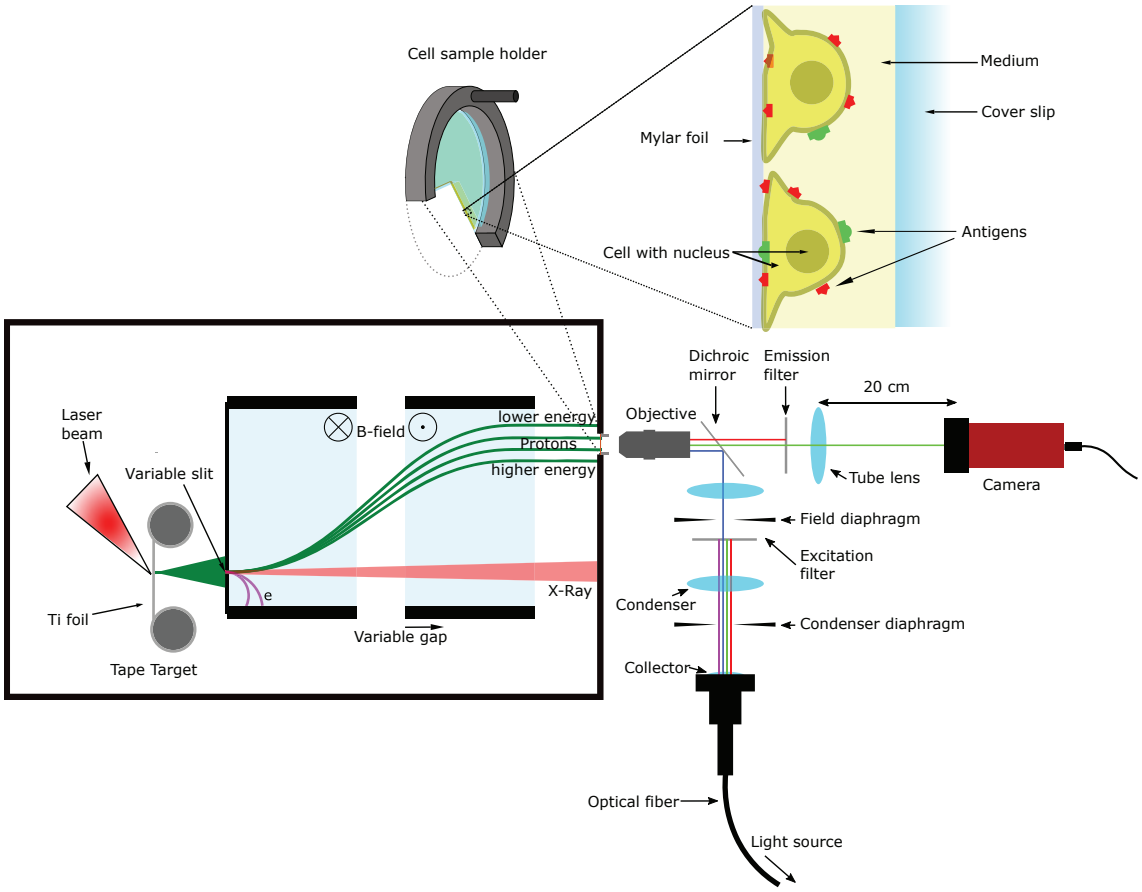

Figure 3.6.: A schematic drawing of the experimental setup. *left:* The **vacuum chamber** for the interaction of the laser pulse (incidence angle 45°) to the titanium foil → ionising radiation can pass through a variable gap normal to the back of the tape target and the laser interaction point. Protons are deflected depending on their energy by a magnetic double yoke. A Kapton® foil acts as the vacuum seal. Behind the foil is the **cell sample holder**, which consists of a steel ring with a 1.5 µm mylar® foil, a coverslip and cells with medium in between (illustrated at the top of the drawing). Protons penetrate though the mylar® foil and the cells. Adherent cells can be grown on the mylar® foil or on a coverslip. *right:* These cells can be observed with an **epifluorescence microscope**. The excitation filter selects the required wavelength range. This light is reflected by a dichroic mirror though the objective onto the cell sample. The dichroic mirror is a triple beam splitter and transparent for the Stokes-shifted fluorescence. Behind the mirror is the emission filter (triple-band filter), positioned at the infinity optics path of the microscope. A tube lens focuses the cell image onto the sensor of the camera.

and on the right the take-up wheel (see figure 3.7). In between are smaller guide rollers to fix the interaction plane and make it independent from the fill levels of the big wheels. The supply wheel was equipped with a 10 m long, 6 mm wide and 5 µm thick titanium foil. This allows up to 2500 consecutive shots before having to put fresh target material into the chamber.

Only the take-up wheel is motorized with a 12 V motor and a rated speed of 4490 revolutions per minute connected to a 439:1 transmission. The supply wheel is curbed and the level of friction can be adjusted. Even though titanium was chosen as target material for its mechanical stability, it can break if the resistance is too strong, since the laser pulse leaves a damage spot behind after each shot. In order to precisely align the target onto the laser beam focal position, the whole construction is mounted on a 3D translation stage. In addition, the tape target can be rotated to control the direction of the proton burst.

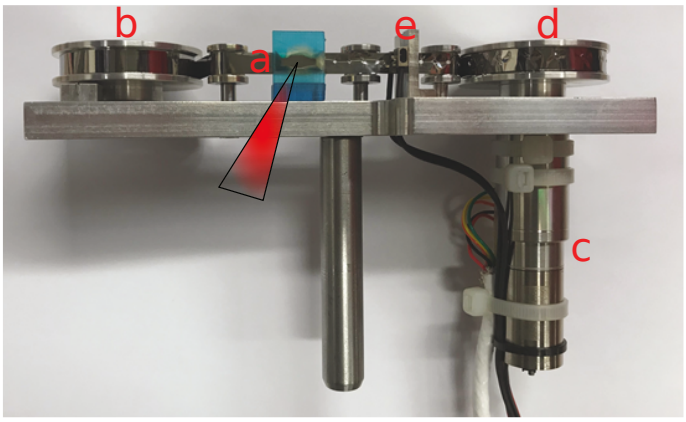

Figure 3.7.: A picture of the tape target mechanism. The laser is focused onto the titanium foil (a) at the position of the blue shield (tip of the wedge). On the left wheel (b) is the new foil, which is unrolled by the motorized (c) wheel (d) on the right. In between shield and right wheel is a light barrier (e) to detect the broken tape.

The control unit, used to move the titanium foil to a new position, has two operating modes. The tape can either be moved to a new position by pressing a button on the control box or the tape movement is externally controlled and synchronised with the laser trigger. The driving distance can be adjusted by changing the voltage pulse duration of the control unit. Furthermore, the control box is equipped with an electronic counter hence the tape consumption can be calculated relatively well. In addition, if problems occur, like a broken tape, which is controlled with a photoelectric sensor, the number of shots can be easily tracked.

3.3.4. Testing the new Tape Target

The tape target system was tested with a four shot sequence of 5 Hz, which is also the maximal repetition rate of the laser. Also longer sequences with 30 shots at 1 Hz (both externally triggered) were tested.

To measure the cut-off energy for shot sequences with up to 5 Hz a MCP detector was used. This detector was chosen because it can easily handle the high shot frequency and initial conclusions can already be drawn about the proton flux. For theses measurements the stepper motor was connected to the laser trigger. In the vacuum chamber the laser beam (see figure 3.6), impinging under a 45° angle, is focused onto the titanium foil.
The proton cut-off energy is 5.64 MeV averaged over 30 shots with 2.5 J laser pulse energy before compression and a one Hz shot repetition rate and the standard deviation is ± 0.54 MeV. For the sequence with 5 Hz and 4 shots the average cut-off energy is 5.78 MeV. The standard deviation is ± 0.37 MeV. This fast sequence was used in only a very limited number of shots and was merely a proof of concept. However, the tape target can be operated in this mode if needed for experiments.

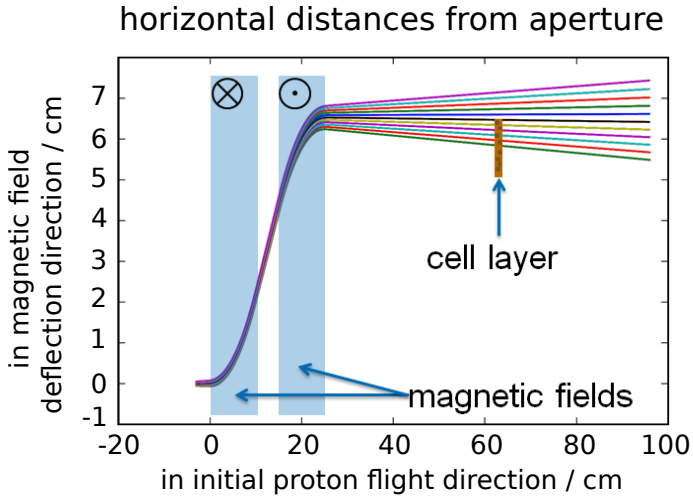

Figure 3.8.: Beam divergence for 2 MeV protons. The sequence of layers considered in the simulation are as follows: They originate from a point source (located 84 mm ahead of the traces) and pass through a 2 mm aperture entering the first magnetic field. The traces are simulated from here over the energy range which is sampled in small steps. The gap between the magnets is 50 mm and the cell layer is located 30 cm behind the second magnet.

3.3.5. Transport and Dosimetry

Since not only protons are accelerated by the interaction of the laser pulse with the target, but also fast electrons and X-rays are generated, a separation and transport system for the protons is necessary. An adjustable slit is positioned in front of the magnetic double yoke 114 mm behind the interaction point of the laser with the titanium foil. Each yoke consists of two parallel Neodym magnets with a size of 100 x 100 mm^2. Between the magnets is a 10 mm gap (along the magnetic field lines). The magnetic field lines of the yokes are anti parallel and the mean magnetic flux density is 0.85 T. The two yokes are connected to each other by a threaded rod, which enables the distance to be varied between 1 cm and 9 cm. This variable gap and the slit width allow to adjust the proton energy and flux at the cell port.
Assuming a negligible slit opening, the variation of the gap from 1 to 9 cm allows to adjust the proton energy from 1.9 to 4.9 MeV in the center of the cell port, before the vacuum seal. For example, in our configuration with a 5 cm gap, the corresponding energy is 3.1 MeV. However, increasing the gap between the magnets, decreases the proton flux at the cell port, due to the LAP energy distribution. The deflection of the protons is schematically shown in figure 3.6 (green proton traces). The protons leave the second yoke as parallel beam, but this is only approximately correct since we cannot neglect the divergence of the TNSA source and the finite size of the adjustable slit, which defines the energy bandwidth of the transported proton beam. The divergence for a 2 mm slit opening and a 2 MeV proton beam is shown in figure 3.8. The calculated initial proton energies in the center of the cell port range from 2.2 to 3.8 MeV for this opening width. For cell experiments presented in this paper the slit was set to 1 mm, which corresponds to half the opening angle and an energy range in the port center from 2.5 to 3.3 MeV. Over the entire cell port of 15 mm the energy ranges from 2.1 to 4.5 MeV. By increasing the slit size, the dose increases while the energy-resolution decreases. (The programme for the numerical simulation of the proton energies is discussed in chapter 3.3.7.) During the experiment the dose was increased by the number of shots, while keeping the energy-resolution constant.

The protons which reach the cell layer can be counted with CR39 plates, which were placed at the same position as the cell layer or behind the cell layer. After exposure the plates were etched for 35 min in a sodium hydroxide solution. Microscopic images of the CR39 plates were taken and the tracks were counted. At the highest pulse energy of the laser, a track density for a single shot of up to 0.44 tracks/

µm^2 was obtained. For light microscopy this is already close to the resolution limit, because approximately 15% of the tracks overlap.

To overcome this limitation AFM images were taken for the same etching time as a proof of principle (see figure 3.4). The tracks had a FWHM between 0.3 µm and 1 µm and a depth between 60 nm and 500 nm. Since the track density was much lower in the AFM sample, the behaviour for two overlapping tracks could not be observed, but it can be estimated that the resolution should be at least twice as good. This would lead to a four times higher measurable track density. Furthermore IPs were used for dosimetry in combination with the calibration for our scanner, which is described in [73]. IP shots were taken periodically in between the cell irradiation to make sure that the dose per shot did not show strong fluctuations. The total dose was determined from the proton spectrum and the tracks counted on the CR39 plates.

Even though the CR39 method can be used to determine very precisely the number of protons, it is a too time-consuming method to be employed for every sample. As a second approach radiochromic films were tested, but as already mentioned the dynamic range or the protection layer turned out to be too large to precisely determine the dose in cell experiments. Since the fluctuations in the proton flux are not negligible for laser driven proton sources and do not average out for low shot numbers or rather small doses, an online dosimetry would be the preferable method. A promising method for the online dosimetry of laser-accelerated protons with scintillators, which was recently published by our group [84] is planned to be implemented in this setup, which focuses on medical applications.

3.3.6. Cell Port

Cells are irradiated using the experimental platform schematically shown in figure 3.6. Protons impinge on a layered setup before they finally interact with the cells. Only protons with initial energies above 1.6 MeV can penetrate the layers and reach the cells. As can be seen in figure 3.9 on the right, there is a second flange where the Kapton® foil is replaced by a 10 µm thick Ti foil. The Kapton® flange was used in live cell imaging experiments due to geometrical advantages. It is worth noting that the observed area is not behind the steel support, as it stops the protons completely. The stopping power of the Ti foil is slightly smaller than the combination of aluminium and Kapton® foil, therefore no change in the energy range for the proton beams is required. The temperature of this flange can be adjusted and controlled by a Pt1000,

a resistance thermometer ($R_{T=0\,°C} = 1000\,\Omega$ and approximately $3.9\,\Omega/K$). In case of cell experiments, the cooling function may be used to reduce enzymatic reactions, for example DNA repair mechanisms. On the other side, as preferred temperature in live cell assays, the flange temperature can be set to 37 °C to prevent a high temperature gradient between the incubator and the irradiation process, as well as to maintain the live cells at physiological temperatures.

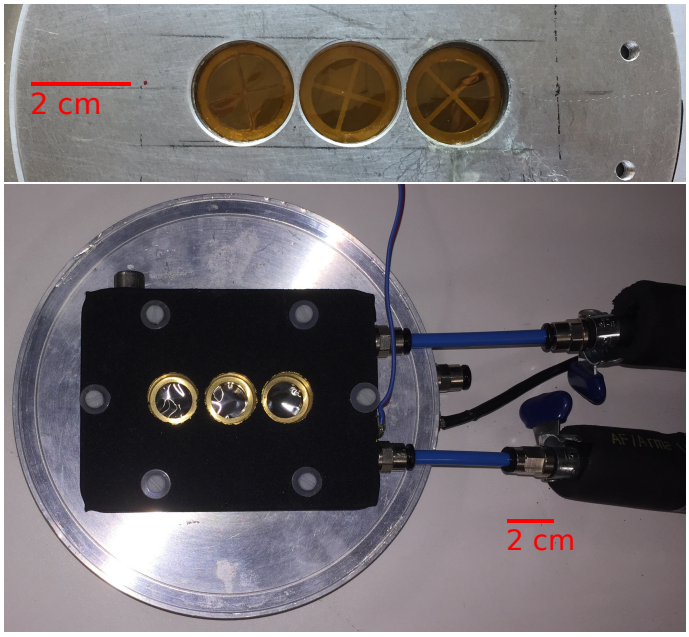

Figure 3.9.: Two flanges with three ports each. The inner port diameter is 2 cm. *top:* The yellow foil is 25 µm Kapton® and behind the foil is a support frame made of steel. *bottom:* Instead of Kapton®, a 10 µm Ti foil shields the vacuum. Further this flange can be cooled or heated and the temperature can be measured with a connected Pt1000. (from [10])

Both flanges have three ports, usually they are aligned in parallel with the dipole dispersive direction; the right port holds the cell sample and the middle one an IP to image the cut-off energy. The left port can be used for control samples. In this case, the X-ray signal must be blocked with a metal plate.

A cell holder is placed in the cell port. It consists of a steal ring with an inner diameter of 15 mm and 1.5 µm thick mylar foil. The foil is glued onto the metal ring with a 2-component epoxy resin for 10 minutes at 100 °C. The cells to be irradiated are located in medium between the mylar foil and a coverslip. Suspension cells are densified to much higher concentrations for this purpose compared to incubation. Adherent cells are either cultured directly on the mylar foil or on the coverslip.

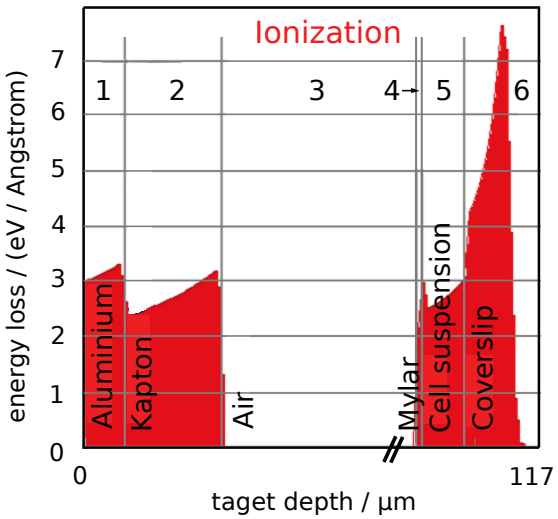

Figure 3.10.: SRIM analysis [79] for 2 MeV protons. In the simulation, the following sequence of layers was used: 1. Aluminium 10 µm; 2. Kapton 25 µm; 3. Air 1000 µm; 4. Mylar 1.5 µm; 5. Cell suspension 10 µm; 6. Coverslip

3.3.7. Simulations

In order to determine the minimal proton energy, necessary to reach the cell layer, the Monte Carlo program *The Stopping and Range of Ions in Matter* (SRIM) [79] was used. In addition, the programme was used to calculate the energy loss of the faster protons in the sample to obtain the energy-dependent mean dose. The deposited energy in the different layers, simulated for 2 MeV protons, can be seen in figure 3.10.

The next step is to adjust the gap between the magnets, as well as the opening slit, to direct the desired energy range to the cell port. For this purpose, the protons deflected by the magnetic field are traced by a particle tracing program. The program is written in Python and the ordinary differential equations solver *scipy.integrate.odeint* was used. For this purpose the magnetic field was measured. The measuring points form a square lattice and the grid point spacing is 5 mm. The program was tested with a homogeneous magnetic field, which was used as input parameter and the result was compared to the analytical solution. The trajectories are simulated for different inlet angles, which are limited by the opening of the slit. This is repeated over the energy range which is sampled in small steps (< 50 keV). The programme structure is adjusted to the IDL code, which can be found in reference [83, p. 125-136]. The version of the source code translated into Python can be

found in the appendix B. Traces of 2 MeV protons can be seen in figure 3.8. Each colour belongs to a different angle of entry, which are homogeneously distributed. In this case, 11 different horizontal angles were simulated; for the other calculations, much smaller angular steps were generally used. For each trajectory, the energy and the position in the plane of the cell port are stored.

3.4. Fluorescence Microscope

The main advantage of an epifluorescence microscope attached to the irradiation apparatus is the live visualisation of cell parts and properties. The possibility to observe the samples with a microscope during irradiation is the unique feature of our setup. To image effects of the LAPs on cellular processes and functions, recordings of the cells during irradiation are needed. For this purpose, the objective must be mounted directly to the irradiation chamber behind the cell port. For this reason it was not possible to use a regular stand-alone epifluorescence microscope and a custom made device was built instead. As the cell sample has a fixed position, the objective has to be moveable and is therefore mounted on a 3D translation stage to set the focus position.

Setup

The schematic setup of the assembled fluorescence microscope developed for this purpose can be seen in figure 3.6. Figure 3.11 shows a picture of the setup. Here, the illumination path, which runs in the horizontal direction, is indicated with a yellow line and the imaging path, which runs in the vertical direction, is indicated with a green line. The absolute positions of the individual components, which are each marked with letters in the image, are listed in the caption.

The imaging path starts from the left with the light source, the C-HGFI mercury lamp from *Nikon* which is connected with an optical fibre to the setup. The brightness of the lamp is adjustable. Only the fibre adapter is shown in the image. In focus distance of the light source is an aperture, the luminous-field diaphragm, to adjust the size of the illuminated area of the specimen, the next aperture is to adjust the depth of focus, which also changes the brightness. Depending on the fluorophore used, a different excitation filter is inserted between apertures. The triple bandpass beam splitter and the emission filter are placed between objective and tube lens in vertical direction. The specifications of the filters are detailed in the following chap-

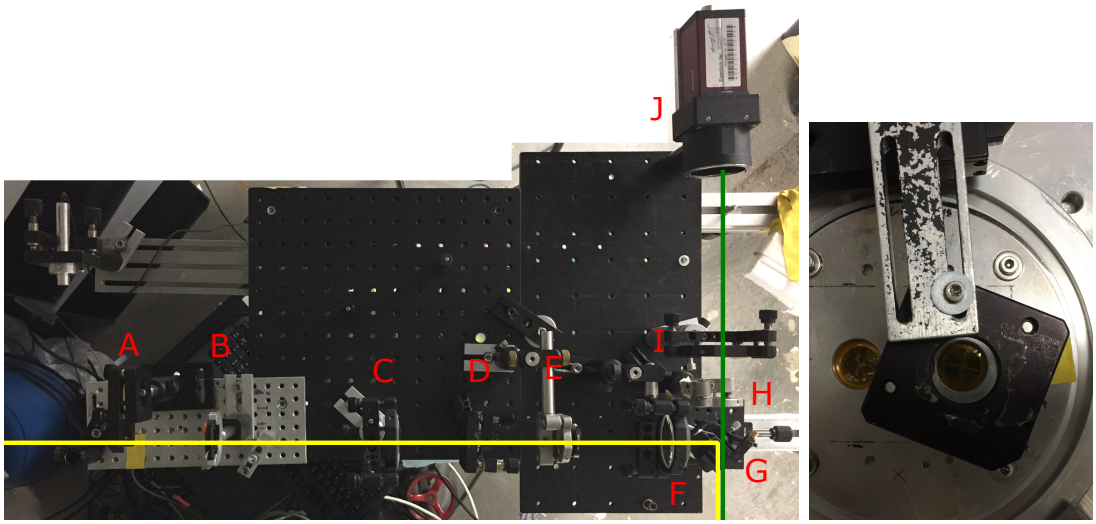

Figure 3.11.: Pictures of the microscope setup with the light path. Yellow: from optical fibre to specimen; green: from specimen to camera. A: light source mount, B: condenser diaphragm, C: condenser, D: excitation filter, E: luminous-field diaphragm, F: lens, G: dichroic mirror (beam splitter), H: emission filter, I: tube lens, J: camera; distances between parts $\overline{AB}$: 4 cm, $\overline{BC}$: 16 cm, $\overline{CD}$: 16 cm, $\overline{EF}$: 8 cm and $\overline{IJ}$: 20 cm. The picture on the right hand side shows the mount for the objective on XYZ linear translation stage.

ter. The microscope is an infinity optical system, so the magnification is determined by the focal length ratio $f_{tubelens}$ / $f_{objective}$.

Different objectives (see table 3.1) were used to observe the cells at different magnifications and resolutions. Two lenses in particular were used, the Olympus air objective with a numerical aperture (NA) of 0.6 and the oil objective with NA 1.25 (see microscopic recording with this objective in figures 3.13, 5.7 and 5.8). Even though the air objective has a much smaller numerical aperture (NA) than the oil objective, it is advantageous for some experiments due to the large working distance (WD) adjustable from 2.7 mm to 4 mm compared to 0.12 mm, respectively. Figure 3.11 (right) shows the objective holder, mounted on a 3D translation stage, into which the various objectives can be screwed. Since no objective is attached in the picture, the cell port behind it can be seen.

3.4.1. Filter

The dichroic filters and beam splitter are from *Semrock Inc.* and distributed by *AHF analysentechnik AG*. The filters have a diameter of 25 mm and a thickness of 2 mm. The beam splitter is a cuboid with the dimensions: 25,2 x 35,6 x 1,1

Table 3.1.: Objective Lenses

manufacturer	magnification	NA	immersion medium	WD/mm
Olympus	40x	0.60	air	2.7 - 4.0
Olympus	60x	1.25	oil	0.12
Motic	40x	0.60	air	2.8
Mitutoyo	20x	0.42	air	20

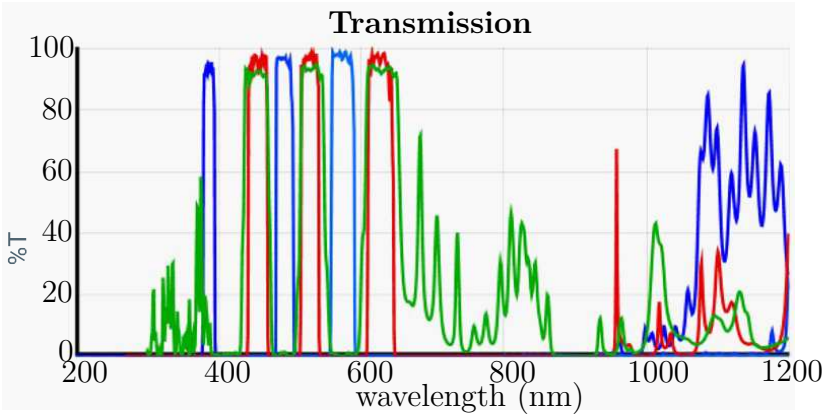

Figure 3.12.: "*AHF analysentechnik AG*": Transmisssion filter set 200 - 1200 nm *blue:* three excitation bandpass filters transmission > 90%: 381.5 - 392.5 nm, 484 - 504 nm and 562.5 - 587.5 nm *red:* triple band emission filter transmission > 85%: 446 - 468 nm, 520 - 540 nm and 614 - 642 nm *green:* triple beam splitter transmission 90%: 446 - 468 nm, 520 - 540 nm and 614 - 642 nm.

mm. Its transmission is shown in figure 3.12 in green. The transmission of the three excitation bandpass filters are highlighted in blue > 90%: 381.5 - 392.5 nm, 484 - 504 nm and 562.5 - 587.5 nm. The triple band emission filter transmission is shown in red > 85%: 446 - 468 nm 520 - 540 nm and 614 - 642 nm (data "*AHF analysentechnik AG*").

3.4.2. Microscope Images

Figure 3.13 shows images taken with the microscope. The left side shows a fluorescence image of a fixed cell sample, which is a superimposed image of the three fluorescence channels available (further information is given in the caption). On the right side, three bright field images of living HeLa cells are shown. The time points were chosen because a cell division can be seen. The complete time-lapse video can be found in the supplementary data of publication [10].

From test images assessing the cell cytoskeletal structures (shown in green) an effective resolution limit of approximately 500 nm is found for the fluorescein isothiocyanate (FITC)-channel (filter 520 - 540 nm, see 3.12). It is possible to record up to 5 frames per second (fps) at the highest resolution and slower rates can be set as desired. Furthermore, the camera (*Pike F-1100*) can be triggered with an arbitrary delay to the laser trigger using a digital delay generator. The exposure time can be varied from 129 µs to 67 s.

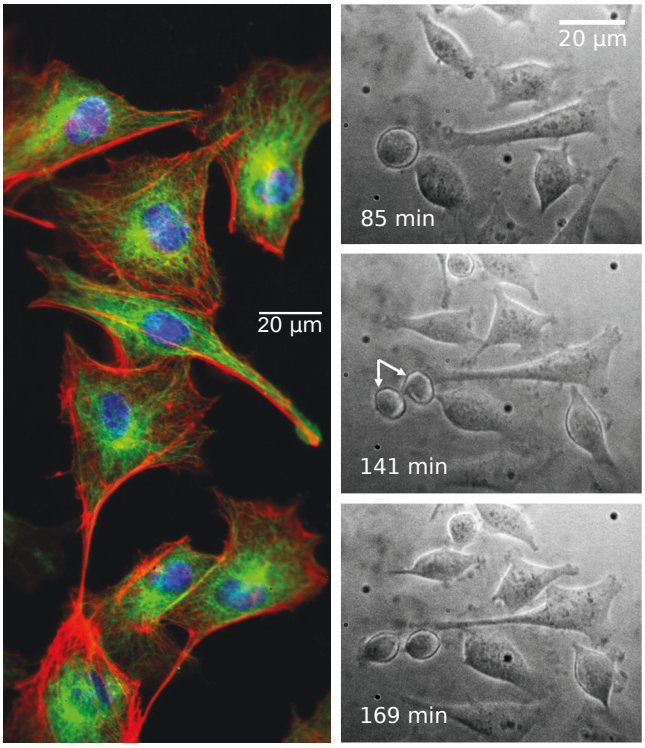

Figure 3.13.: *left:* Recording of immunofluorescently stained fibroblast cells (*Thermo Fisher Scientific Inc. FluoCells™ Prepared Slide #2*) depicting the subcellular architecture (red: actin filaments, green: microtubuli, blue: DNA) with overlay of three recorded channels. *right:* time-lapse recording of HeLa cells, depicting cellular motion and division over 3 hours, as highlighted by white arrows [10].

3.5. Summary

The Arcturus laser facility uses the CPA technique to generate ultra-short pulses with a duration of about 30 fs. The focused intensity of these pulses is in the order of $I = 10^{20}$ W/cm^2. To monitor the pulse-target interaction various diagnostics

are employed, mainly to detect and quantify the protons, which are accelerated by the TNSA process. Furthermore, the energy range and the deposited energy of the protons at the target position are calculated numerically.

The experimental platform described is capable to irradiate various types of small biological samples with LAPs (Ø $<$ 15 mm and a material-dependent depth: for water the maximum is about 100 µm depending on the desired energy range and dose rate) and provides very high dose rates compared to clinically used cyclotrons. The dose of a single shot can be varied from the mGy to Gy level at a maximum dose rate in the range of 10^8 Gy/s, which is about nine orders of magnitude higher than for conventional irradiation.

Cells and fluorescent stains detecting particular cell functions can be imaged by an epifluorescence microscope, which is attached to the chamber, during irradiation or be examined after irradiation. The fluorescence channels of the three dyes DAPI, FITC and Texas Red are available for this purpose. The microscope camera can record at up to 5 frames per second (fps) or be timed with the laser pulse. The microscope has a flexible, open-beam setup thus components can easily be exchanged or placed in the beam path, e.g. to switch between fluorescence channels, to adjust the contrast or change the objective.

Due to the tape target design the time lag between shots can be reduced to the laser repetition rate, which is 0.2 s. This allows probing of a broad range of doses within in a short time.

Here, only the possibilities for irradiation and analysis with the setup were shown. The irradiation experiments performed on cells with the platform are described in more detail in chapter 5.

4. Source Development: Two Beam Configuration

Previous experiments performed at the Arcturus laser facility have shown that LAPs produce less nitro-tyrosine in A-549 cells compared to a continuous proton irradiation, whereas the yields of DSBs were not significantly different for the investigated doses [9]. Potentially, the high dose rates of LAPs cause less oxidative stress overall than conventional proton irradiations. This might be an evidence for an *in vitro* induced FLASH effect (see chapter 2.2.4). Although it is well known that a high dose rate is responsible for this effect, it raises further exciting questions about the correlation of produced reactive species in cells with the temporal dose distribution of the irradiation. For LAPs, the dose rate of a single shot is generally very high, but the total averaged dose rate in an irradiation series of several shots can be very low due to the time interval between the shots. Thus, for example, the dose per shot as well as the dose rate of a single shot are interesting parameters to investigate with regard to the FLASH effect.

This chapter describes experimental techniques to is increase the parameter range for the proton pulse by using both beams of the Arcturus laser system in order to be able to address such issues. The aim is to extend the possibilities of investigating LAP irradiation. Mainly it is about providing the possibility to vary the dose rate.

Parts of this experiment are published in the master's theses of Abdulraouf Kutaish [85] and Marco Dittrich [86], who also evaluated a part of the MCP images.

4.1. Experimental Setup

For two beam experiments the setup was moved to "Chamber 2" [82, p. 41], which has access ports for both beams. The tape target system is further used. An illustration of the experimental setup is shown in figure 4.1. In addition to the previously implemented beam ("Beam 2") the second beam ("Beam 1") is focussed

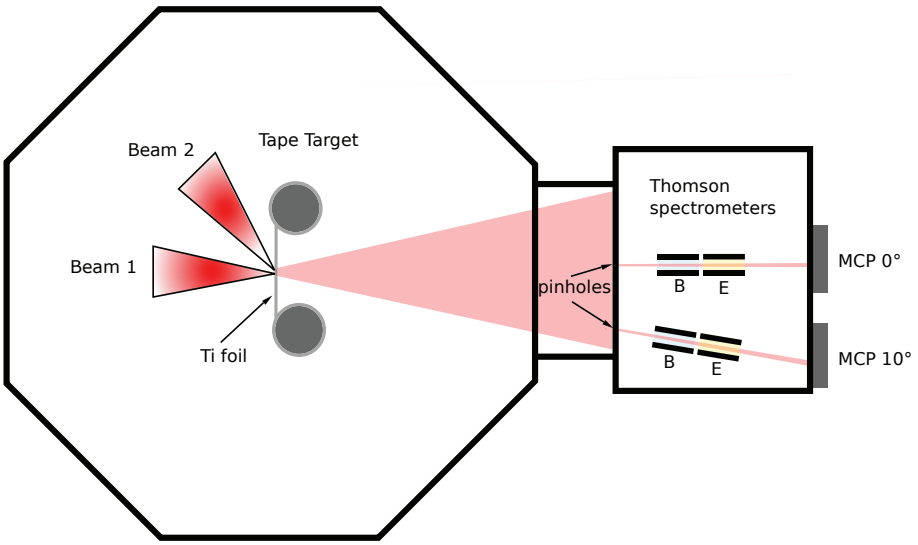

Figure 4.1.: Schematic illustration of the experimental setup. Both laser beams are focused onto the tape target. Two pinholes are used in order to provide a proton pencil beam in 0° and in 10°, respectively, for the Thomson parabola - MCP arrangements.

onto the foil at normal incidence. (The designation number goes back to the order in which the beams of the Arcturus laser were mounted when the system was first put into operation.) The beams can be focused, positioned and shot independently.

For a temporal variation of the proton bursts either a single or two intense pulses interacted with a thin foil target. The delay between the two pulses was adjusted in the experiments between zero and 6 ns by varying the distance they travel. Two interaction conditions were used. Either both pulses interacted with the target at the same interaction point or the beam interaction points were horizontally separated by a distance of up to 1 mm. For the two beam experiments, the plasma mirror systems [59, 60] were used to avoid strong back reflections, which could be harmful to the laser due to the normal incidence of “Beam 1” and further to improve the laser contrast.

As before, f/2 parabolic mirrors were used to focus the laser pulses. Since the aim of this setup was to provide further possibilities for particle therapy on cell layers, diagnostics were set up to measure the ion energy and flux, with particular interest in the protons. The ions accelerated in a cone normally to the rear of the target were examined at two different angles. For this purpose, two pencil beams were generated from the broad TNSA beam via pinholes. One pinhole had an angle of 0° relative to the target normal interaction point and the other an angle of 10°.

The distance from the pinhole to the target was 70 cm. The accelerated ions are diagnosed by a TPS, each of which has a MCP as detector. Both, the TOF-MCP and the imaging MCPs were used.

For the imaging MCP TPS setup, each trace corresponds to a specific charge-to-mass ratio (a brief presentation of the theory can be found in chapter 3.2.1). For the spatially separated interaction points a MCP image is shown in figure 4.8 on the right. As can be seen, the ion tracks and the X-ray signals of "Beam 1" and "Beam 2" are horizontally offset, depending on the distance between the two interaction points. (For comparison, figure 3.2 right shows a TPS recording with only one interaction point.)

To record time resolved signals, an imaging MCP was replaced by a TOF-MCP. In this setup, the pulses are now distinguished by measuring the temporal distance between the signals of incoming ions and the X-rays generated during the laser/target interaction. Based on the temporal and spatial (target - detector) separation, the energy of the ions can now be determined. However, since the time-of-flight differences of the ions arriving on the detector are significantly larger due to the different energies than the time distance of the two laser pulses, only a small part of the spectrum was used to generate short ion pulses. For this purpose most of the ion spectra are blocked by a metal shield that is placed behind the Thomson parabola (see figure 4.8 left), while only a part of the ion spectra, which arrives at the height of the slit reaches the time of flight-MCP.

4.2. Experimental Results

The results of the two beam experiments are divided into two parts. First, the results of the tests with spatially overlapped interaction points for both beams are presented and in the next part for spatially separated interaction points. Since the latter configuration offers far more application possibilities in radiation biology, it will be discussed in more detail here.

4.2.1. Temporal Beam Synchronisation

Since the time interval between the pulses is varied for both experimental parts, the pulses must be temporally synchronised beforehand. A first step in this process is to use a photodiode on which the two laser beams are focused and the signals

are read out by an oscilloscope. With this method, it is already possible to achieve a temporal accuracy of the beams well below one nanosecond. However, since the beams should be matched to each other in the range of a few ps for the experiments, this accuracy is not yet sufficient.

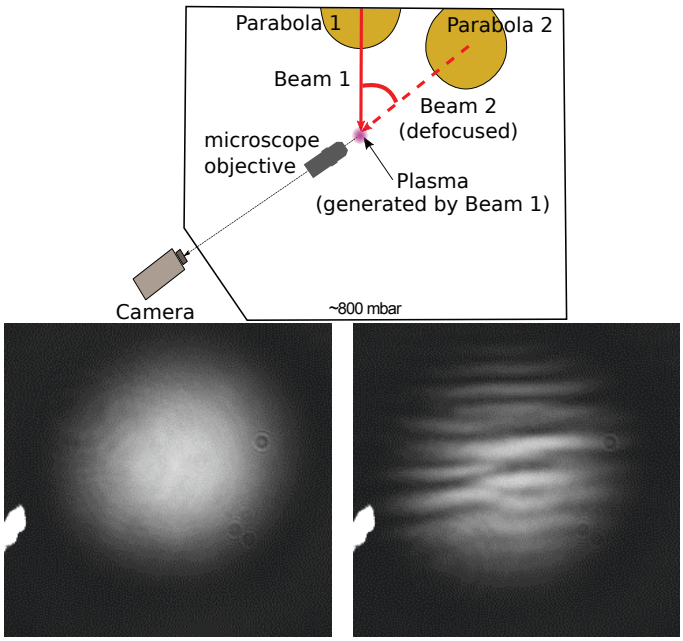

Figure 4.2.: Synchronisation method, *left:* experimental setup (reworked from [86]); *middle and right:* images of the defocused "Beam 2". *middle:* undisturbed recording of the defocused beam, *right:* the delay of "Beam 2" was increased by 15 ps and clear deformations in the beam profile can be seen.

A significantly higher temporal accuracy can be achieved by generating a plasma with one beam and probing it with the other beam. This method was used for a further temporal adjustment of the pulses. The experimental setup, together with two exemplary images, can be seen in figure 4.2. For this purpose, the focus of "Parabola 2" is moved slightly out of the focal plane of the imaging system to illuminate a larger area. In addition, the intensity of the defocused "Beam 2" is also reduced to such an extent that the intensity is much lower than necessary to ignite a plasma. The intensity of "Beam 1", on the other hand, must be sufficient to ignite a plasma (this is the case starting at about 10^{14} $\frac{\mathrm{W}}{\mathrm{cm}^2}$, so only a tiny fraction of the maximum laser intensity is required). Furthermore, in order to image the plasma, there must be sufficient particles in the focus of "Beam 1" that can be ionised. The measurement was therefore not carried out under vacuum, but at approximately atmospheric pressure. As can be seen in figure 4.2 *right*, the image does not show a

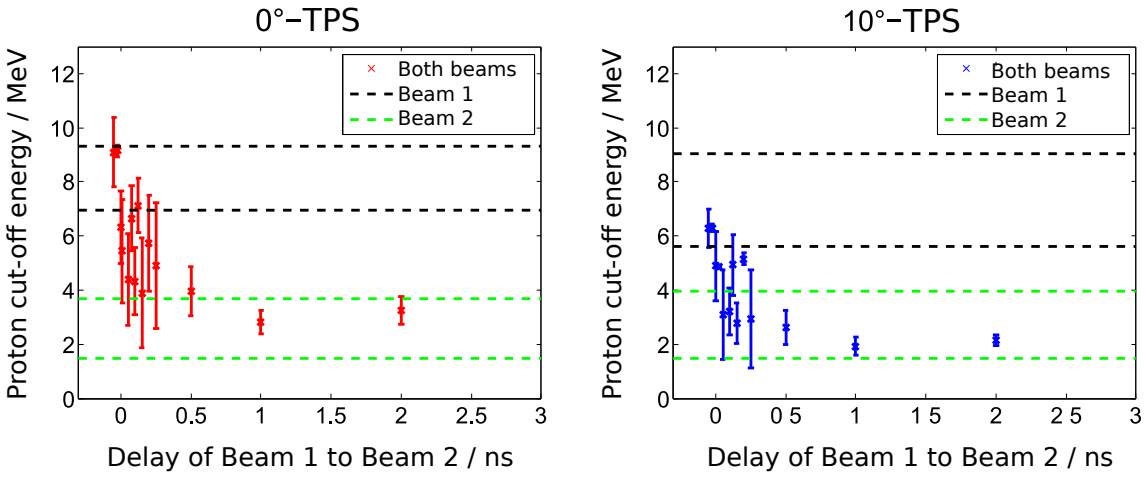

Figure 4.3.: Proton cut-off energies for different delays of "Beam 1" to "Beam 2", MCP images evaluated by Marco Dittrich. The dashed lines indicate the range of the standard deviation for each beam. *left:* TPS at normal incidence; *right:* TPS at 10°.

blob of plasma, but multiple plasma channels, which is due to the filamentation of the laser beam in air.

4.2.2. Overlapping Interaction Points

If both beams are focussed at the same point on the titanium foil, the resulting ion spectra of both pulses, recorded with a Thomson parabola spectrometer, overlap on the MCP. Thus, the two spectra cannot be distinguished from each other and no statement can be made about the individual interactions of the beams. But for greatly different cut-off energies obtained by the individual interactions, the resulting spectra of the temporally timed interactions can be compared with those of the respective individual beams.

To measure the contribution of the later pulse, the intensity of the prior pulse ("Beam 2") was strongly decreased by reducing the pumping power and by defocussing. Consequently "Beam 2" generated a much lower cut-off energy compared to the stronger pulse from "Beam 1". The pulse energy before compression were 4.7 J for "Beam 1" and 2.4 J for "Beam 2".

In the diagrams 4.3 the cut-off energies are plotted depending on the delay of the two beams, as well as the cut-off energies for the single beam cases. For the single beam cases, measured with the 0° TPS, the single beam cut-off energies were (8.1± 1.2) MeV and (2.6± 1.1) MeV, respectively. For a negative delay (interaction of

"Beam 1" first) the mean resulting cut-off energy was 9.1 MeV for -50 ps and nearly identical for -25 ps with 9.2 MeV. Both values are slightly higher than in the single beam case but the values are still within one standard deviation. For the temporally synchronised case (uncertainty $\approx$ 1 ps), the mean cut-off energy is already reduced and below one standard deviation of the single beam case. Due to the scatter of the data points, no exact trend can be given for the first 250 ps, but from a delay of 0.5 ns onwards, the cut-off energy is significantly further reduced. With a beam delay of 1 ns the cut-off energy is in the uncertainty of the low intensity single beam case. For the cut-off measurement at an angle of 10°, the same trend is seen. Here, however, the cut-off energies of the double-beam tests are somewhat shifted towards lower energies compared to the single-beam measurements. It can be concluded that the contribution of the delayed pulse to the proton signal strongly decreases within the first 0.5 ns and disappears after a delay of less than 1 ns.

Discussion

The interaction of two temporally tuned beams with a target results in various physical effects. The plasma generated at the front of the target, also called pre-plasma, influences the absorption of the laser pulse and has completely different properties for the second pulse as for the first. The absorption in turn influences the electron temperature, which is an important parameter for the electron sheath at the rear side of the target. In general, a higher absorption of the laser energy in the preplasma leads to hotter electron temperatures, which in turn lead to stronger electrostatic acceleration fields at the rear side. On the other hand, a steep density gradient must be present at the target rear for successful ion acceleration, but this gradient is also affected by the first pulse.

Comparable two beam experiments have already been described in the literature, both theoretically and experimentally [87–89]. In publication [88] they detected a strong increase in the absorption of the laser pulse energy and in the conversion efficiency into kinetic proton energy. For timed pulses with an energy ratio of 1:10, the weaker beam arrives first, the cut-off energy increased for a delay of 0.75 ps by more than 30%. These experimental results were also confirmed numerically (here, the simulated conditions differed noticeably from the experimental ones). However, these results are only to some extent comparable with those obtained in this work, since the gold target of 100 µm was 20 times thicker than the titanium target used here and the delay times also cover a much smaller temporal range. The most

decisive factor is probably the different pulse durations, which at 0.7 ps correspond to more than 20 times the pulse duration used here. For longer pulses, resonance absorption plays a greater role compared to vacuum heating and $\mathbf{j} \times \mathbf{B}$ heating, which require a much steeper density gradient and are more relevant for absorption in the case of ultrashort pulses (see chapter 2.1.5). Thus, the prepulse may offer advantages in one regime but disadvantages in the other, so publication [89] is more appropriate for comparison. Here, both the laser pulses and the target thicknesses are very similar to those in this thesis. In order to obtain two pulses that are tuned to each other in time, a single pulse was divided into two equivalent pulses by a split mirror, which allow a pulse delay between 0 and 2 ps. When the pulses impinge simultaneously, the highest proton cut-off energies were measured. When compared to a single laser pulse of half the energy, however, increased cut-off energies could still be measured, depending on the target thickness, up to a delays of 0.6 ps (3 µm Al) and 1 ps (6 µm Al). Numerical simulations of the experiments were used to investigate these results. Also here, an increase in absorption by the preplasma on the target front side was found, which led to a significantly increased electron temperature. However, the steepness of the density gradient on the back side of the target has already decreased, which significantly reduces the effectiveness of the second pulse for ion acceleration despite higher electron temperatures (see chapter 2.1.6). In the work [85] the plasma expansion at the front and at the rear side of the target are estimated 1 ns after the interaction for the conditions in this thesis to be around 370 µm and 200 µm, respectively. This far greater scale length suppresses successful ion acceleration. However, as can be seen in figure 4.3, an increase in the cut-off energy is measurable for a significantly longer time than found in publication [89]. This will primarily be due to a much higher beam intensity of the delayed pulse. The trend is evident for both measured angles, whereby the respective energies for 10° are significantly lower than for 0°. The decrease in cut-off energies for increasing angles to the target normal is generally observed in the TNSA process [30]. For a more accurate comparison of the two experiments, the pointing stability must also be taken into account. Since the two beams are separated much earlier here and are focused via two separate parabolae, the pointing stability of the two beams in relation to each other will be noticeably lower. This is certainly one reason for the measurement uncertainties at a delay of up to 250 ps.

An effect of the delayed pulse was no longer measurable in this setup after less than 1 ns and thus offers no possibility to flexibly adjust the dose rates. Further-

more, neither the ion flux nor the cut-off energies are significantly increased, so that overlapping beams have no visible advantage for cell irradiation.

4.2.3. Separated Interaction Points

The separation of the laser interaction points of the two beams can be controlled in the 10s of µm range. However, it is necessary to be able to distinguish the accelerated ions originating from the individual interaction points. Since the distances of the ion sources to each other, as well as the pinhole size and the distances between ion source and pinhole and MCP are known, the minimum distance at which the tracks would be separated on the detector can be calculated using Thales's theorem (see illustration [85, p. 36]). For the experimental conditions 0.5 mm beam separation should be enough to resolve the traces. However, as can be seen in the exemplary images shown in figure 4.4 the individual traces and cut-off energies are not sufficiently separated.

In order to detect distinct traces on the MCP and to be able to obtain the individual ion spectra, a distance of 1 mm is chosen. As can be seen in figure 4.4 and 4.8 the proton traces can be well distinguished for the whole recorded spectrum, whereas traces of other ion species merge partially for lower energies. The interaction points are separated in parallel to the defection of the electric field of the TPS. Therefore, the traces are getting closer if the contribution of the electric field to the deflection increases. For ions, which are detected on the screen, a smaller charge-to-mass ratio leads to a stronger electric field dependency. Additional the MCP has a limited resolution and the ion source size is not infinitely small. However, the proton spectra are most relevant, since only protons are used for the irradiation of cells.

To investigate whether the ion acceleration processes still influence each other relevantly at an interaction distance of 1 mm, the respective cut-off energies were measured for different beam delays under 0° and 10°. Figure 4.5 shows the mean cut-off energies for the respective delays with the corresponding standard deviations. As can be seen, no significant delay dependent changes in the proton cut-off energy compared to the single beam case were observed. In contrast to the measurement described above, there is no decrease in the cut-off energies for larger angles to the target normal. Since this effect seems to be independent of the delay, it is possibly due to a less precise adjustment of the target relative to the MCP and not a two-beam effect. However, this only marginally affects the informative value of the measurement, as any other small angles to the target normal could have been set.

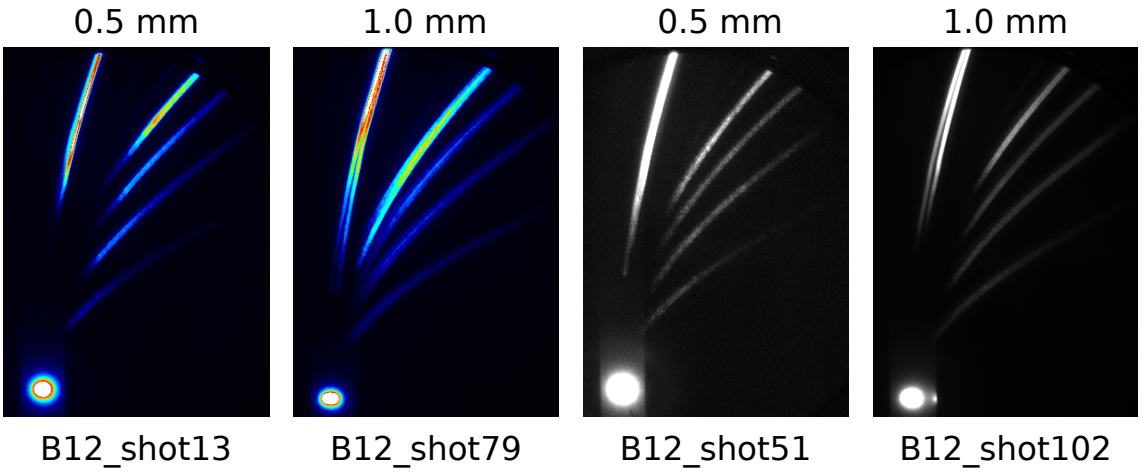

Figure 4.4.: Four different example TPS recordings for 0.5 mm and 1 mm separations of the interaction points. Shown in *left:* false colours *right:* grey values.

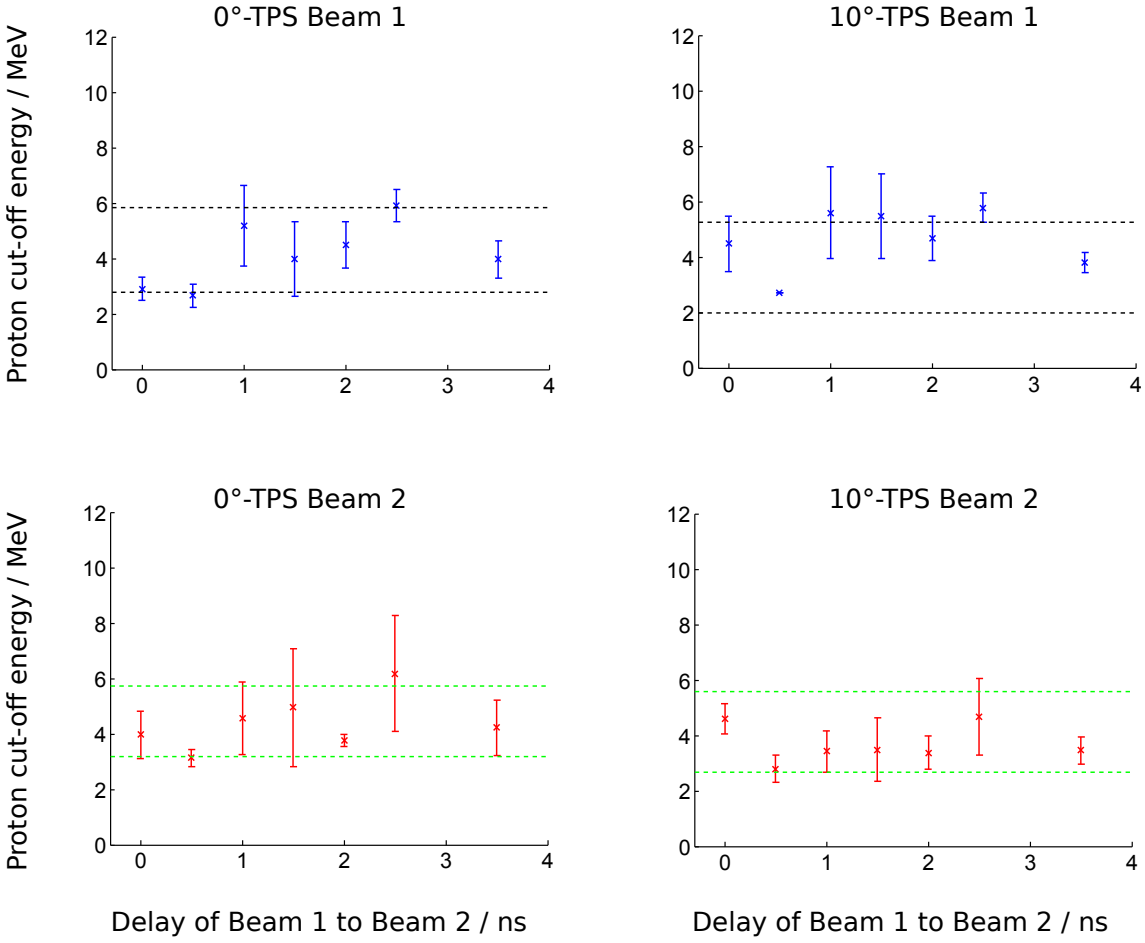

Figure 4.5.: Proton cut-off energies for 1 mm separated interaction points. *top:* cut-off energies for "Beam 1"; *bottom:* cut-off energies for "Beam 2"; *left:* 0° TPS; *right:* 10° TPS. The dashed lines mark the standard deviation of the respective single beam measurements. (revised from [86])

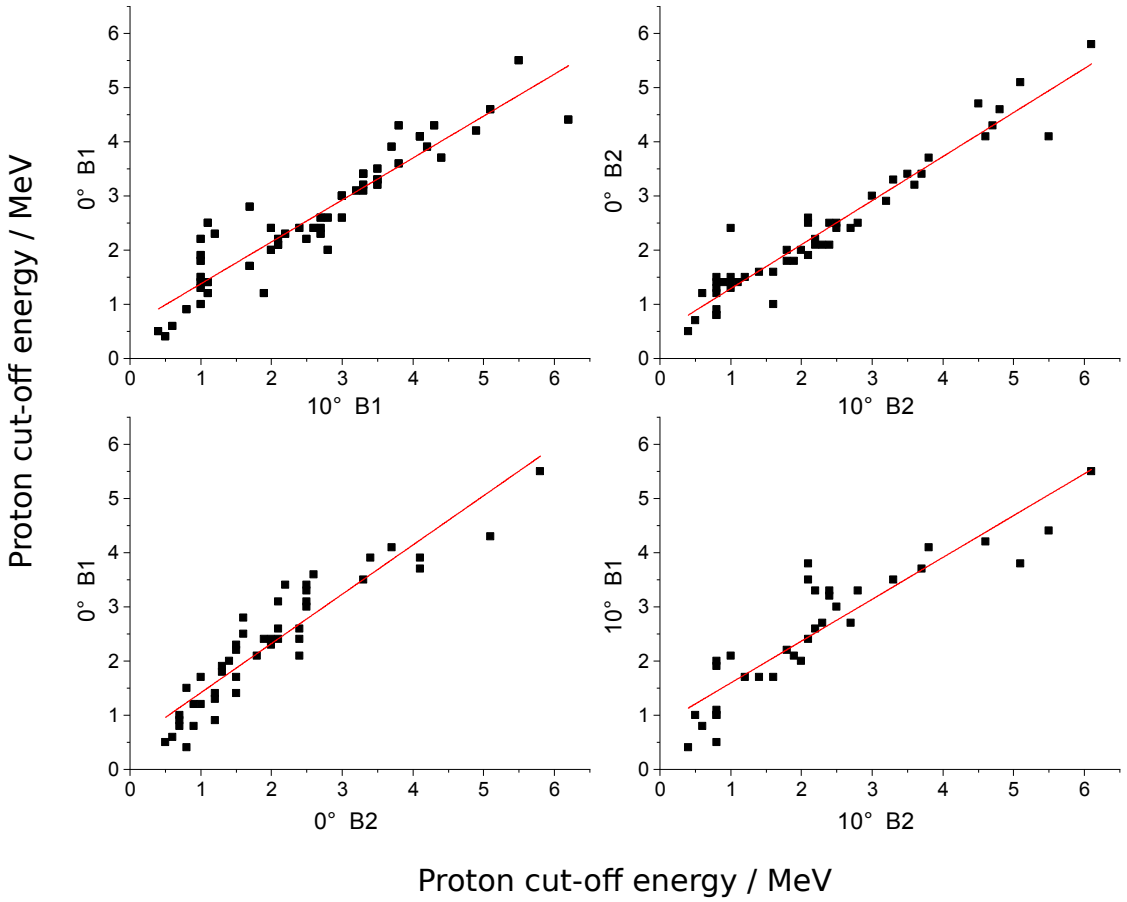

Figure 4.6.: Proton cut-off energies for 1 mm separated interaction points. Each black square shows one double beam measurement. *top:* cut-off energies measured with the 0° TPS against the 10° TPS for "Beam 1" on the left and for "Beam 2" on the right. *bottom:* cut-off energies for "Beam 1" against "Beam 2" on the left measured with the 0° TPS and on the right with the 10° TPS. In red the respective best fit lines are shown.

Apart from the expected correlation between the 0° and 10° cut-off values for one interaction, the diagrams also hint at a correlation between the proton cut-off energies of the two timed beams. To further examine these two possible correlations, proton cut-off energies of the respective beams and angles are plotted against each other in figure 4.6. A measurement series with cut-off values over a wide energy range was used for this. As can been seen there is a strong correlation between the 0° and 10° cut-off values for each beam (upper two diagrams), but also for the two beams against each other, both under 0° and 10° (lower two diagrams). Due to the apparently linear distribution of the data (see red best fit lines), the Pearson correlation coefficient

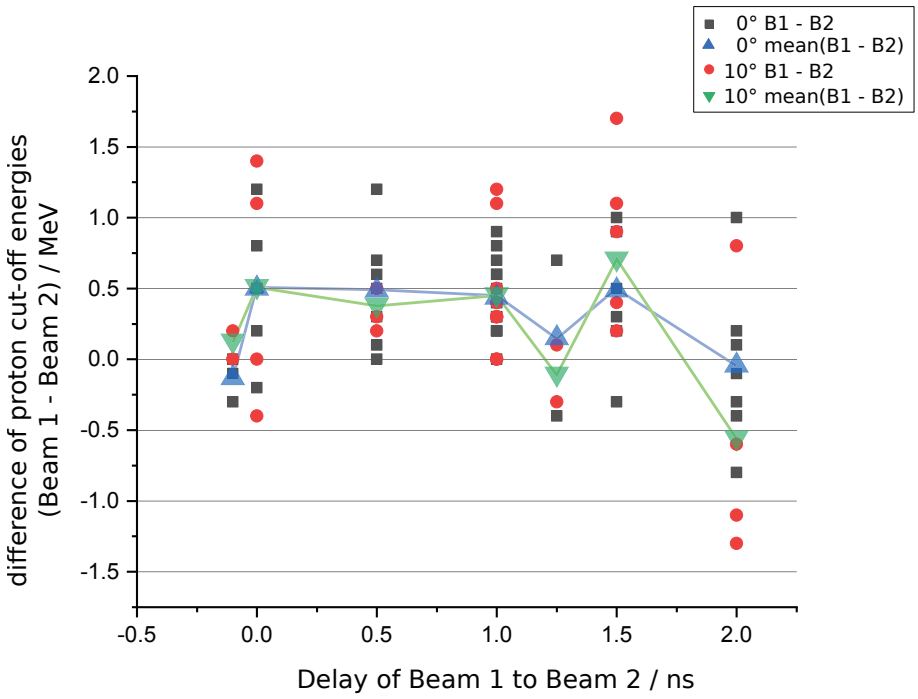

Figure 4.7.: Differences of proton cut-off energies for 1 mm separated interaction points under 0° and 10° against the delay time. The mean values are given in each case and connected with a line to guide the eye.

$$R_{x,\,y} = \frac{\sum(x_i - \bar{x})(y_i - \bar{y})}{\sqrt{\sum(x_i - \bar{x})^2 \sum(y_i - \bar{y})^2}} \tag{4.1}$$

was calculated to quantify this hypothesis. $R_{x,\,y}$ can take values in the range from -1 to 1, where -1 indicates a perfectly negative linear relationship, 0 an absence of linear relationship and 1 a perfectly positive linear relationship. For "Beam 1" the coefficient is $R^{\mathrm{B1}}_{0°,\,10°} = 0{,}93$ and for "Beam 2" $R^{\mathrm{B2}}_{0°,\,10°} = 0{,}97$. Both values are close to one, so the correlation tends to be a largely positive linear relationship between the 0° and 10° proton cut-off energies. The cut-off energies for "Beam 1" 0° against "Beam 2" 0° $R^{0°}_{\mathrm{B1,\,B2}} = 0,93$ and for "Beam 1" 10° against "Beam 2" 10° $R^{10°}_{\mathrm{B1,\,B2}} = 0{,}91$ have an almost equally high correlation coefficient, so that a largely positive linear relationship is also observed here.

In this context, the further investigation of a possible correlation between the beam delay and the cut-off energies is of course of interest. In the diagram 4.7 the difference of the proton cut-off energies of "Beam 1" and "Beam 2" are plotted against the beam delay. Values greater than zero indicate a higher proton cut-off energy of "Beam 1" and negative values indicate a higher cut-off energy of "Beam

2". The absolute values were not taken in order to reduce errors due to fluctuations over the course of the experiment. The 0° (blue) and 10° (green) mean values are each connected with a line to guide the eye. No correlation is evident here and the Pearson correlation coefficients $R_{0°,\,delay} = -0.13$ and $R_{10°,\,delay} = -0.19$ are also close to 0, as expected.

TOF Experiments

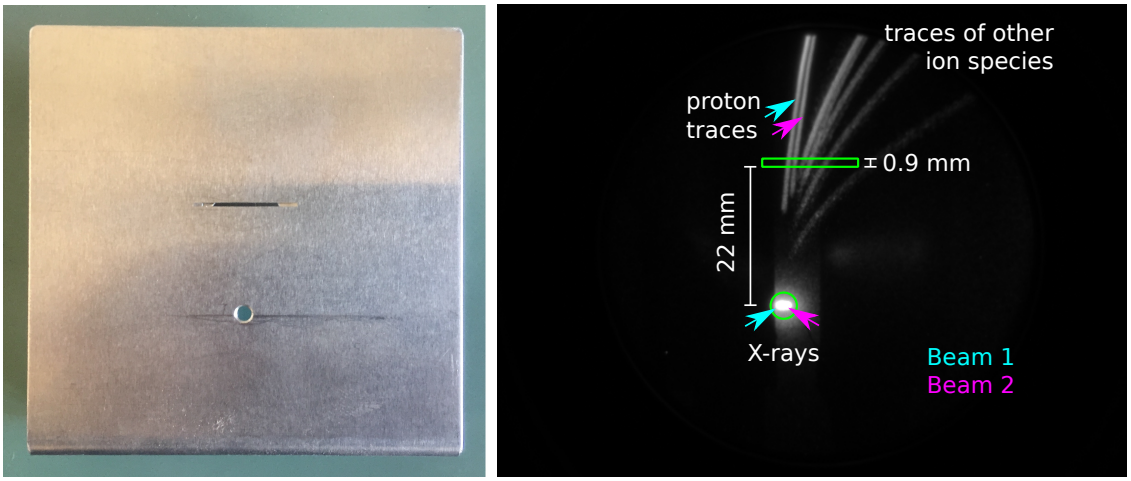

Figure 4.8.: *left:* Metal shield, which is placed in front of the MCP detector in order to allow to pass only a part of the ion spectrum (slit) and the photon signal (round hole). *right:* MCP image showing the traces of the accelerated ions and the X-ray signals, indicated by arrows. The interaction points of the two laser beams are spatially separated by 1 mm. The shield opening positions are marked in green, the rectangular slit for part of the ion spectrum and the hole for the X-ray signal.

These experiments were performed to assess the experimental platform's ability to stretch proton beams with a specific energy bandwidth. In order to measure the actual impinging time of the ions the TOF-MCP (see chapter 3.2.2) is employed. In contrast to the experiments before where the impact positions of the ions are visualised on a screen, now the impinging ions are time resolved with an oscilloscope. Due to the travel distance between the titanium foil and the TOF-MCP, ions hit the detector at different times depending on their speed. The acceleration time can be neglected due to the time resolution of the TOF-MCP (700 ps FWHM), as well as due to the energy resolution of the ions in relation to the travel distance. As before the beams are separated by 1 mm on the target. For the signal recording with the TOF-MCP read out with an oscilloscope (cf. graphs in figure 4.9) most of

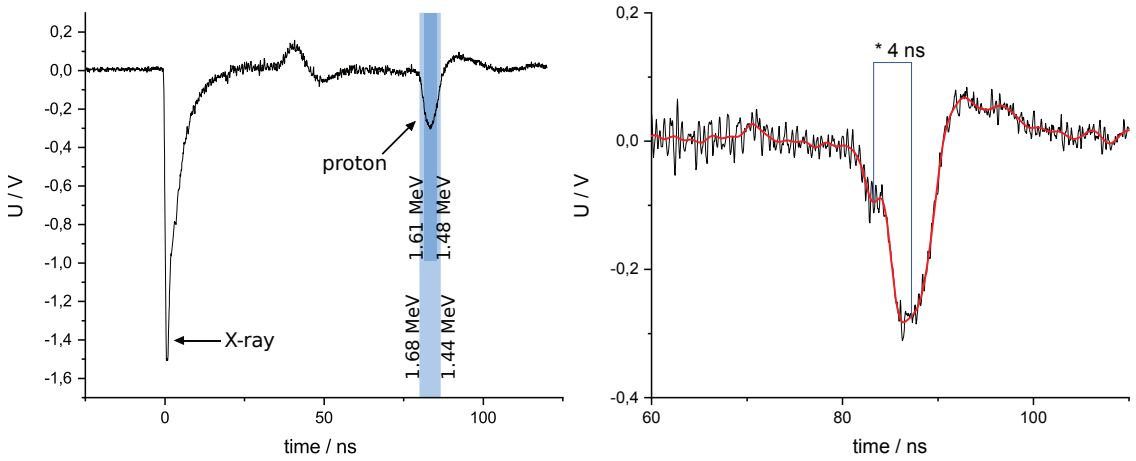

Figure 4.9.: TOF-MCP signals measured with an oscilloscope, proton travel distance: 152 cm, trigger (0 ns): X-ray peak, proton peak in the range of 80 - 90 ns *left:* Single laser pulse, with the proton signal highlighted in light blue and its FWHM drawn in blue. The corresponding proton energy ranges are given in each case. *right:* proton signal generated by two laser pulses with a delay of 4 ns. The different amplitudes indicate interactions of unequal effectiveness, red line: fast Fourier transform low pass filter 500 MHz.

the ion spectra are blocked by the metal shield, which is shown in figure 4.8 on the left. This ensures that only a small energy range of the respective ion type hits the detector and thus the signals of the two beams overlap less and can be separated. Further there is a hole for the X-rays in the metal shield, which gives the reference signal on the oscilloscope. The slit and hole are shown schematically on an MCP image in figure 4.8 on the right.

The time interval between the photon and proton signal is

$$t = \frac{s}{v} - \frac{s}{c}, \tag{4.2}$$

with the distance s between target and TOF-MCP, the speed of light c and the particle velocity

$$v = c \cdot \sqrt{1 - \left(\frac{E_{kin}}{mc^2} + 1\right)^{-2}}, \tag{4.3}$$

where m is the mass of the particle and E_{kin} is its kinetic energy.

For the proton peak signal, this corresponds to a centre energy of 1.56 MeV in the chosen setup. The FWHM of the peak is 4 ns and ranges from 1.61 MeV for the lower edge to 1.48 MeV for the upper edge of the slit. This geometry was tested for delays up to 5 ns and there was no indication that it cannot be used with much

longer delays. Figure 4.9 (right) shows that the two proton pulses start to separate for a delay of 4 ns. The resolution is mainly limited by the divergence due to the slit and the pinhole and not by the time of flight-MCP. With the existing setup first separation effects can already be measured for a relative delay of 3 ns of the laser pulses. For typical cell experiments, the irradiation time of a cell is about 5 ns due to the different travel times of the protons (centred on the cell port 3 ± 0.6 MeV).

Discussion

To further develop the experimental scope, it should be possible to irradiate cell samples with variable LAP dose rates. Both beams of the Arcturus laser system were used for this purpose. As experimentally demonstrated, the most promising arrangement is that of separated interaction points. In order to homogeneously irradiate samples for biological applications an overlap of the accelerated particles is desired, wherefore the distance between the interaction points of the beams on the target should be rather small. For this purpose, a distance of 1 mm is a good compromise. As can be seen in the evaluations of the cut-off energies for the mutually delayed beams (figures 4.5 and 4.7), this distance leads to two largely separate TNSA events, which makes this configuration suitable for cell experiments where the dose rate is changed. Due to the orthogonal orientation of the magnetic field of the double yoke for cell experiments to that of the TPSs, the two separated interaction points would each lead to different proton energy ranges on the cell sample. This may be intentional, but if not, there would be enough space on the 6 mm wide titanium foil to arrange the interaction points on top of each other, which would probably limit the foil stability. Another possibility would be to rotate the tape target system by 90°, because of the holder, this rotation could be easily implemented experimentally. In both cases, only the shielding in front of the film would have to be reworked.

The range in which the dose rates can be adjusted extends from more than 10^8 Gy/s to less than 10^6 Gy/s for each pulse. The dose rates cannot be set completely independent of each other, as the slit size in front of the magnetic double yoke and the distance from the target to the cells are identical. Furthermore, it is theoretically possible to reduce the dose rate of a shot even further, but then the number of shots must be increased substantially to achieve the same dose.

4.2.4. Horizontal TPS-MCP Traces

By the TNSA mechanism, only charged particles from roughly a single point can be accelerated and then pass through the TPS, so only ion signals should be detected on the MCP detector, apart from the zero point. Furthermore, the charged particles should have a continuous spectrum up to the cut-off energy, so each track on the MCP should partially correspond to a parabola. However, on various TPS-MCP recordings, horizontal traces can be seen emanating from the pinhole and pointing only in the deflection direction of the electric field for the positive ions (see figure 4.10). Some of these traces end in the pinhole signal and a beginning of the line is not discernible, but there are also traces that only start at a clear distance from the pinhole. These signals appear on both the 0° and the 10° MCPs and on different measurements. Since the electric fields of the TPSs are completely separated from the MCPs, a consequential measurement error can be excluded.

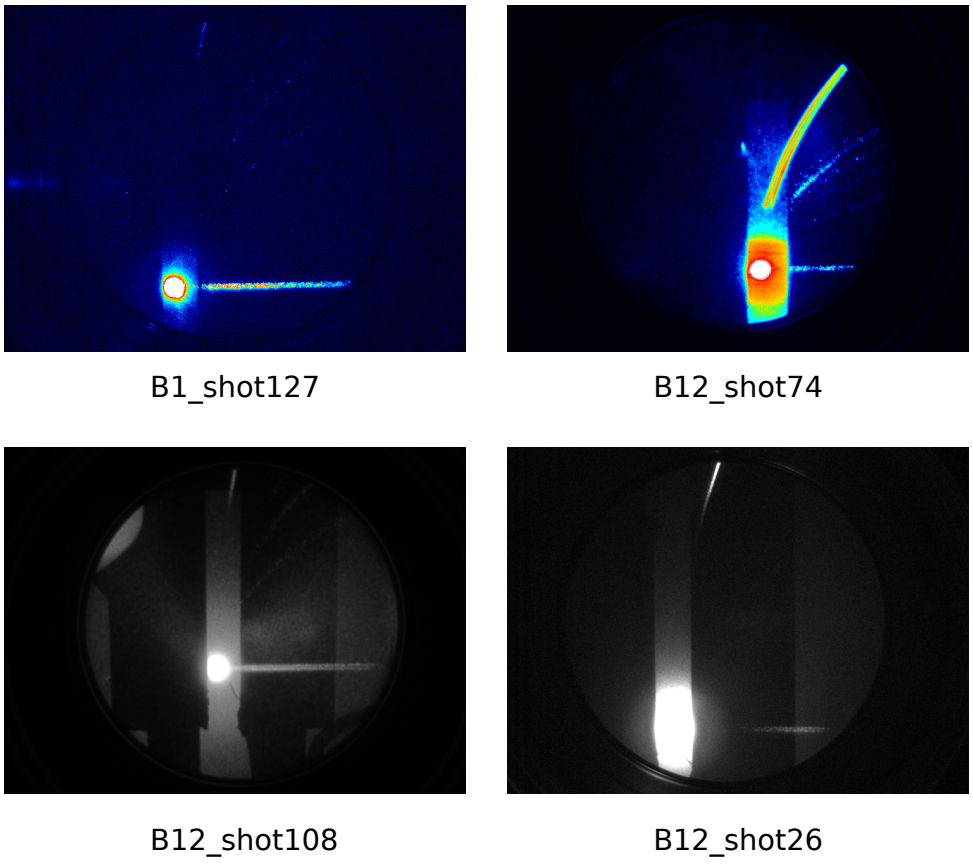

Figure 4.10.: Four different example TPS recordings with an additional horizontal signal. Shown in *top:* false colours *bottom:* grey values.

Potential Explanations

One possible explanation is that the horizontal traces come from an ion species that is deflected much more weakly by the magnetic field, i.e. has a lower charge to mass ratio. In the recordings, the C^+ track is the one where the deflection caused by the electric field is greatest compared to the magnetic deflection. Therefore, this track is a good choice for comparison. Since the target consists of titanium, a possible species would be Ti^+.

This means for an equal deflection in the E-field direction, i.e. $x_C = x_{Ti}$:

$$\frac{q_C}{m_C v_C^2} = \frac{q_{Ti}}{m_{Ti} v_{Ti}^2} \tag{4.4}$$

(see equation 3.1, without the variables that are kept constant). With $m_{Ti} \approx 4m_C$ and a single positive charge the equation becomes:

$$\frac{4}{v_C^2} = \frac{1}{v_{Ti}^2} \qquad \Rightarrow \qquad \frac{v_C}{v_{Ti}} = 2. \tag{4.5}$$

Now the ratio of the magnetic deflections of both species can be calculated:

$$\frac{q_{Ti}}{m_{Ti} v_{Ti}} \Big/ \frac{q_C}{m_C v_C}. \tag{4.6}$$

By insertion in equation 3.2 and the same assumptions one gets $\frac{1}{2}$ for the deflection of Ti^+ in comparison with C^+ due to the magnetic field by identical deflections due to the electric field. This deviation would be clearly detected and even a possible Pb^+ trace would have more than $\frac{1}{5}$ of the height of C^+ and would therefore also be clearly detectable.

Based on the traces that lie on a straight line, which is parallel to the electric field and originates at the pinhole, the particles should be positive ions that also have their point of origin at the laser/target interaction point. But since a deflection by the magnetic field would be detectable even for very massive nuclei, the particles would have to pass through the magnetic field as neutral atoms. A possible explanation would be that the particles are ionised and accelerated during the laser/target interaction, just like the other detectable particles, but these ions capture electrons in the gap between the interaction point and the magnetic field and thus become neutral atoms again. Therefore, these particles are not deflected by the magnetic field, but when they enter the range of the electric field, field ionisation occurs and the generated ions are deflected. At first glance, the electric field strength seems

to be several orders of magnitude too small for field ionisation (see chapter 2.1.3). However, if the atom is not in the ground state but in an excited state significantly smaller field strengths can also lead to an ionisation.

A highly excited atom is called a Rydberg atom [90], since a varied Rydberg formula can be used to calculate the energy levels. Actually, this formula only applies to hydrogen or hydrogen-like atoms, but since the highly excited electron is delocalised compared to the other electrons of the atom it can be approximated as one electron and a single positively charged nucleus and thus be considered similar to hydrogen. The threshold for classical field ionisation scales with the principal quantum number n^{-4} [91], so that atoms beginning with an $n \approx 15$ will be ionised with the electric field settings chosen for the TPS. Since the Rydberg atom lifetime may provide information about the possible origin, it is another important quantity. However, this variable also scales strongly with n (at least n^3), and can be hundreds of microseconds for strongly excited atoms ($n \approx 60$) [90]. This means that the runtime from the interaction point to the detector is still well below the possible lifetime even for the slow particles, i.e. those that hit the MCP at the edge. This means that no information about the point of origin can be obtained from this.

4.2.5. Spectral Shaping of a Proton Pulse

In the setup for irradiating cells, the ions are deflected by two opposing and movable permanent magnetic fields. This allows a very constant setting of the ion energy range, but it cannot be varied during the experiment. For cell experiments, however, it may be of interest to irradiate two otherwise identical samples with different proton energies and thus vary the position of the Bragg peak, for example. Since cell samples are time-sensitive, it is a great disadvantage for the comparability of the samples if the experimental chamber has to be opened and pumped down again for this purpose. In the following, a method is described for adjusting the spectrum during the experiment without having to break the vacuum or open the bunker. Due to the fast control technology, the technique shown theoretically offers irradiation possibilities that would not be feasible with deflection fields that are constant compared to the proton flight duration. First experimental data are shown to demonstrate the feasibility.

A proof of principle experiment has been set up in which an adjustable part of the proton spectrum is diverted. The basic design of the construction is shown schematically in figure 4.11. The setup is largely identical to the one used so far.

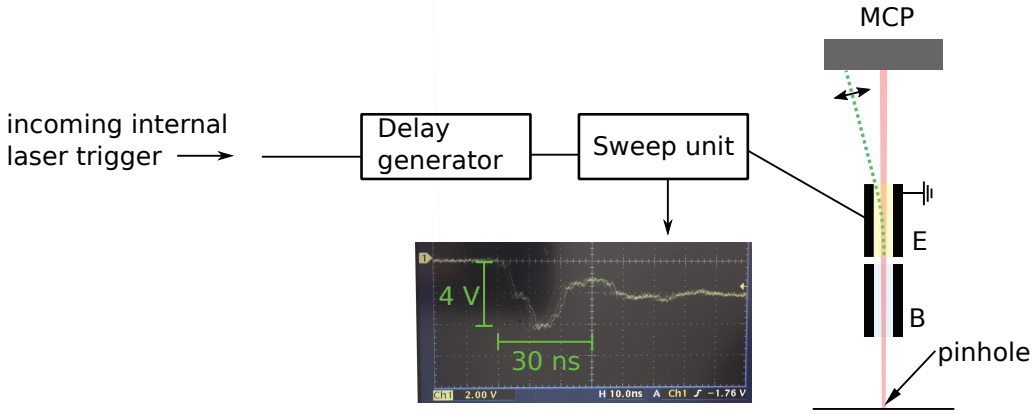

Figure 4.11.: Experimental setup for the streaking of a proton pulse. Only the modified section of the setup shown in figure 4.8 is illustrated here. The laser trigger signal is delayed for an arbitrarily adjustable time and controls the sweep unit. An attenuated (1:1000) streak pulse is shown as an example. The sweep unit is connected to one electric field plate and deflects a certain range of energy depending on the delay (indicated by the green dashed line).

The change is that the electric field of the TPS is switched on selectively and only the magnetic field remains constant in time. The magnetic field is only needed to determine the proton energy depending on the vertical impact position on the MCP. In a setup for cell experiments, a different configuration would be chosen. The working principle is to apply a high voltage pulse at the moment when the protons in the desired energy range are in between the plates to which the electric field is applied. For this, on the one hand, it must be quick to ramp up the electric field and, on the other hand, the process must be timed with the laser/target interaction.

The distance from the target to the entrance of the electric field was set to 135 cm. This means that a proton with the kinetic energy of 1 MeV needs 97 ns and one with 3 MeV 56 ns to reach the entrance of the electric field. To cross the 5 cm long field, they need 3.6 ns and 2.1 ns, respectively. The duration of the laser particle acceleration can thus clearly be neglected. Furthermore, the achievable energy resolution for the setup can be roughly estimated; a desired energy resolution of 100 keV would correspond to a runtime difference of about 1 ns for 3 MeV protons, but already 5 ns for 1 MeV protons. Thus, the achievable resolution is energy-dependent and it results in about 200 keV for the 3 MeV protons. If this were to be improved further,

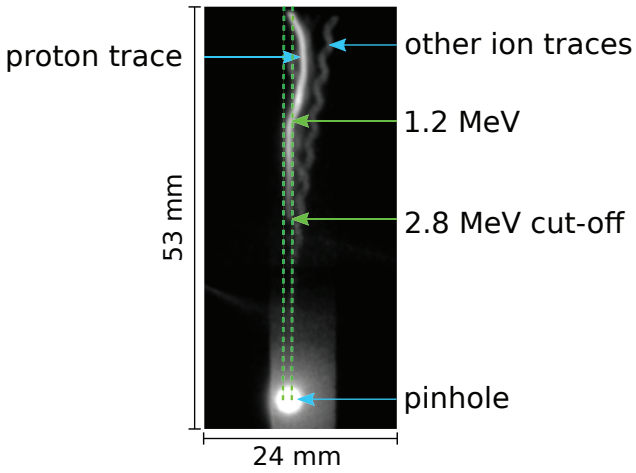

Figure 4.12.: MCP recordings a TPS setups with a pulsed electric field. The green dashed lines correspond to proton deflections only by a magnetic field in order to guide the eye. *left:* From the maximum proton energy of 2.8 MeV to 1.2 MeV, the straight track, deflected purely because of the magnetic field, can be seen. When the electric field is switched on ($E_{p^+} < 1.2\text{MeV}$), a clear deflection to the side can be seen. For the other ions, which pass later through the plates of the electric field, a curved line can be detected. By positioning a vertical slit, part of the proton spectrum could be cut out in this way.

the path length of the protons would have to be extended, which would have the disadvantage of reducing the dose. For the 1 MeV protons, on the other hand, a better resolution than 100 keV should be achievable.

For the timing of the electric field, the internal signal of the laser was used, which otherwise triggers the pump lasers, among others. This signal is coupled into a delay generator and passed on to the high-voltage generator. The minimal delay of this two devices was measured to be 61 ns. For this reason, the idea of using a photodiode as a trigger was rejected, as this would only have been possible for low proton energies.

An example recording with the pulsed TPS setup can be seen in figure 4.12. Without the electric field, the proton trace is only deflected vertically, depending on the energy, but as soon as an electric field is added, the track is additionally deflected laterally. On the image the defection starts at 1.2 MeV for protons and at the top the proton trace is nearly on the vertical line again, which means that these protons do not feel an electric field. The upper edge corresponds to a kinetic proton energy of 0.62 MeV. The difference in travel time for the different energies is about 36 ns. As no constant electric field is applied, the other ion traces cannot

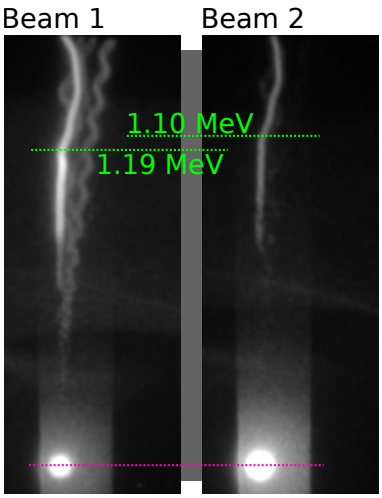

Figure 4.13.: Two MCP recordings with a pulsed electric field of two independent laser interactions. The left images shows ion traces from "Beam 1" and the right from "Beam 2". Due to different path distances, "Beam 2" interacts 4 ns earlier relative to the laser trigger. The pink dashed line indicates the same height of the zero points. As can seen the deflection due to the electric field starts at different energies (indicated by the green dashed lines).

be clearly assigned. However, they show a periodic oscillation and since, based on previous measurements, the traces probably come from carbon, the one marked with the arrow could belong to C^{3+} as the period is almost identical at 37 ns. The period duration was calculated by using the period length of the trace on the MCP. Since the magnetic field is constant, the kinetic energy of the C^{3+} ions is given due to the height of the impact position. Thus, the energy-dependent travel time differences from the target to the electric field can be used to calculate the period duration. The electric field for this ion trace seems to have a constant magnitude with a smaller periodically oscillating component. However, this can also be partly explained by the fact that the ions need a certain time to pass through the electric field (about 18 ns for C^{3+} at the upper end of the trace). Since this corresponds to about half the frequency, it cannot be approximated that these ions do not see an electric field.

Since protons are used for cell irradiation, the main focus was here and not on the other ion species. Two different measurement approaches show that the electric field can be set very precisely and that the jitter is negligibly small. One approach can be seen in figure 4.13. For this measurement, the two laser beams were synchronised and, in the next step, the travel distance of "Beam 2" was shortened by 1.2 m. As a result, "Beam 2" hits the target 4 ns earlier relative to the laser trigger. This delay

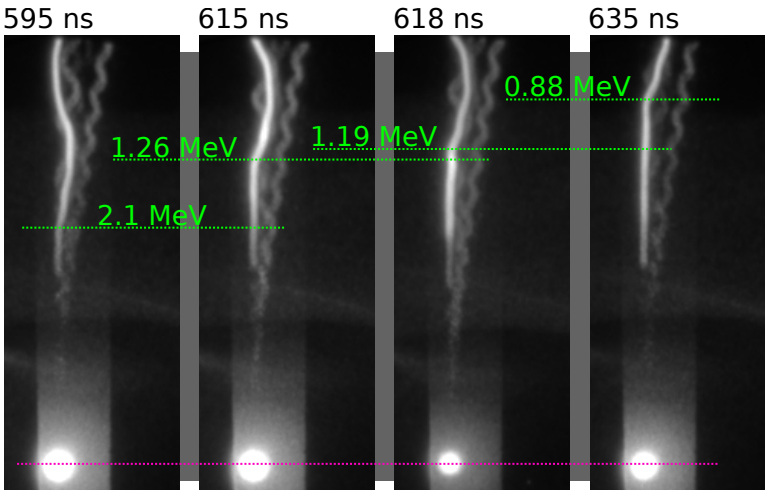

Figure 4.14.: Different delays of the pulsed electric field relative to the laser trigger. The pink dashed line indicates the same height of the zero points. The green dashed lines indicate the beginning of the deflection due to the electric field with the respective proton energies.

could be verified by measuring the kinetic proton energies at the beginning of the deflection due to the electric field. This energy was 1.19 MeV for "Beam 1" and 1.10 MeV for "Beam 2". By calculating the time of flight difference to the centre of the electric field plates, the adjusted 4 ns are obtained. The other approach can be seen in figure 4.14. The ion tracks shown were generated with "Beam 1" and the retardation was set on the delay generator. A delay of 3 ns is already clearly visible. Again, the calculated travel time differences matched the set ones to the nanosecond.

On the other hand, the reproducibility of the electric field level is also important. To test this, the MCP images were overlayed with the calculated proton traces for a constant electric field of 3.5 kV (see figure 4.15). The deflection due to the electric field depends on the kinetic energy of the protons and is significantly smaller for higher energies. It can be seen that the traces approach and fall off the parabola at different positions depending on the delay. This voltage also matches well with the measured voltage of the sweep unit (see figure 4.12). As expected, this deflection is also independent of the selected laser beam.

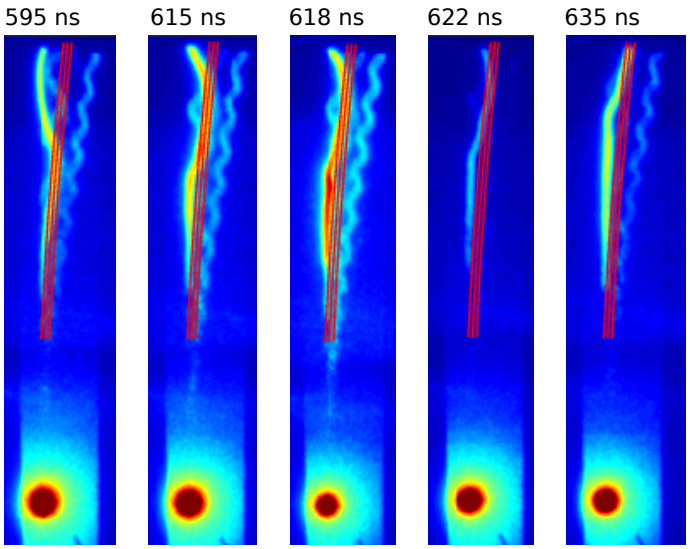

Figure 4.15.: Superposition of the MCP ion signal with a parabola (red lines) that would correspond to a proton energy in the range of 0.62 MeV to 5 MeV and a constant electric field of 3.5 kV/cm in the chosen setup (Matlab program form Aaron Alejo Alonso QUB). Apart from "622 ns", all tracks were generated with "Beam 1".

4.3. Conclusion and Outlook

Since the irradiation of biological samples with LAPs has been a very active field of research for some time and has currently gained momentum, especially in the context of FLASH-RT, it will probably further continue to be an active field of ongoing investigation [92]. In this regard, it is of course essential to be able to vary the parameters of the LAP irradiation. In this work, different approaches were investigated that have potential for possible application in cell irradiations.

Due to the ability of the Arcturus laser system to generate two largely identical laser pulses, it was an obvious choice to use both beams to work out the basics of varying the irradiation modalities. In a way, this establishes a link to one of the first experiments in the field of the FLASH effect, in which the effectiveness of two electron pulses is compared with that of a single pulse with the same total dose [47]. It could be shown that two TNSA events can be triggered in spatial proximity (1 mm) in the experimental setup. The closer the two interaction points are to each other, the more similar the proton spectra on the cell sample become. Since the two interactions can be freely arranged in time and space, temporarily overlapping cell irradiation with two different energy ranges, for example, could be realised. On the other hand, it would be possible to position the two interaction points vertically

(normal to the dispersion direction of the magnetic double yoke) in order to have two identical energy ranges arrive at the cell sample. For this, it would only have to be tested whether the mechanical stability of the titanium foil is sufficient, as anticipated.

The proof of principle experiment of a pulsed energy dependent defection protons has shown that this can be done with sufficient temporal accuracy when using the internal laser trigger. However, before the setup is implemented in the cell test chamber, further issues need to be clarified. For example the trade-offs of the installation: greater distance of the electric field plates from the laser/target interaction point allows for better energy resolution, but the dose is reduced and with a smaller distance of the plates from the sample, the total deflection is also reduced.

Since the beginning of the proton deflection due to the electric field could be determined relatively precisely, the time interval between the laser particle acceleration and the rise of the electric field was deduced from the proton energy at the edge. This showed that the jitter is small and the reproducibility is given. This already provides a good basis for a later implementation in the experimental setup.

5. Cell Irradiation Experiments

This chapter describes the performed cell irradiation experiments.[1] First, the basics are discussed, from the applied instruments to the used cells and their irradiation methods, then the experimental results are shown.

The ability of the platform to perform live cell experiments over several hours and to resolve fluorescently stained subcellular compartments with the attached fluorescence microscope, which can provide information about the radiation effects, is demonstrated. Furthermore, fluorescence experiments were evaluated with a flow cytometer due to better statistics and reproducibility. DSBs were investigated as the most relevant form of DNA damages induced by ionising radiation by detecting proteins on DSB sites on chromatin. Additional markers were also used to investigate other cell properties. For example, oxidative stress resulting from irradiation was investigated with various markers, as it is held responsible for a large proportion of cellular damage in radiotherapy. Here, first measurements showed lower oxidative stress for LAPs in contrast to X-ray irradiation. Last but not least, gene expression analyses of irradiated and non-irradiated haematopoietic stem cells were performed and the evaluation showed that different radiation damage response pathways were activated.

5.1. Instruments and Diagnostic for Medicine and Cell Biology

The following is a description of the pool of devices, methods and techniques used in this work, most of which are standard in medicine and cell biology. First, the most important equipment, the different types of mammalian cells used, will be discussed, as they provide the basis for the further investigations. This is followed by the sample preparation procedures including cell staining, the measurement methods and the

[1] A part of the results was already published in [10] and is presented in the following once more.

irradiation process.

5.1.1. Mammalian Cells

The tests were carried out on cell lines and on primary cells. The used cell lines had the advantages that they are more robust and had a better availability since they were cultured in our biological laboratory. The cells were cultivated at 37 °C, a high humidity and 5% CO_2 in medium. Different types of culture media were used depending on the cell type or experimental situation. To prevent bacteria infestation, we added penicillin and streptomycin in long-term culture. The disadvantage of the used cell lines is that they are established from cancer cells [93–96] and cultured for many years so they show significant differences to primary cells and provide only a limited information value for the human organism. The behaviour of primary cells has a higher information value for the human organism but these cells are more complicated to handle, due to apoptosis and differentiation. In addition, the cells came from different donors, which in turn has an influence on the cells. And also the amount of primary cells cannot be increased arbitrarily.

Another important classification of the cells for irradiation and evaluation is into suspension and adherent cultures. As the name implies, suspension cells are cells that grow free floating in the medium, whereas adherent cells must be connected to a surface in order to proliferate; these cells only detach from the surface briefly for the cell division itself. Whether a cell grows adherently or in suspension does not depend on the method of cell culture, only on the type of cell. Adherent cells have the possibility to migrate on the surface, but this movement is relatively slow, so that their position can usually be assumed to be constant for the duration of the irradiation and evaluation.

Cell Lines

Both, suspension (Jurkat, Ramos) and adherent (HeLa, A-549) cell lines were used for the experiments. Depending on the experimental conditions, a certain type of cell is more suitable. Generally speaking, microscopy is better with adherent cells and flow cytometry (FC) measurements with suspension cells.

Jurkat and Ramos cell lines were provided by the “Institut für Molekulare Medizin I - Prof. Dr. Sebastian Wesselborg” and cultured in our laboratory. The Jurkat

cells are T-lymphocytes. They were extracted from the blood of a patient with an acute lymphatic leukaemia [96]. Ramos cells were derived from the ascitic fluid of a patient with American-type Burkitt lymphoma [95]. The cells were cultured in medium that consisted of 89% RPMI, 10% fetal bovine serum and 1% penicillin and streptomycin.

HeLa cells originate from a cervical carcinoma. This cell line has been cultivated since 1951 and is the first human cell line. The cells were cultured in medium that consisted of 89% DMEM, 10% fetal bovine serum and 1% penicillin and streptomycin, but DMEM can also be replaced by RPMI [97].

A-549 cells originate from a lung tumour of a man [98]. The processing of these cells was carried out by the working group "Institut für Medizinische Strahlenbiologie - George E. Iliakis (45147 Essen)".

Primary Cells

The primary cells used all belong to the group of blood cells and thus to the suspension cells. For this group, the following distinction is made between the leukocytes extracted from blood samples and the stem cells obtained by apheresis.

Leucocytes or white blood cells had a much better accessibility because they were obtained from blood samples that were available in much greater volume and regularity. As far as possible, only samples from healthy donors were used for the experiments. To separate the leucocytes from the other blood components, a lysis buffer (in addition to water, 1 ml contains 8.29 mg ammonium chloride, 1.00 mg potassium bicarbonate and 0.0375 mg Na-EDTA) was used to lyse the red blood cells. After a few minutes, the sample was centrifuged, the supernatant discarded and the cell pellet, with the contained leucocytes, is resuspended in phosphate-buffered saline (PBS). The samples were then temporarily stored in the refrigerator. A further division of the cell types was only made after the trials/irradiations. Unless otherwise noted, the division was based on the side-scattered light (SSC) and the forward-scattered light (FSC) signal of the flow cytometer measurement (see figure 5.1).

Normal Hematopoietic CD34+ Progenitor and Stem Cells were obtained from the university hospital Düsseldorf - "Institute of Transplantation Diagnostics and Cell Therapeutics" from healthy donors. Remnants of the apheresis that were not needed for the stem cell donation were made available for research. These samples need to be further processed to obtain the high purity of CD34+ cells required for the experiments. First, a density gradient centrifugation was performed to isolate the peripheral blood mononuclear cells (PBMCs). For this purpose, the sample was placed in a test tube on a Ficoll® solution without mixing the two phases. The density of the Ficoll® solution is adjusted so that it is above that of PBMCs but below that of e.g. granulocytes. This means that after centrifugation, PBMC are deposited separately from other components on top of the Ficoll® solution and this layer of cells, which is usually clearly visible, can be aspirated. In a second step the purity of CD34+ cells was further increased either via fluorescence-activated cell sorting (FACS) or via magnetic-activated cell sorting (MACS). In both cases monoclonal antibodies were used which bind the protein CD34 on the cell surface, either conjugated with a fluorescence dye (FACS) or magnetic beads (MACS). The FACS technique is discussed in more detail in context with FC in chapter 5.1.4. The magnetic cell selection protocol was performed as indicated by *Miltenyi Biotec*. For this procedure, the prepared cell suspension is passed through a column, which is located in a magnetic field and is in turn filled with paramagnetic spheres. The cells to which magnetic beads have bound, because they express the specific surface protein, are now magnetically attached to the spheres, while cells without this surface protein can pass through the column undisturbed. In the next step, the column is removed from the external magnetic field, whereby the magnetic field of the paramagnetic spheres also disappears and the cells are thus no longer bound to them and can simply be washed out of the column. Furthermore, a distinction is made between positive and negative selection; in positive selection, the cells of interest are bound to a magnetic nanoparticle and in negative selection it is the other way round and, if possible, only the desired cells are not labelled by an antibody. No negative selection was performed as the effect of the beads on the cells is reported to be negligible.[2]

With the FACS technique a very high purity of stem cells could be obtained directly, but the process took a relatively long time, mainly due to the high cell

[2]https://www.miltenyibiotec.com/DE-en/products/macs-cell-separation/cell-separation-reagents/microbeads-and-isolation-kits/basic-principle-of-macs-microbead-technology.html

numbers required. Therefore, on the one hand, attention must be paid to the availability of the device and, on the other hand, the stem cells should be irradiated as quickly as possible, which was thereby naturally postponed. MACS, in contrast, could be performed relatively quickly and in case of an insufficient purity, the process could be repeated. This allowed a level in the range of 98 % of CD34+ cells to be obtained, so this process was generally used for purification.

5.1.2. Staining and Preparation of Cells

The cell preparation was very similar for the different analytical methods (fluorescence microscopy or flow cytometry), only the preparation for gene expression profiling was widely different, therefore this preparation is discussed separately in chapter 5.6. The specimens prepared for staining were either primary cell or cell line samples.

Our normal cell medium contained phenol red to detect changes in pH. For fluorescence measurements we used phenol red free medium or buffer because phenol red is known to cause a background fluorescence signal, so the cells were washed before the staining. Adherent cells were either washed with PBS or they were subcultured by trypsinization and incubated in phenol red free medium on coverslips. In the case of suspension cells, a subculture was pipetted from the cell culture into centrifuge tubes and centrifuged for 5 minutes at 350 g. Hereafter the supernatant was discarded and the cell pellet was resuspend with phenol red free medium or buffer.

For the staining we added the dye to the cell culture medium or buffer and mixed it by pipetting. For measurements with low dye concentrations or small volumes we solved the dye solution first in PBS (1:10 up to 1:100) and afterwards in the cell sample. This step was added to reduce the systematic error which is growing rapidly for small volumes < 1 µl [99, S. 31- 32].

All staining procedures were performed according to the protocols provided by the manufacturer. After the live cell staining the samples were incubated for usually 10 up to 60 minutes in the incubator. Most samples were prepared for live cell imaging the other samples were fixed with 1 % formaldehyde which was solved in PBS.

Since there was no CO_2 incubator for the cell port available, the pH stabilized *Leibovitz's L-15* medium was generally used during irradiation experiments and imaging of living cells.

Table 5.1.: Fluorescence dyes and antibodies

antibodies against	fluorescence dye	manufacturer
γH2A.X	Alexa Fluor 488	Cell Signaling Technology, Inc.
53BP1	DY550	LifeSpan BioSciences, Inc.
CD3	PerCP-Cy 5.5	BD Biosciences
DNA	Hoechst 33342	-
DNA	Propidium iodide	-
mitochondria	Mitotracker	Thermo Fisher Scientific Inc.
nitrotyrosin	Alexa Fluor 647	-
ROS	DCFH-DA	Merck KGaA
ROS	APF	Thermo Fisher Scientific Inc.
ROS	CellROX Green Reagent	Thermo Fisher Scientific Inc.

5.1.3. Fluorescent Dyes and Antibodies Used

To proof effects and also to distinguish between different cell types we used fluorescent labeled antibodies (see table 5.1). Which could be detected either with a fluorescence microscope or by a FC analysis.

To stain DNA in the cell nucleus during live cell experiments, we used *Hoechst 33342*, which penetrates the membrane of living cells and binds to the minor groove of the DNA[100] developing thus bright blue fluorescence (see figures 5.7 (left) and 5.8 (bottom)).

To detect dead cells, propidium iodide (PI) was used. When PI intercalates with DNA it shows increased fluorescence properties, but PI cannot penetrate through intact cell membranes. Therefore, after PI staining, only cells with a disturbed cell membrane integrity, which is an indication of apoptosis or necrosis, show a strong PI fluorescence signal.

The mitochondria were stained with Mitotracker™ from *Thermo Fisher Scientific Inc.*, which stains the mitochondria independently of the membrane potential, (figure 5.7 yellow).

Jurkat cells were stained with a CD3 antibody labelled with R-Phycoerythrin (PE) from *BD Biosciences* (figure 5.7 green).

DSBs were stained with an γH2A.X antibody from *Cell Signaling Technology*. In certain experiments, 53BP1 was additionally stained.

To detect ROS the fluorescent dyes APF and CellROX™ from *Thermo Fisher Scientific Inc.* were used, as well as DCFH-DA from *Merk KGaA*. The dyes were

either solved in dimethylsulfoxid (DMSO) (DCFH-DA, CellROX™ Green Reagent) or in dimethylformamid (DMF) (3‘(p-aminophenyl) fluorescein (APF)). Since the dyes were stored in the fridge or the freezer one had to make sure for in DMSO solved dyes that you were above the freezing point for staining.

5.1.4. Flow Cytometry

FC is used to measure properties of cells. From a suspension cell sample, a flow of single cells in a sheath of fluid is generated. This flow of isolated cells passes through a laser beam. Two different effects are exploited, on the one hand the scattering at the cells and on the other hand the fluorescence of stained cells. These devices are often referred to as FACS, regardless of whether or not subsequent cell sorting is performed. The FC data presented in this thesis were recorded with the FACSCANTO II™ or the LSRFortessa™, both from the company BD Biosciences - San Jose, USA.

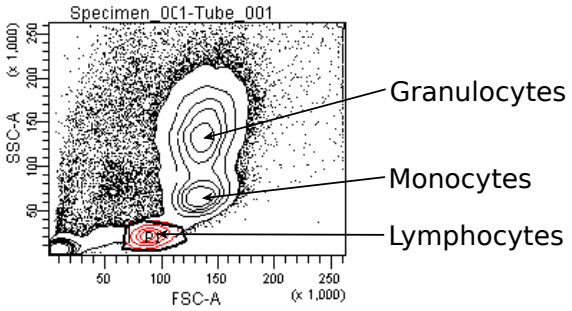

Figure 5.1.: FC measurement of a leucocyte sample. By measuring FSC against SSC, the separation of the individual cell populations can be clearly seen. An area can be marked for further analysis. Here, for example, the lymphocytes were selected (polygon with thick black line). This area “P1” is additionally coloured red.

Figure 5.1 shows an example FC-measurement of a leucocyte sample, where a splitting into different populations can be seen. For this, the scattering of the cells is firstly measured in the direction of the laser beam, the so-called FSC (horizontal axis), in order to make statements about the size of the cells. Secondly, the light scattered to the side (SSC) is also measured to determine the granularity of the cells (vertical axis). In the case of blood, for example, it is generally possible to identify the individual populations of lymphocytes, monocytes and granulocytes in this way, which are additionally separated from the debris, which is mainly located in the lower left corner .

Cell samples are usually stained with a fluorescent dye coupled to an antibody prior to the measurement. This allows even more information about the cell to be obtained from the fluorescence signal. The cell sample can be stained with several dyes simultaneously. By using lasers of different wavelengths and separating the fluorescence signals with filters, the emissions can be measured individually. For each cell or particle, the information on the SSC, FSC and the fluorescence channels used is thus stored. For further evaluation, the area in the FSC-SSC plot is usually delimited with cells that are to be evaluated further (in figure 5.1, this would be the area "P1" with the lymphocytes selected with a polygon). Only cells located in this window are used for a further evaluation based on the fluorescence signal. Of course, it is also possible to evaluate fluorescence against scatter channels, for example, the measurement of the SSC signal against the fluorescence-labelled CD45 antigen signal is also often used for a cell type division.

As already mentioned, with this technique it is also possible to sort the cells. For this purpose, individual droplets are created from the flow after it has passed through the laser light. These droplets ideally contain a cell about which the scattering and fluorescence properties are known. These droplets are now electrically charged depending on this information. When passing through an electric field, the trajectories of the droplets are now charge dependent and can thus be distributed to different culture dishes.

5.1.5. DNA Microarray

In this work DNA microarrays were used to quantify the transcriptome of CD34+ cells [101, 102]. This technique allows the simultaneous expression measurement of a large number of genes. On the surface of the micro array are fragments of single stranded DNA from the investigated genes. These DNA fragments can bind with complementary base sequences. This process is called hybridization. Since the transcriptome is made up of RNA molecules, they must be transcribed back into DNA in order to bind to the array. The detour via DNA is taken because DNA is much more stable than RNA. For the reverse transcription procedure the enzyme reverse transcriptase is used, which generates from the RNA templates the complementary DNA.

The generated and fluorescently labelled single-stranded DNA fragments from the cell sample to be analysed are now loaded onto the microarray surface. Based on the bound amount, the expression level can be determined in this way.

Figure 5.2 shows a DNA microarray after hybridization. On the left side one can see the complete array with several 100,000 test fields. Since the individual test fields cannot be distinguished here, a zoomed-in section is shown on the right-hand side in which the single test fields can be recognized. The differences in brightness of the fields can also be identified. The brighter fields have more fragments of labelled single-stranded DNA bound to them and thus correspond to stronger gene expression and the darker ones to weaker gene expression. In total, far more fields are evaluated than there are genes to be examined (number of genes examined on the chip used in this work is 21448). This redundant measurement is used to reduce the measurement errors and enhance the range.

5.2. Cell Irradiation

In this work, cell samples were irradiated with two different types of radiation. In addition to LAP irradiation, X-ray irradiation was also applied. The special features and limitations of the two methods are discussed below. Since irradiation with X-rays had fewer restrictions, these will first be briefly discussed. As the special sample preparation required for LAP irradiation has an influence on the cells, this preparation was also used for the X-ray samples for comparative tests.

5.2.1. Cell Preparation for X-ray Irradiation

For preliminary and comparative experiments, cell samples were irradiated with X-rays. For these experiments the X-ray machine *RS225 Gulmay GmbH - Krefeld,*

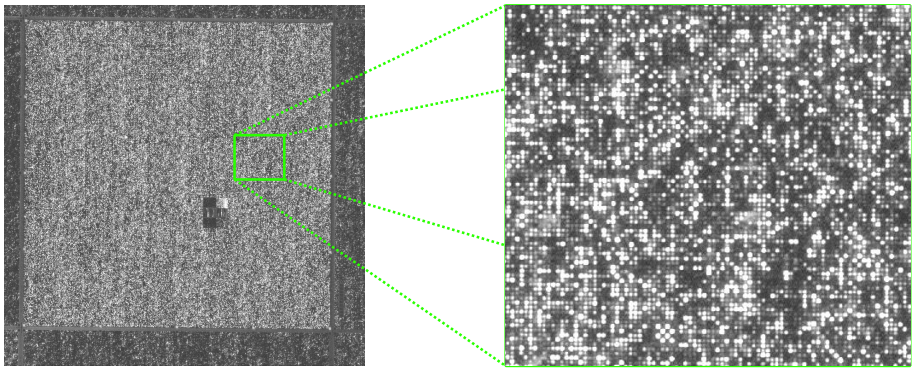

Figure 5.2.: DNA microarray after hybridization. The example shown is sample "1b" (see table 5.2). *left:* the complete array, *right:* zoomed in to see the individual test fields.

Germany from the "Labor für Molekulare Radioonkologie", supervised by Dennis Sohn could be used very flexibly. The dose rate of the X-ray tube in the irradiator is calibrated for two voltages: 150 kV corresponds to 0.72 Gy/min ($\hat{=}$ 12 mGy/s) and 175 kV corresponds to 1.01 Gy/min ($\hat{=}$ 16.8 mGy/s) at a table spacing of 461 mm, 0.2 mm Cu filter and a current of 15 mA. The higher dose rate is usually used for doses larger than 10 Gy to reduce the irradiation time. The temperature of the irradiation chamber can be adjusted, but not the humidity or the CO_2 level, therefore the irradiation time can be important, depending on the sample used. During irradiation, the cells were usually in multiwell culture plates or in LAP-sample holders.

5.2.2. Cell Preparation for LAP Irradiation

In contrast to the cell irradiation experiments described in publication [9], which were also carried out by our research group, we focused here mainly on suspension cells and to a lesser extent on adherent cells. The challenge of radiating suspension cells with our setup is that we can only radiate a small cylindrical volume (radius about 6.5 mm and height < 100 µm), but for example gene expression profiling and FACS analyses need a high cell count. The size of the base is restricted by the vertical distance of the deflecting magnets and also by the energy distribution due to the deflection of the magnets. The height is restricted because of the range of the low energy protons. Here we had to make a compromise. On the one hand the penetration depth of the protons should not be too short but on the other the flux of protons must not be too small. Another very important and obvious point which needs to be considered is the effect this whole procedure has on the cells even without radiation.

For suspension cells we were not able to get the required cell number by culturing the cells until the desired confluence level of the surface was reached. So three different methods to achieve a high cell density and acceptable unintended side-effects were tested. The individual methods are described below, and since they offer differing advantages, the appropriate method was selected depending on the experiment.

Centrifuge Cells: High Cell Density

To obtain a high cell density the suspension cells were centrifuged for 5 minutes at 350 gravitational acceleration 9.8 m/s^2 (g). Afterwards the cell pellet was resuspended in medium 1:1 which leads to a cell density in between 200,000 and 300,000 cells per µl. These high cell densities could usually only be achieved with a very high input cell count and were about one order of magnitude lower with the CD34+ cells. For the irradiation 1.5 µl of this high concentrated cell suspension were pipetted on the middle of the Mylar® foil and a coverslip was put on the other side of the cell suspension. This produced a very thin cell layer between the Mylar® foil and the coverslip of approximately 11 µm.

Cytospin

With a cytospin or cytocentrifuge it is possible to concentrate a high number of suspension cells in a thin layer on a coverslip. Generally, cytospins are used to centrifuge cells onto a slide and to prepare them for microscopy. The disadvantages of this technique for our needs are that the area, which is covered with cells, is small compared to the size of the irradiated area and the recovery of cells from the coverslip is quite low. The reasons for the low recovery rate could be that the cells dry out while they are spined on the coverslip or that the cell membrane is destroyed by detaching the cells from the coverslip.

RetroNectin®

Originally, RetroNectin® (*Takara Bio inc.*) is used to enhances retroviral-mediated gene transduction, this means that a gene or DNA segment is incorporated into the host cell genome via a virus. For this purpose, the surface of the cell culture dish is coated with RetroNectin® and both, the host cell and the virus bind to RetroNectin® and, due to the proximity, the probability of DNA transfers increases. Prof. Cornelia Monzel suggested using a RetroNectin® coating so that the haematopoietic cells bind to the respective surface and omitting the virus. With this method a weak cell binding to the surface was achieved, which required careful pipetting.

The sample preparation was as follows: the coverslips were laid in a RetroNectin® solution or the solution was given into the LAP sample holders and put in the refrigerator ($\approx 8\ ^\circ C$) overnight (or longer). The solution was subsequently pipetted off again. The RetroNectin® solution was used up to three times. The remaining

solution was carefully washed off with PBS. Afterwards they were placed in a petri dish and 200 - 300 µl of cell suspension was pipetted onto the coverslip or LAP sample holder. These prepared samples were placed in the incubator afterwards for a few hours or over night.

5.3. Measurement of Double Strand Breaks

The next step, of course, is to prove that there is a direct effect of LAPs on the irradiated cells. Since DSBs have a large share in the adverse effects of particle radiation on cells, their detection was used as a positive control. To measure the DSBs after irradiation via the formation of γH2A.X, cells were washed with buffer, fixed in formaldehyde, permeabilized using Triton-X100, stained and then washed. Fluorescence intensity was measured by FC in case of suspension cells.

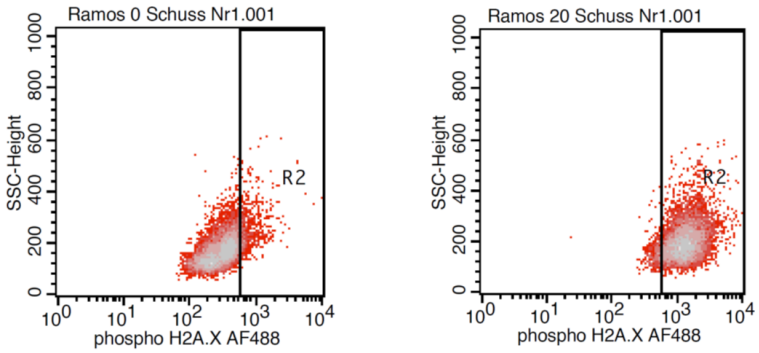

Figure 5.3.: FC analysis of Ramos cells, each about 10 000 events in the cell gate. On the vertical axis is the intensity of the side scattering. On the horizontal axis is cell fluorescence intensity of the γH2A.X conjugated fluorescent molecule. *left:* unirradiated cells; *right:* the cells were irradiated 20 times (about 1 Gy)

The diagrams in figure 5.3 show the flow cytometry analysis of Ramos cells. On the left the cells were not irradiated. On the right the cells were irradiated 20 times (about 1 Gy). It can be seen that the whole cell population shows higher fluorescence after the irradiation. Since the fluorescence dye binds specific to γH2A.X, which is a marker for DSBs, the protons caused DNA damage.

For diagram 5.4 this was repeated several times and the mean fluorescence intensity was plotted. This series of measurements was performed before the laser upgrade, which is why the dose per shot is significantly lower. Furthermore, an older tape target was used, which did not run as stable, so that fluctuations were

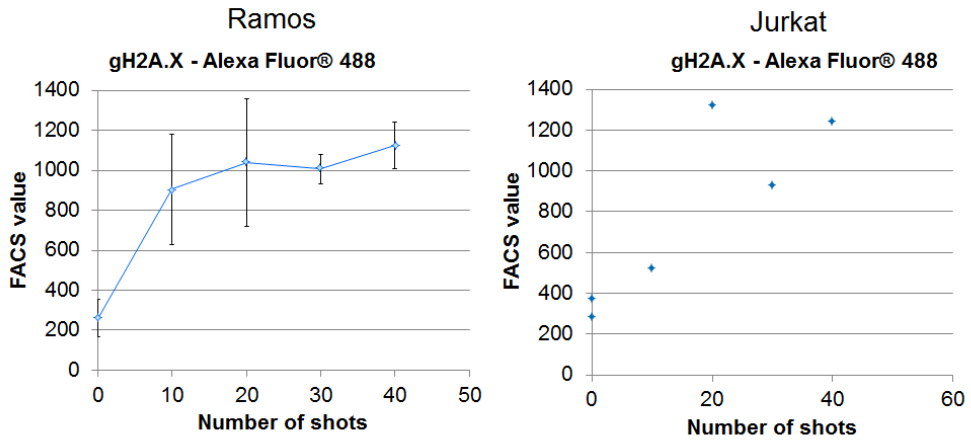

Figure 5.4.: Evaluation of several flow cytometry measurements. *vertical axis:* mean cell fluorescence intensity of the γH2A.X conjugated fluorescent molecule *horizontal axis:* Number of shots *left:* averaged over at least three Ramos cell samples.
right: Jurkat cell samples

also significantly higher.

After the laser upgrade, DSB experiments were also performed. Here we were able to show that, as expected, the fluorescence signal increases with the dose for both repeated FC measurements (see figure 5.5) and by scoring foci (only for adherent cells; see figure 5.6 left). For adherent cells, 53BP1 was additionally stained and foci were counted using a confocal microscope. The foci scoring followed in [9] published methodology. In this experiment the dose per shot was more than 10 times higher, due to the laser upgrade, but the number of foci per Gy is in good agreement among the trials. As in the previous experiments, in addition to γH2A.X staining, 53BP1 was also detected and the corresponding foci scored. The agreement between the results generated by scoring the two types of foci was very high. The FC measurements of γH2A.X show similar trends. Since there is no signal saturation in the dose range considered, the DSB-signal may also be used as confirmation of the delivered LAP dose. This is particularly useful for suspension cells, as a subpopulation can be extracted for this purpose after irradiation. Because the cells are fixed before the above staining procedures, the DSB measurement is not time-sensitive. Future studies may also include live cell imaging before cell fixation, particularly since the number of foci decrease from 22 only to 19 within the first three hours (see figure 5.6 right). Fixation could be easily integrated into the experimental procedure. For experiments with live adherent cells, which are carried out within

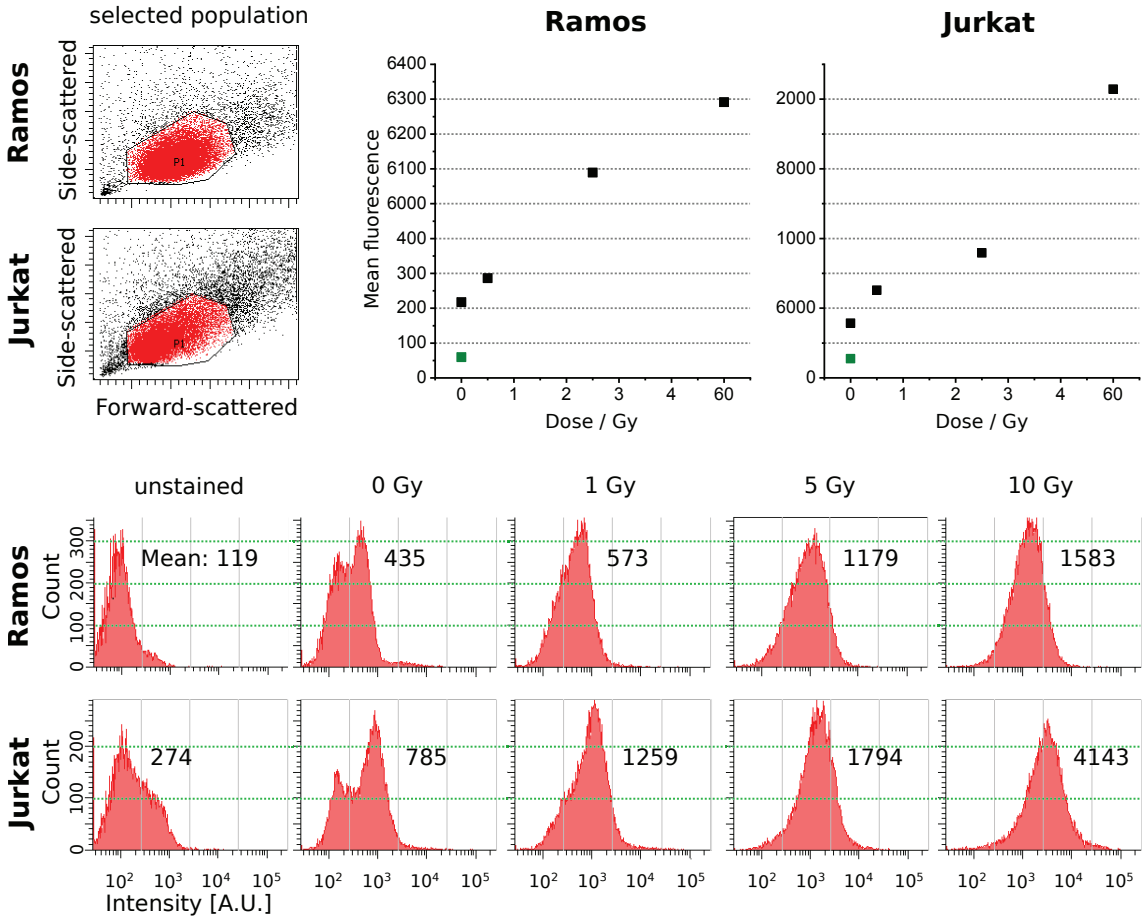

Figure 5.5.: FC measurements of the γH2A.X fluorescence intensity after irradiation of Jurkat and Ramos cells with LAPs. Cells were stained with a γH2A.X antibody. *top left:* for the Ramos samples, the cell population in the scatter plot is easily distinguished from unwanted cell fragments. The same gates were chosen for the Jurkat samples. *top right:* Only the selected population (red) is taken into account in the diagrams shown. Each point indicates the mean fluorescence intensity of the respective cell sample. The individual green markings show the fluorescence signal of the corresponding unstained sample. *bottom:* The respective histogram is shown for each diagram point. The number of total events detected is 20,000. (edited from [10])

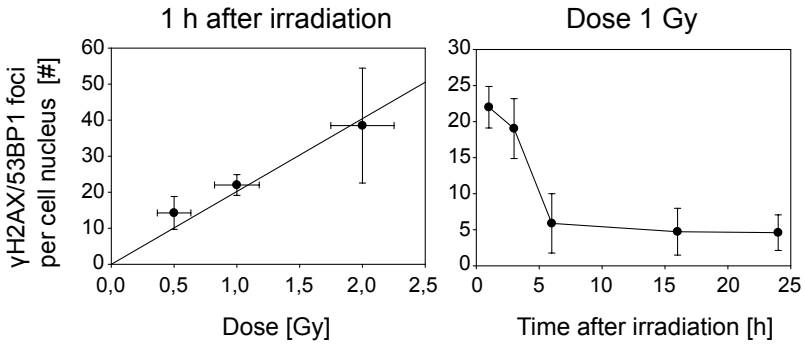

Figure 5.6.: LAP irradiated A-549 cells. Each condition was tested three times and 50 to 100 cells were scored for γH2A.X foci at the indicated times after irradiation. The foci were counted using a confocal microscope. The standard deviation is plotted as an error bar for each dose or time point. *left:* Number of foci as a function of radiation dose measured 1 h after irradiation. *right:* Number of γH2A.X foci as a function of time after 1 Gy irradiation. The reduction reflects repair of DSBs. (from [10], evaluated by Michael Piel)

the first three hours after irradiation, it should be possible to fix the complete cell sample and then stain for DSB foci with another fluorescent dye.

The DSB-signal should be suitable for dosimetric purposes, as initial experiments indicate that the number of DSBs is independent of the proton source [92]. Before an exact dosimetry with the DSB-signal can be carried out, comparative experiments with conventionally accelerated protons should be performed. Furthermore, a dependence of the signal intensity on the cell line used is indicated by the results shown. As can be seen in the figure 5.5, the fluorescence intensity is consistently higher in Jurkat cells as compared to Ramos cells. Therefore, a separate calibration curve must be generated for each cell line.

5.4. Live Cell Imaging while Irradiation

For the live imaging of the cells during the LAP irradiation, an the epifluorescence microscope attached to the chamber was employed (technically described in chapter 3.4), the data obtained are presented below. It is shown that the live visualisation of cell parts and properties is possible during the irradiation and that the cells are still in a healthy condition while undergoing this process.

5.4.1. Live Cell Experiments and Verification of Cell Integrity

First of all, to demonstrate that cells behave normally while located in the irradiation apparatus and that their viability is not appreciably affected, we recorded the condition of HeLa cells for up to 3.5 hours after placing them in the apparatus. Single cell layers could be easily monitored under the standardized conditions developed. Figure 3.13 (right panel) shows three representative time points of a 3 h time-lapse recording. Beside cell movement we could also detect cell division (marked with white arrows) and the reattachment of the divided cells to the surface (the complete video can be found in V. Supplementary material of publication [10]). It can be concluded that the cells are definitely alive during the recording and the conditions in the sample holder are therefore sufficient for cell lines.

Furthermore, PI was used in FC live cell measurements to detect dead cells. The proportion of PI positive cells was usually in the low single-digit percentage range. There were strong differences between the media or buffers used. Here, the *Leibovitz's L-15* medium showed the best characteristics in preliminary tests, which was one reason why it was used in most experiments.

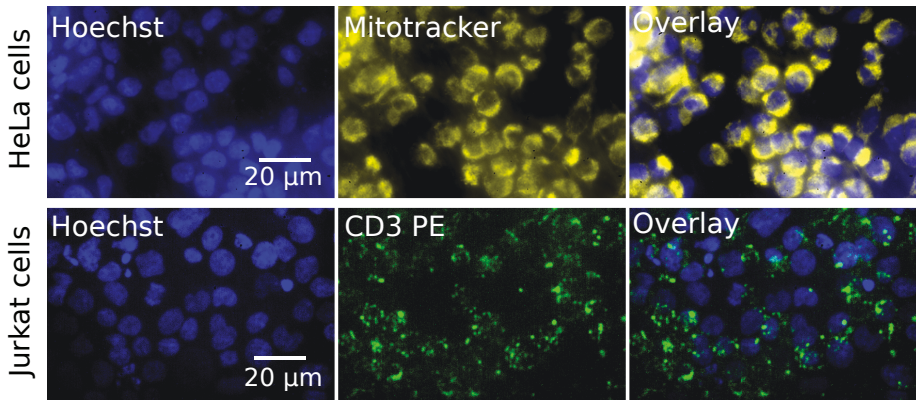

Figure 5.7.: Live imaging of HeLa and Jurkat cells before proton irradiation. *left:* Hoechst staining of cell nuclei. *middle:* Fluorescence images of the mitochondria, Mitrotracker (top), and the antibody, CD3 (bottom). *right:* Overlay. (from [10])

Live Cell Imaging of Fluorescence Stained Cells

Images of the nucleus of HeLa and Jurkat cells are shown in figures 5.7 and 5.8 (bottom). As can be seen in figure 5.8 (bottom), the fluorescence signal is 90 min after the irradiation sufficient to record a clear image of the cell nucleus. Additionally

we took images of the mitochondria, which can be seen in figure 5.7 (yellow) and stained Jurkat cells with a CD3 antibody, which can be seen in figure 5.7 (green).

5.5. ROS Detection

As ROS play an important role in the biological damage induced by ionising radiation, their detection is of great interest. Differences in the ROS production due to varying radiation characteristics could well offer advantages in radiotherapy. This is especially interesting in the context of the currently widely discussed FLASH effect (see chapter 2.2.4), where healthy tissue is spared at high dose rates but the tumour control remains the same. For this sparing effect most explanations are related to ROS. To be able to detect ROS directly after the irradiation, while the cells are still placed in the port of the chamber, a fluorescence dye was required that changes its fluorescent properties when it gets in contact or reacts with ROS, to quantify ROS by this method. Three different substances that meet this condition were tested here: APF, CellROX^{TM} and DCFH-DA. In the first trials with X-rays, DCFH-DA and CellROX^{TM} produced the more promising results. DCFH-DA delivered the higher yields as a consequence of the irradiation and CellROX^{TM} has the advantage that it is much less sensitive to light. Therefore, the experiments presented here focused on these two markers.

Figure 5.8 (top) shows a sample of HeLa cells stained with CellROX^{TM}. The first image shows the cells directly before the irradiation and the two images next to it, at 4 and 8 minutes after the irradiation, respectively. In all three images, the fluorescence signal is clearly distinguishable from the background. The cytoplasm shows a significantly higher fluorescence intensity compared to the nucleus. In the cytoplasm, there is no homogeneous distribution but presumably a binding of the dye to cell structures. Since the here shown images are a selection of a continuous exposure, the fluorescence signal decreases significantly due to photobleaching during the measurement. Therefore, the contrast of the images was increased from left to right. Unfortunately, microscopy showed no significant differences in the evolution of the fluorescence signal between irradiated and non-irradiated samples.

The difficulty of detecting ROS is that the fluorescence properties of the available markers are strongly influenced by other parameters and not only by ionising radiation like LAPs. In publication [103] significant changes in the fluorescence signal level of DCFH-DA between cells, which were covered with Krebs Ringer Phosphate

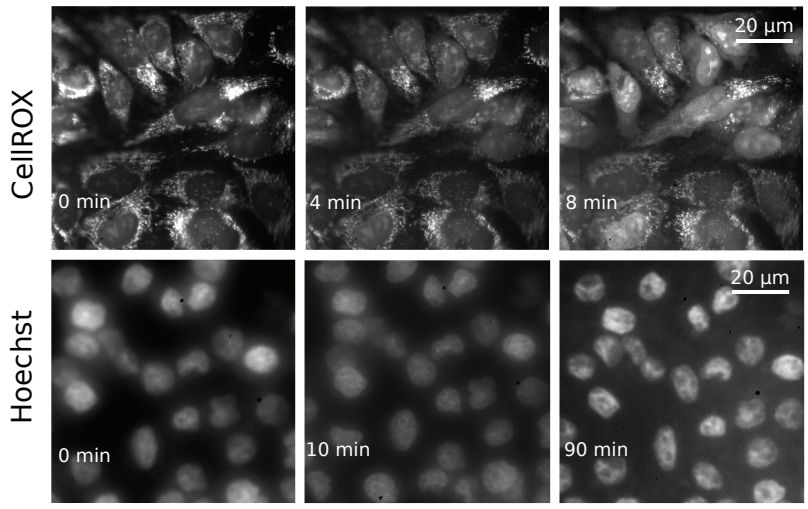

Figure 5.8.: Snapshots of the live imaging of proton irradiated HeLa cells at different time points. 0 min: directly before irradiation; *top:* CellROX^{TM} fluorophore. Cells were irradiated with 10 Gy (LAP); *bottom:* Hoechst 33342 staining of HeLa cell nuclei. Cells were irradiated with 2 Gy (LAP) (from [10]).

Buffer compared to cells, which were covered with medium or a different buffer, were detected. Another effect that has a strong influence on the measurement of ROS, is the oxidation of DCFH-DA due to the excitation light. For CellROX^{TM}, this effect was much smaller on the sample. In particular, if the level of ROS is measured with a fluorescence microscope one has to pay attention to increase of the signal level due to the excitation light. This is one reason why preliminary experiments were carried out with a flow cytometer. In FC the excitation laser beam exposes the cell only for a very short time so this effect can be neglected or the effect is at least equal for all the cell. As mentioned above, no significant fluorescence change could be detected microscopically between irradiated and untreated samples, so the focus has been placed on FC measurements.

5.5.1. Flow Cytometry Measurements

Both, suspension cell lines and primary blood cells were used for ROS measurements by FC. In addition to the irradiation with LAPs, cell samples were irradiated with X-ray radiation for the comparative experiments with the X-ray machine described in chapter 5.2.1. The dose of X-ray radiation was varied in a range from 0 to 10 Gy. The culture medium *Leibovitz's L-15* was used in all the experiments analysed here. For the detection of ROS, the two dyes DCFH-DA and CellROX^{TM} were used, as

they showed the strongest response in the preliminary experiments.

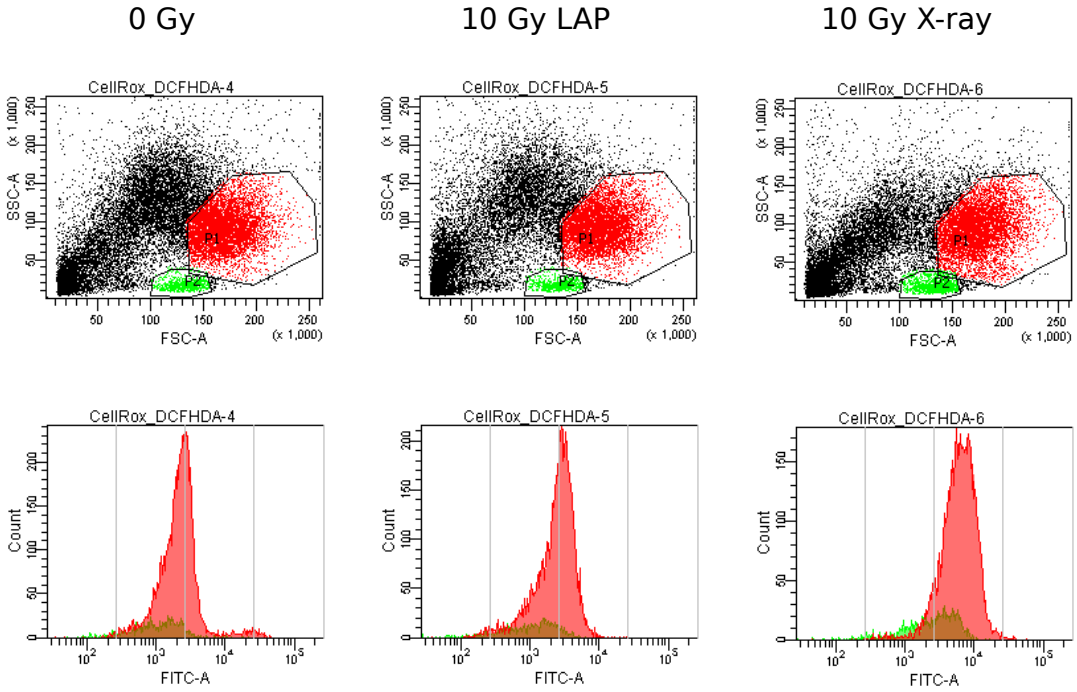

Figure 5.9.: FC measurements of the DCFH-DA fluorescence intensity of a processed blood sample. The left image shows the unirradiated sample, the middle one shows a sample irradiated with 10 Gy LAP and the right one a sample irradiated with 10 Gy X-ray, below are the corresponding histograms. For the evaluation the interval "P1" (red) was used. Additionally, in green, "P2" is also shown in the histograms.

Figure 5.9 shows FC measurement of primary white blood cells. These example images show cell samples that were first stained and then divided among the different samples, irradiated and measured by FC. In the measurement results shown in the following, the staining was always performed before irradiation. In the figure shown, granulocytes (P1, red) and lymphocytes (P2, green) are selected, but the focus of the measurements was mainly on granulocytes since they contain a large number of cells and therefore provide better statistics. However, as can be seen in the associated histograms, the fluorescence trend is analogous for both cell types. The granulocytes cannot be separated clearly from the monocytes in this FSC/SSC measurement, so some of these cells are presumably also in the selected interval. It should be ensured that the amount of debris is low in the selected interval. Therefore, the measuring ranges are shifted somewhat to higher FSC values.

The following variables were considered for the measurements: the type of ra-

diation, LAP or X-ray, and the respective doses. The dye selected, DCFH-DA or CellROX^{TM} and whether primary cells or cell cultures were involved. Furthermore, for the X-ray irradiated cells, a distinction was made whether the cells were in the LAP sample holder or in a cell culture vessel during irradiation. Test samples, which were in parallel irradiated with LAP and X-ray irradiation were also registered separately. This was done to exclude systematic errors in the staining, the sample or the test day.

5.5.2. Flow Cytometry Results

For the evaluation of the FC measurements, the fluorescence intensity mean value of the granulocyte area was used. The evaluation of the obtained data can be seen in the figures 5.10 and 5.11. Due to experimental circumstances, it was not possible to set the average intensities of the zero samples to a relatively equal value. Therefore, all irradiated samples were normalised to the respective unirradiated samples.

In the first figure the normalised intensities are presented as a function of the dose for four different cases. On the left hand side the DCFH-DA and on the right side the CellROX^{TM} samples are shown, while the samples in the top are irradiated with X-rays and the bottom ones with LAPs. The individual data points are colour coded. For the X-ray experiments the red circles are from cell lines irradiated in cell culture vessels and the pink ones from primary cells. The black and blue data points are also from primary cells but irradiated in a LAP sample holder. The blue points represent cell samples that were subdivided for a parallel X-ray and LAP irradiation. For the LAP case its analogous. The only difference is that the cell lines were also mandatorily irradiated in LAP sample holders.

A dose-dependent increase in fluorescence intensity can be seen for the samples irradiated with X-rays. This increase is stronger for DCFH-DA than for CellROX^{TM} (different y-axis scaling). In both cases, a relatively strong scattering of the fluorescence intensities occurs, which is stronger for the samples in the sample holder than for those irradiated in the cell culture tube. For the samples irradiated with LAPs, no increase in fluorescence intensity associated with the dose can be found, this is also true for samples irradiated with doses of 20 Gy and more.

Since the sample holder had an effect on the measurement, only the evaluations of samples irradiated in a LAP sample holder are shown in Figure 5.11. Here it can be seen that the fluorescence intensity for CellROX^{TM} samples no longer increases so clearly with the dose. For DCFH-DA stained samples, however, there is still a

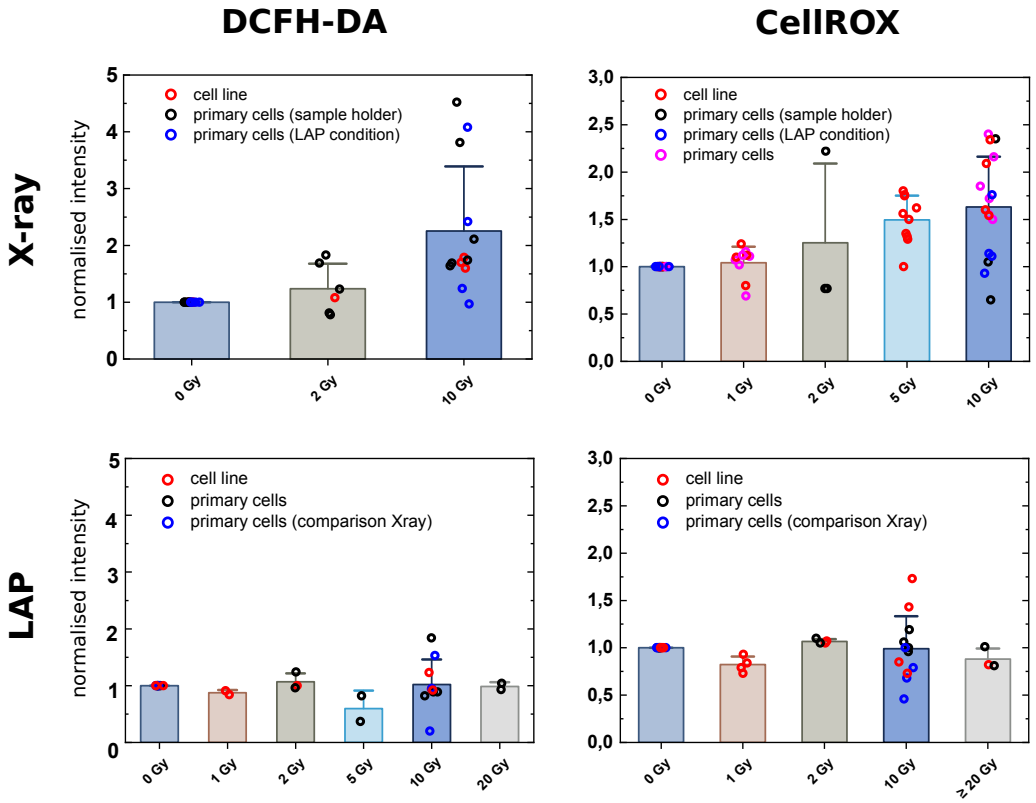

Figure 5.10.: FC measurements of the fluorescence intensity after the irradiation of cell samples with X-rays or LAPs. The cells were either stained with DCFH-DA or CellROX^{TM}. The bar height corresponds to the mean value of the intensities relative to the respective 0 Gy sample. The standard deviation is plotted as an error bar in each case.

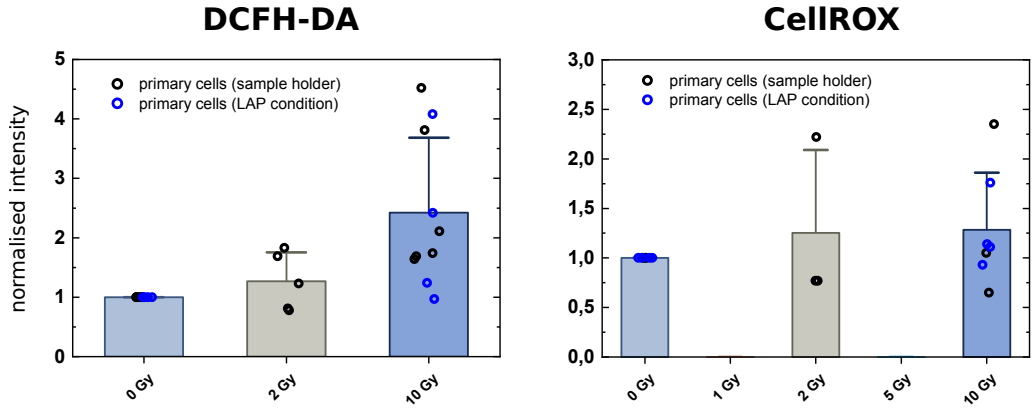

Figure 5.11.: Analogous evaluation to figure 5.10 (top X-ray), but limited to samples irradiated in an LAP sample holder.

strong dose-dependent increase.

5.5.3. Discussion and Outlook

In the following, firstly possible causes for the different increase in fluorescence intensity of ROS-markers in LAP and X-ray irradiated samples are discussed, then causes of the statistical errors are presented. Which systematic improvements would be desirable and how they are or could be implemented is described at the end of this section in chapter 5.7, as this part overlaps for the different cell experiments.

Oxygen depletion, which is responsible or partly responsible for the FLASH effect (see chapter 2.2.4), is a possible reason for the increase in fluorescence intensity in X-ray irradiated samples, which is not observed in LAP-irradiated samples. Molecular oxygen, which is present in the cell, is consumed by the ionising radiation directly or by reactions induced by it. At low dose rates, this oxygen loss is compensated for externally by diffusion, but at high dose rates there is a sudden loss that cannot be compensated for so quickly. This temporary hypoxia protects the cells because less ROS, which damages the cells, can be formed and thus less ROS is detected with the markers.

For the generation of the FLASH effect, the dose rate is decisive, the empirically found value of 30 Gy/s roughly sets the lower limit. In this work the reference samples are irradiated with X-rays with either 12 mGy/s or 16.8 mGy/s, i.e. with a dose rate that is more than three orders of magnitude lower than necessary to induce the FLASH effect. For the higher of the two dose rates, this corresponds to about 10 min for an irradiation with a total dose of 10 Gy. For the LAP irradiated samples with a dose of 0.5 Gy per shot and a shot frequency of 1 Hz, the total dose rate is ≈ 0.5 Gy/s for 10 Gy, which are accordingly reached in 19 s. This dose rate is significantly higher than that of the X-ray comparison measurements, but it is also well below that of the FLASH dose rates. In most publications, a dose rate dependent effect was observable starting at a total dose of about 10 Gy, but this may also well be due to the more challenging detectability at small doses than to the non-existence of an effect (cf. cell survival curves in publication [54] Figure 1). What might be more relevant, however, is the extremely high dose rate per shot [51], which is about 10^8 Gy/s for the LAP irradiation, far exceeding most dose rates previously published in connection with the FLASH effect [50, 51]. Furthermore, 0.5 Gy per shot is already such a high dose that the average distance between two proton tracks is in the range of 1 to 2 µm (cf. figure 3.4 left), and thus, temporally

anyway, but also spatially, interactions between the radiation products can occur (cf. figure 2.8).

Besides oxygen depletion, other effects, which occur at high dose rates, might be crucial, such as radical-radical reactions, whose rate increases with the square of radical concentration [104]. This would also result in fewer ROS interacting with the fluorescence markers and thus also contribute to a lower fluorescence signal. Another parameter that must be considered in this context is the LET. The higher the LET, the closer the radiation induced radicals are to each other. With the proton energies used here, the LET is about one order of magnitude higher than for proton energies generally used in radiation therapy, both for the plateau phase and the Bragg peak (SRIM comparison of 2 MeV to 100 MeV protons). Even if the LET is still well below the threshold at which oxygen deficiency no longer has a cell-protective effect, there will be different distributions of compounds synthesised in samples exposed to X-rays and those exposed to LAPs [105]. For this reason it would be beneficial to perform comparison proton irradiations with low dose rates but a comparable LET. The realisation of such a setup is discussed later (chapter 5.7).

As demonstrated in publication [54], the possibility of triggering the FLASH effect or rather cell protection through temporary hypoxia is related to the initial oxygen saturation. Under atmospheric conditions, the oxygen concentration is too high to induce temporary depletion and this is also the presumed reason why no FLASH effect could be detected in many *in vitro* studies [51]. In the case of the samples used here it is very likely that the oxygen content in the cells was greatly reduced. As the cells were trapped at high concentrations in a very small volume between the coverslip and the Mylar® foil, oxygen exchange was severely restricted. Due to the manual sample preparation, not all samples will have had the same oxygen content during irradiation. A too low oxygen concentration and a resulting lower ROS generation in some of the X-ray samples could have led to the fact that the fluorescence did not increase for these samples, but increased very significantly for others. Another factor to consider, especially with DCFH-DA, is the light sensitivity of the markers. Thus, some of the statistical variation will be due to differences in light exposure between samples. This could probably be reduced by designing a largely opaque sample holder.

5.6. Gene Expression Profiling

Hematopoietic CD34+ progenitor and stem cells were irradiated for gene expression profiling in two different campaigns. The first campaign was before the last laser upgrade in which the laser pulse energy was increased by adding two new pump lasers [3]. Due to this upgrade the proton flux per shot was higher in the second campaign. Also the cell preparation was different in the second campaign to reduce the stress for the cells.

In both campaigns, the RNA was isolated the same way (see 5.6.1). Since the amount and density of RNA in the samples was in most cases to small for the Implen NanoPhotometer N60, the RNA density and RNA integrity number was measured by the "Biologisch-Medizinisches Forschungszentrum (BMFZ)" of the Heinrich-Heine-Universität. For the micro arrays (see and 5.6.1) only samples with a high enough RNA density for the chips and a RNA integrity number (RIN) of 9 or higher were used.

5.6.1. General Procedure

The procedure consisted of several steps, which are described below in chronological order. First, usable cells must be available in sufficient numbers. For this we received left overs from the "Institute for Transplantation Diagnostics and Cell Therapeutics" from the apheresis of healthy donors. These specimens are, for example, samples previously used for quality control and are not needed for stem cell transplantation. The cell suspension, which is obtained during apheresis, has to be purified subsequently to increase the proportion of CD34+ cells.

Purification, Irradiation and Incubation

Two methods were tested for purification, one via FACS and the other via MACS. As mentioned in Chapter 5.1.1, the MACS method has become established, as, for example, it took several hours to reach a sufficient CD34+ cell count via FACS. The MACS method required only a fraction of this time and was also more flexibly available.

For irradiation, the CD34+ cells had to be on the Mylar® foil of the cell holder. Two different methods were used for this. In the **first campaign**, the cells were

[3] https://amplitude-laser.com/wp-content/uploads/2019/01/Titan.pdf

Table 5.2.: Samples of the second campaign for gene expression profiling. The complete results of the RIN measurements can be found in the Appendix C.

sample	# shots	RIN	patient	RNA ng/µl	analysed
1a	20	9.8	1	0.538	yes
2a	10	1.5	1	0.162	no
3a	20	N/A	1	0.005	no
4a	0	10	1	0.058	no
5a	10	10	1	0.396	yes
6a	20	6.4	1	0.081	no
7a	20	1	1	0.102	no
8a	0	10	1	0.189	yes
9a	10	8.9	1	0.023	no
10a	10	10	1	0.205	yes
11a	0	10	1	3.253	yes
1b	40	10	2	0.850	yes
2b	10	10	2	1.125	yes
3b	0	N/A	2	1.015	yes
4b	40	10	2	0.418	yes
5b	10	10	2	2.881	yes
6b	0	1	2	0.028	no
7b	40	10	2	2.795	yes
8b	10	10	2	0.233	yes
9b	0	10	2	0.517	yes
10b	40	9	3	0.081	no
11b	10	10	3	0.619	yes
12b	0	10	3	1.636	yes
13b	40	9.4	3	0.971	yes
14b	10	10	3	0.394	yes
15b	0	10	3	0.608	yes
16b	40	10	3	1.583	yes
17b	10	10	3	2.023	yes
18b	0	10	3	0.396	yes

centrifuged and the cell pellet was resuspended in Medium. From this dense cell suspension ($> 10^6$ $\frac{cells}{ml}$), 10 µl were applied to the mylar® foil.

In the **second campaign**, the preparation was changed to reduce the gen expression spread due to the experimental influences between the individual samples. For the irradiation, the CD34+ cells were attached to the Mylar® foil with RetroNectin® (see chapter 5.2.2). The stem cells in medium were incubated in the holders for about 4 hours. This resulted in a slight adhesion of the cells to the Mylar® foil. The connection between the cells and the foil could be loosened again by gentle pipetting.

For the irradiation, part of the supernatant medium was sucked off to prevent the medium from flowing away during the irradiation. Immediately after irradiation, the cells were resuspended with additional culture medium and transferred to 24-well culture plates and then incubated for 18 h. *Stem Span SFEM II* with 10 % *CD34+ expansion supplement* from *STEMCELL Technologies Inc.* was used as the culture medium.

RNA Extraction

After the incubation, the cells were washed of the coverslips with 500 µl PBS. The suspension of cells, medium and PBS was transferred to a micro test tube and lysed in *RLT Buffer* (from *Qiagen*) with β-mercaptoethanol [4], which was added to inactivate RNAses.

To extract the RNA from the cell samples, the *RNeasy Micro Kit* in combination with the *QIAshredder spin columns* from *Qiagen* was used [106, S. 20- 22]. The *QIAshredder spin columns* should increase the RNA yields[5]. Prior to the gene expression profiling the quality of the extracted ribonucleic acid (RNA) samples was tested. The complete results can be found in the Appendix C.

Gene Expression Profiling with DNA Microarrays

In order to quantify the extracted RNA, the samples were given frozen (-70 °C) to the "Biologisch-Medizinisches Forschungszentrum (BMFZ) Genomics & Transcriptomics Labor (GTL)". Only samples that had a RIN value of 9 or higher were used for gene expression analysis. The samples actually evaluated can be found in ta-

[4] https://www.qiagen.com/us/resources/faq?id=2acb974c-4cca-4744-a2cf-60b5f483339b&lang=en

[5] https://www.qiagen.com/~/media/nextq/image%20library/g/00/88/g_0088_qiashredder/1_5

ble 5.2. The RNA concentrations show relatively strong fluctuations, but there are no significant differences in concentration due to the irradiations (0 shots: mean = 0.856 ng/ µl, standard deviation (SD) = 1.033 ng/µl; 10 shots: mean = 0.806 ng/ µl, SD = 0.942 ng/µl; 40 shots: mean = 1.116 ng/µl, SD = 0.968 ng/µl). Furthermore, the relative expression differences are of interest for the evaluation and thus, due to the normalisation, the RNA quantity is irrelevant as long as it is not above or below the working range of the array (0.1 - 10 ng). The "Affymetrix Clariom S Human" system from *Thermo Fisher* was used for acquiring the data.

Data and Data Evaluation

The data include expressions of 21448 genes. For the data analysis the program *Transcriptome Analysis Console (TAC) 4.0* from *Thermo Fisher* was used. In order to obtain better statistics, samples were grouped together and expressions from different groups were thus compared. The main criterion was, of course, the dose, but the other criteria were also taken into account: donor, day of collection and evaluation round.

5.6.2. Results of Gene Expression Profiling

CD34+ cells were irradiated for gene expression in two separate campaigns. For this purpose, the apheresates of the stem cell donors were collected and irradiated as soon as possible after donation. The number of samples to be irradiated resulted in each case from the number of CD34+ cells obtained in the purification. The experimental steps described above were carried out in sequence, and only the extracted RNA was frozen.

First Campaign

In the first gene expression experiment, six samples were evaluated: two unirradiated and two irradiated samples with 10 and 20 shots each. The results showed that radiation induced gene expression pathways are activated such as the "genotoxicity pathway" and "p53 transcriptional gene network". However, there was relatively large statistical variation between samples that actually had an identical treatment. Since gene expression experiments on the same cell type were carried out at the same time by another group in our laboratory, the respective results could be compared. Due to the different experimental conditions, it will not be possible to achieve the

same minimal variations. However, this evaluation allowed us to gain experience for the next round of gene expression analyses and to adapt the experimental procedure. For example, the preparation method for cell irradiation was changed from centrifugation to the RetroNectin® method from the first to the second campaign (see chapter 5.2.2).

Second Campaign

The purified CD34+ cells came from three different healthy donors. From the cell material, 29 test samples were obtained from which the RIN was measured after irradiation. This resulted in 21 samples to be analysed: 7 unirradiated, 8 with 10 shots (5 Gy), 1 with 20 shots (10 Gy) and 5 with 40 shots (20 Gy). The RNA was extracted 18 h after irradiation in each case; a time series was omitted in favour of better statistics. This procedure was chosen because the measurements of the first campaign showed that the experimental procedure already has a clear effect on gene expression. In this way, the effects of LAP irradiation can be clearly identified in the evaluation. As can be seen in figure 5.12 on the right, the number of differentially expressed genes between non-irradiated and irradiated samples is much higher than between the irradiation levels. Furthermore, the overlap of expressions is shown on the right in a Venn digram. More than a quarter of the up- or down-regulated genes between the irradiated and nonirradiated samples match in each case for the examined criteria. There is no overlap between the expressed genes irradiated vs. non-irradiated and the different levels of the irradiated samples. For example the gene GADD45A is upregulated compared to the unirradiated samples (fold change: 2.5 for 10 shots samples and 2.2 for 40 shots samples), which is increased by growth arrest and DNA damages. So, in addition to the individual genes that have been up- or down-regulated, the biological pathways are of interest. The “DNA Damage Response” pathway and the “Genotoxicity pathway” can be verified for both irradiated samples. (Significance: 4.31 and 4.41 for the 10 shots samples and 1.48 and 3.83 for the 40 shots samples. The significance level is calculated with “Fisher’s Exact Test” by the program and the significance is the p-value converted by -log10.)

5.6.3. Conclusion of Gene Expression Profiling

Gene expression of irradiated compared to non-irradiated samples showed the activation of radiation induced gene expression pathways. Accordingly, as can be seen in

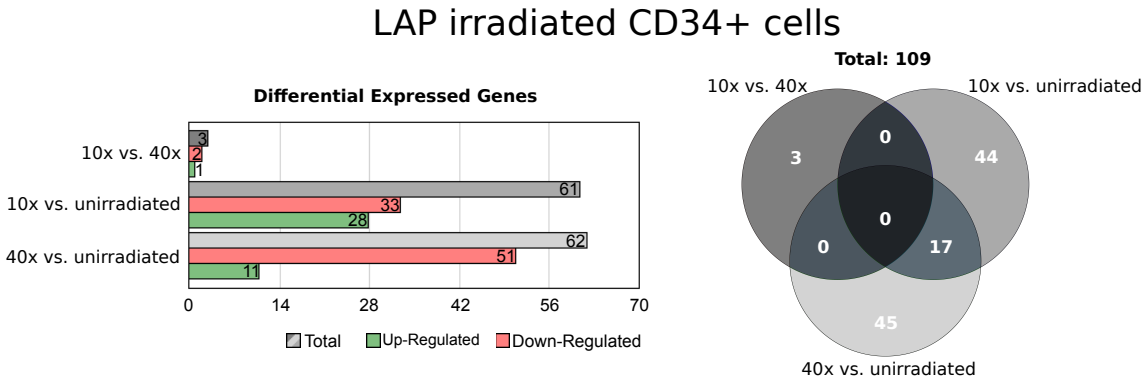

Figure 5.12.: Number of genes with a gene-level fold change < -2 or > 2 and a p-value < 0,05 for the three conditions investigated in the second campaign: unirradiated, 10 shots and 5 Gy (10×) and 40 shots and 20 Gy (40×). *left:* subdivided into up- and down-regulated genes. *right:* A Venn diagram to show the overlap of the expressed genes.

figure 5.12, the expression of individual genes is also irradiation dependent. This can be seen from the Venn diagram, which contains three sets of genes that show a net fold change of more than 2 when comparing the respective experimental situations (and a p-value < 0,05). When comparing the 10× with the 40× irradiated samples, it is noticeable that on the one hand there are very few genes in this set, 3 compared to 61 respectively 62. On the other hand, there is no overlap of this set of genes with the genes of the other groups, whereas there is an overlap of 17 genes in the two groups of irradiated versus non-irradiated samples. Overall, however, it remains to be said that the fluctuations of the gene expression analysis of same treatments are probably far too large to experimentally determine the presumably small variations between conventional and LAP irradiated samples in this way. Experimental improvements are probably needed to be able to detect such a difference.

5.7. Discussion of the Cell Experiments and Possible Improvements

The experiments shown have demonstrated that cell irradiation is feasible with the setup and that radiation-dependent effects can be detected. For example, there is a clear correlation between the number of shots respectively the LAP dose and the double strand breaks. Furthermore, it could be shown that the cells remain vital and can be observed live during the irradiation with the microscope. However, it became

apparent that conditions, which provided a sufficient living environment for the cell lines are not sufficient for stem cells. The major part of the statistical fluctuations in the gene expression analysis of similarly treated samples will have been caused by the non-optimal conditions on the cell holder. (For comparison, the fluctuations in gene expression of the same cell type with the same purification method and the same culture media were very small, as can be seen in publication [107] of a fellow student.) Other biological experiments are also likely to benefit from an improved design of the sample holder, but this would be inevitable for follow-up experiments, especially when using stem cells and in general for highly sensitive analyses such as gene expression profiling. The principle of a revised cell holder would be to ensure the conditions they had in the incubator also during irradiation, as far as possible. Since the cells are only briefly taken out of the incubator (< 0.5 h) for irradiation, a significant improvement could probably already be achieved by greatly increasing the ratio of culture medium volume to cell volume.

In the following, two approaches will be briefly discussed, firstly a larger cell suspension volume and secondly cell irradiation from below. Since the peak power of the laser was increased in the course of this work, more protons can be emitted in the higher energy domain and thus with a greater range. So far, the upgrade has been exploited in such a way that the proton flux onto the sample was greatly increased. However, the energy range of the protons hitting the sample can also be adjusted, so higher proton energies would allow a deeper cell sample. This would, of course, significantly reduce the dose per shot. Since the process shown in figure 5.10 is presumably due to the extremely high dose rate, it would first have to be tested whether this effect can also be achieved with a lower flux at higher proton energies.

The other option is to connect the cell sample holder to the chamber horizontally and not vertically as before. This is by far the more elaborate method, as the entire structure of the vacuum chamber would have to be changed. The big advantage would be that one could take advantage of the higher density of the cells compared to the culture medium and thus, get suspension cells in large numbers on the mylar® foil via a light centrifugation and still have as much medium as desired above the cells. In both cases it should be considered that the changed cell holder also leads to a different oxygen concentration in the cell samples. Since the oxygen concentration is an important variable for the observed effect related to ROS, this effect might possibly disappear due to a “too good” condition of the cells. Therefore, it would

be ideal to have the possibility to measure and adjust the oxygen concentration of the cell samples.

6. Conclusion and Outlook

This thesis describes laser proton source developments and various methods to analyse irradiated cells. The results of the work are presented in three parts. In the following, each topic is briefly concluded and, last but not least, an outlook on possible subsequent experiments and improvements is given. First, the experimental platform is described and its capabilities are outlined. The next part describes mainly the investigated modifications of the proton beam by a timed second laser pulse. The last part deals specifically with the cell experiments carried out.

The basis for proton acceleration is the so-called TNSA process, in which an ultrashort laser pulse interacts with a foil and generates an extremely strong electric field normal to the back of the target, which accelerates the ions at the rear surface. This interaction takes place in a vacuum chamber, which among other things also contains systems for the transport of protons and for supplying new target material. It is shown that the experimental platform is suitable for interesting cell experiments. The platform was further improved in the course of the work. Cell samples can now be irradiated with sequences up to the repetition rate of the Arcturus laser system (5 Hz) and the cells can be observed during the irradiation with an attached fluorescence microscope. Its resolution and sensitivity are sufficient to image subcellular structures even for a long time after irradiation (> 1 h). In its current setup, the microscope can image three different fluorescence channels. Various subcellular structures like mitochondria, DNA and cell surface molecules were imaged in combination with the LAP irradiation. Since the microscope was built with compact open-beam optics it can be adjusted to the experimental requirements easily.

Furthermore, it was demonstrated that the Arcturus laser system offers various possibilities for modifying the proton pulses, which is possible due to its two beam configuration. The analysed data indicate that already at a distance of 1 mm between the laser interaction spots, two largely independent TNSA processes for ion acceleration are triggered. Thus, it is possible to irradiate cell samples with two temporally synchronised and largely identical proton pulses. The time interval be-

tween the pulses can be varied in the range of several ns and can be set precisely to the ps level. The resulting control of the dose rate is particularly interesting in connection with the generation of oxidative stress and the related FLASH research.

Finally, the results of the cell irradiations were shown. The detection of DSBs induced by LAPs and their dependence on the number of TNSA events carried out with fluorescence markers demonstrated the functionality of the experimental platform. Based on this, additional fluorescence markers were used for cell monitoring during irradiation. Here, especially the markers for measuring oxidative stress provided interesting results. No microscopic difference in fluorescence could be measured between the irradiated and non-irradiated sample for LAPs, and no significant difference was measured in FC measurements either. For comparison measurements with X-rays, however, a clear dose dependence was found by using FC. A possible conclusion is that LAPs produce significantly less oxidative stress, which would be very relevant for later clinical applications. Furthermore, gene expression analyses of CD34+ stem cells were performed after irradiation. Here, both the radiation-induced expression of individual genes and the resulting expression of biological pathways could be detected.

For further experiments, gene expression analyses of CD34+ cells on the one hand and further ROS experiments on the other hand are possible. Since the stem cells used for gene expression are very sensitive to unintended external influences, the cell handling during irradiation would have to be completely revised. However, the ROS experiments already showed a very interesting difference between X-ray and LAP irradiated samples. In connection with the currently very active research field of the FLASH effect this offers therefore probably the even more interesting approach for further investigations. Here, the individual samples also showed strong fluctuations, so it would probably be beneficial to revise the cell handling to reduce this. In this context, the improvement of microscopic examination of the cell samples should be approached, as live observation of the ROS signal would be highly interesting. This could possibly already be achieved by precisely controlling the excitation light, as it was strongly affecting the ROS markers.

Comparison experiments of LAPs with X-rays are not the ideal solution, since the observed effect could also be due to the high LET of the low-energy protons, for example. In order to have a radiation source in which only the dose rate differs, initial experiments have already been undertaken in collaboration with the WPE proton therapy centre. As the first experiments have shown, the spectrum cannot

simply be adjusted to match the LAP spectrum by using absorber material (this finding served as the basis for the numerical research paper [108]). However, with the additional application of the magnetic yoke described in this work, promising results were obtained. An other aspect that offers potential for improvement is the dosimetry of the LAPs. An online dosimetry would be ideal here, in order to no longer estimate the dose via the number of shots, but to adjust the number of shots depending on the desired dose.

Bibliography

[1] W. P. Levin, H. Kooy, J. S. Loeffler, and T. F. DeLaney. Proton beam therapy. *British Journal of Cancer*, 93(8):849–854, 2005.

[2] P. Montay-Gruel, K. Petersson, M. Jaccard, G. Boivin, J.-F. Germond, B. Petit, R. Doenlen, V. Favaudon, F. Bochud, C. Bailat, J. Bourhis, and M.-C. Vozenin. Irradiation in a flash: Unique sparing of memory in mice after whole brain irradiation with dose rates above 100 Gy/s. *Radiotherapy and Oncology*, 124(3):365–369, 2017.

[3] H. Al-Hallaq, M. Cao, J. Kruse, and E. Klein. Cured in a FLASH: reducing normal tissue toxicities using ultra-high-dose rates. *International Journal of Radiation Oncology, Biology, Physics*, 104(2):257–260, 2019.

[4] E. S. Diffenderfer, I. I. Verginadis, Mi. M. Kim, K. Shoniyozov, A. Velalopoulou, D. Goia, M. Putt, S. Hagan, S. Avery, K. Teo, W. Zou, A. Lin, S. Swisher-McClure, C. Koch, A. R. Kennedy, A. Minn, A. Maity, T. M. Busch, L. Dong, C. Koumenis, J. Metz, and K. A. Cengel. Design, implementation, and in vivo validation of a novel proton flash radiation therapy system. *International Journal of Radiation Oncology, Biology, Physics*, 106(2):440–448, 2020.

[5] A. Yogo, K. Sato, M. Nishikino, M. Mori, T. Teshima, H. Numasaki, M. Murakami, Y. Demizu, S. Akagi, S. Nagayama, K. Ogura, A. Sagisaka, S. Orimo, M. Nishiuchi, A. S. Pirozhkov, M. Ikegami, M. Tampo, H. Sakaki, M. Suzuki, I. Daito, Y. Oishi, H. Sugiyama, H. Kiriyama, H. Okada, S. Kanazawa, S. Kondo, T. Shimomura, Y. Nakai, M. Tanoue, H. Sasao, D. Wakai, P. R. Bolton, and H. Daido. Application of laser-accelerated protons to the demonstration of DNA double-strand breaks in human cancer cells. *Applied Physics Letters*, 94(18):181502, 2009.

[6] K. Zeil, M. Baumann, E. Beyreuther, T. Burris-Mog, T. E. Cowan, W. Enghardt, L. Karsch, S. D. Kraft, L. Laschinsky, J. Metzkes, D. Naumburger, M. Oppelt, C. Richter, R. Sauerbrey, M. Schürer, U. Schramm, and J. Pawelke. Dose-controlled irradiation of cancer cells with laser-accelerated proton pulses. *Applied Physics B*, 110(4):437–444, 2013.

[7] F. Hanton, P. Chaudhary, D. Doria, D. Gwynne, C. Maiorino, C. Scullion, H. Ahmed, T. Marshall, K. Naughton, L. Romagnani, S. Kar, G. Schettino, P. McKenna, S. Botchway, D. R. Symes, P. P. Rajeev, K. M. Prise, and M. Borghesi. DNA DSB repair dynamics following irradiation with laser-driven protons at ultra-high dose rates. *Scientific Reports*, 9(1):4471, 2019.

[8] S. D. Kraft, C. Richter, K. Zeil, M. Baumann, E. Beyreuther, S. Bock, M. Bussmann, T. E. Cowan, Y. Dammene, W. Enghardt, U. Helbig, L. Karsch, T. Kluge, L. Laschinsky, E. Lessmann, J. Metzkes, D. Naumburger, R. Sauerbrey, M. Schürer, M. Sobiella, J. Woithe, U. Schramm, and J. Pawelke. Dose-dependent biological damage of tumour cells by laser-accelerated proton beams. *New Journal of Physics*, 12(8):085003, 2010.

[9] S. Raschke, S. Spickermann, T. Toncian, M. Swantusch, J. Boeker, U. Giesen, G. Iliakis, O. Willi, and F. Boege. Ultra-short laser-accelerated proton pulses have similar DNA-damaging effectiveness but produce less immediate nitroxidative stress than conventional proton beams. *Scientific Reports*, 6:32441, 2016.

[10] J. Ehlert, M. Piel, F. Boege, M. Cerchez, R. Haas, G. E. Iliakis, R. Prasad, O. Willi, and C. Monzel. An experimental platform for studying the radiation effects of laser accelerated protons on mammalian cells. *AIP Advances*, 11(6):065208, 2021.

[11] T. H. Maiman. Stimulated optical radiation in ruby. *Nature*, 187(4736):493–494, 1960.

[12] D. Strickland and G. Mourou. Compression of amplified chirped optical pulses. *Optics Communications*, 56(3):219–221, 1985.

[13] H. Daido, M. Nishiuchi, and A. S Pirozhkov. Review of laser-driven ion sources and their applications. *Reports on Progress in Physics*, 75(5):056401, 2012.

[14] M. Cerchez, R. Prasad, B. Aurand, A. L. Giesecke, S. Spickermann, S. Brauckmann, E. Aktan, M. Swantusch, M. Toncian, T. Toncian, and O. Willi. Arcturus laser: a versatile high-contrast, high-power multi-beam laser system. *High Power Laser Science and Engineering*, 7, 2019.

[15] Paul Gibbon. *Short pulse laser interactions with matter: an introduction.* World Scientific, 2005.

[16] A. Einstein. Über einen die erzeugung und verwandlung des lichtes betreffenden heuristischen gesichtspunkt. *Annalen der Physik*, 322(6):132–148, 1905.

[17] K. Amini, J. Biegert, F. Calegari, A. Chacon, M. F. Ciappina, A. Dauphin, D. K. Efimov, Carla F. de Morisson Faria, K. Giergiel, P. Gniewek, A. S. Landsman, M. Lesiuk, M. Mandrysz, A. S. Maxwell, R. Moszynski, L. Ortmann, J. Antonio Perez-Hernandez, A. Picon, E. Pisanty, J. Prauzner-Bechcicki, K. Sacha, N. Suarez, A. Zair, J. Zakrzewski, and M. Lewenstein. Symphony on strong field approximation. *Reports on Progress in Physics*, 82(11), 2019.

[18] Francis F. Chen. *Introduction to Plasma Physics and Controlled Fusion.* Springer International Publishing, Cham, 2016.

[19] Andrea Macchi. *A Superintense Laser-Plasma Interaction Theory Primer.* Springer Science & Business Media, Berlin Heidelberg, 2013.

[20] Shalom Eliezer. *The Interaction of High-Power Lasers with Plasmas.* CRC Press, Boca Raton, 2002.

[21] H.-P. Schlenvoigt, O. Jäckel, S. M. Pfotenhauer, and M. C. Kaluza. *Laser-based Particle Acceleration, Advances in Solid State Lasers - Development and Applications.* BoD – Books on Demand, Norderstedt, 2010.

[22] F. Brunel. Not-so-resonant, resonant absorption. *Physical Review Letters*, 59:52–55, 1987.

[23] W. L. Kruer and Kent Estabrook. J×B heating by very intense laser light. *The Physics of Fluids*, 28(1):430–432, 1985.

[24] S. P. Hatchett, C. G. Brown, T. E. Cowan, E. A. Henry, J. S. Johnson, M. H. Key, J. A. Koch, A. B. Langdon, B. F. Lasinski, R. W. Lee, A. J. Mackinnon, D. M. Pennington, M. D. Perry, T. W. Phillips, M. Roth, T. C. Sangster, M. S. Singh, R. A. Snavely, M. A. Stoyer, S. C. Wilks, and K. Yasuike. Electron, photon, and ion beams from the relativistic interaction of petawatt laser pulses with solid targets. *Physics of Plasmas*, 7(5):2076–2082, 2000.

[25] A. Macchi, M. Borghesi, and M. Passoni. Ion acceleration by superintense laser-plasma interaction. *Reviews of Modern Physics*, 85(2):751–793, 2013.

[26] M. Roth and M. Schollmeier. Ion acceleration—target normal sheath acceleration. *CERN Yellow Reports*, 2013.

[27] L. Romagnani, J. Fuchs, M. Borghesi, P. Antici, P. Audebert, F. Ceccherini, T. Cowan, T. Grismayer, S. Kar, A. Macchi, P. Mora, G. Pretzler, A. Schiavi, T. Toncian, and O. Willi. Dynamics of electric fields driving the laser acceleration of multi-MeV protons. *Physical Review Letters*, 95(19):195001, 2005.

[28] S. C. Wilks, A. B. Langdon, T. E. Cowan, M. Roth, M. Singh, S. Hatchett, M. H. Key, D. Pennington, A. MacKinnon, and R. A. Snavely. Energetic proton generation in ultra-intense laser–solid interactions. *Physics of Plasmas*, 8(2):542–549, 2001.

[29] M. Hegelich, S. Karsch, G. Pretzler, D. Habs, K. Witte, W. Guenther, M. Allen, A. Blazevic, J. Fuchs, J. C. Gauthier, M. Geissel, P. Audebert, T. Cowan, and M. Roth. MeV ion jets from short-pulse-laser interaction with thin foils. *Physical Review Letters*, 89:085002, Aug 2002.

[30] R. A. Snavely, M. H. Key, S. P. Hatchett, T. E. Cowan, M. Roth, T. W. Phillips, M. A. Stoyer, E. A. Henry, T. C. Sangster, M. S. Singh, S. C. Wilks, A. MacKinnon, A. Offenberger, D. M. Pennington, K. Yasuike, A. B. Langdon, B. F. Lasinski, J. Johnson, M. D. Perry, and E. M. Campbell. Intense high-energy proton beams from petawatt-laser irradiation of solids. *Physical Review Letters*, 85(14):2945–2948, 2000.

[31] W. H. Bragg and R. Kleeman. LXXIV. on the ionization curves of radium. *The London, Edinburgh, and Dublin Philosophical Magazine and Journal of Science*, 8(48):726–738, 1904.

[32] H. Bethe. Zur Theorie des Durchgangs schneller Korpuskularstrahlen durch Materie. *Annalen der Physik*, 397(3):325–400, 1930.

[33] D. R. Grimes, D. R. Warren, and M. Partridge. An approximate analytical solution of the bethe equation for charged particles in the radiotherapeutic energy range. *Scientific Reports*, 7(1):9781, 2017.

[34] J. J. Wilkens and U. Oelfke. A phenomenological model for the relative biological effectiveness in therapeutic proton beams. *Physics in medicine and biology*, 49(13):2811–2825, 2004.

[35] H. Paganetti. Relative biological effectiveness (RBE) values for proton beam therapy. variations as a function of biological endpoint, dose, and linear energy transfer. *Physics in medicine and biology*, 59(22):R419–R472, 2014.

[36] D. Sadava, G. Orians, H. C. Heller, D. Hillis, and M. R. Berenbaum. *Purves, Biologie*. Spektrum Akademischer Verlag, Heidelberg, 2011.

[37] D. A. Bass, J. W. Parce, L. R. Dechatelet, P. Szejda, M. C. Seeds, and M. Thomas. Flow cytometric studies of oxidative product formation by neutrophils: A graded response to membrane stimulation. *The Journal of Immunology*, 130(4):1910–1917, 1983.

[38] C. P. LeBel, H. Ischiropoulos, and S. C. Bondy. Evaluation of the probe 2', 7'-dichlorofluorescin as an indicator of reactive oxygen species formation and oxidative stress. *Chemical research in toxicology*, 5(2):227–231, 1992.

[39] J. Fulford, H. Nikjoo, D. T. Goodhead, and P. O'Neill. Yields of SSB and DSB induced in DNA by Al (K) ultrasoft X-rays and α-particles: Comparison of experimental and simulated yields. *International Journal of Radiation Biology*, 77(10):1053–1066, 2001.

[40] T. Friedrich, M. Durante, and M. Scholz. Simulation of DSB yield for high LET radiation. *Radiation protection dosimetry*, 166(1-4):61–65, 2015.

[41] L.J. Mah, A. El-Osta, and T. C. Karagiannis. γH2AX: a sensitive molecular marker of DNA damage and repair. *Leukemia*, 24(4):679–686, 2010.

[42] E. M. Kass and M. Jasin. Collaboration and competition between DNA double-strand break repair pathways. *FEBS Letters*, 584(17):3703–3708, 2010.

[43] A. Kakarougkas and P. A. Jeggo. DNA DSB repair pathway choice: An orchestrated handover mechanism. *The British journal of radiology*, 87(1035):20130685, 2014.

[44] M.-C. Vozenin, P. de Fornel, K. Petersson, V. Favaudon, M. Jaccard, J.-F. Germond, B. Petit, M. Burki, G. Ferrand, D. Patin, H. Bouchaab, M. Ozsahin, F. Bochud, C. Bailat, P. Devauchelle, and J. Bourhis. The advantage of flash radiotherapy confirmed in mini-pig and cat-cancer patients. *Clinical Cancer Research*, 25(1):35–42, 2019.

[45] V. Favaudon, L. Caplier, V. Monceau, F. Pouzoulet, M. Sayarath, C. Fouillade, M.-F. Poupon, I. Brito, P. Hupé, J. Bourhis, J. Hall, J.-J. Fontaine, and M.-C. Vozenin. Ultrahigh dose-rate FLASH irradiation increases the differential response between normal and tumor tissue in mice. *Science Translational Medicine*, 6(245):93, 2014.

[46] J. Bourhis, W. J. Sozzi, P. G. Jorge, O. Gaide, C. Bailat, F. Duclos, D. Patin, M. Ozsahin, F. Bochud, J.-F. Germond, R. Moeckli, and M.-C. Vozenin. Treatment of a first patient with FLASH-radiotherapy. *Radiotherapy and oncology: journal of the European Society for Therapeutic Radiology and Oncology*, 139:18–22, 2019.

[47] C. D. Town. Effect of high dose rates on survival of mammalian cells. *Nature*, 215(5103):847–848, 1967.

[48] U. A. Weber, E. Scifoni, and M. Durante. FLASH radiotherapy with carbon ion beams. *Medical Physics*, 2021.

[49] B. Lin, F. Gao, Y. Yang, D. Wu, Y. Zhang, G. Feng, T. Dai, and X. Du. FLASH radiotherapy: History and future. *Frontiers in Oncology*, 11:1890, 2021.

[50] J. D. Wilson, E. M. Hammond, G. S. Higgins, and K. Petersson. Ultra-high dose rate (FLASH) radiotherapy: Silver bullet or fool's gold? *Frontiers in Oncology*, 9:1563, 2020.

[51] J. R. Hughes and J. L. Parsons. FLASH radiotherapy: Current knowledge and future insights using proton-beam therapy. *International Journal of Molecular Sciences*, 21(18):6492, 2020.

[52] B. S. Sørensen and M. R. Horsman. Tumor hypoxia: Impact on radiation therapy and molecular pathways. *Frontiers in Oncology*, 10:562, 2020.

[53] M. Buonanno, V. Grilj, and D. J. Brenner. Biological effects in normal cells exposed to FLASH dose rate protons. *Radiotherapy and Oncology*, 139:51–55, 2019.

[54] G. Adrian, E. Konradsson, M. Lempart, S. Bäck, C. Ceberg, and K. Petersson. The FLASH effect depends on oxygen concentration. *The British Journal of Radiology*, 93(1106):20190702, 2020.

[55] A. Jullien, O. Albert, F. Burgy, G. Hamoniaux, J.-P. Rousseau, J.-P. Chambaret, F. Augé-Rochereau, G. Chériaux, J. Etchepare, N. Minkovski, and S. M. Saltiel. 10^{-10} temporal contrast for femtosecond ultraintense lasers by cross-polarized wave generation. *Optics letters*, 30(8):920–922, 2005.

[56] A. Jullien, S. Kourtev, O. Albert, G. Chériaux, J. Etchepare, N. Minkovski, and S. M. Saltiel. Highly efficient temporal cleaner for femtosecond pulses based on cross-polarized wave generation in a dual crystal scheme. *Applied Physics B*, 84(3):409–414, 2006.

[57] A. Jullien, L. Canova, O. Albert, D. Boschetto, L. Antonucci, Y.-H. Cha, J. P. Rousseau, P. Chaudet, G. Chériaux, J. Etchepare, S. Kourtev, N. Minkovski, and S. M. Saltiel. Spectral broadening and pulse duration reduction during cross-polarized wave generation: Influence of the quadratic spectral phase. *Applied Physics B*, 87(4):595–601, 2007.

[58] T. Oksenhendler, D. Kaplan, P. Tournois, G. M. Greetham, and F. Estable. Intracavity acousto-optic programmable gain control for ultra-wide-band regenerative amplifiers. *Applied Physics B*, 83(4):491, 2006.

[59] B. Dromey, S. Kar, M. Zepf, and P. Foster. The plasma mirror—a subpicosecond optical switch for ultrahigh power lasers. *Review of Scientific Instruments*, 75(3):645–649, 2004.

[60] Ch. Ziener, P. S. Foster, E. J. Divall, C. J. Hooker, M. H. R. Hutchinson, A. J. Langley, and D. Neely. Specular reflectivity of plasma mirrors as a function of intensity, pulse duration, and angle of incidence. *Journal of Applied Physics*, 93(1):768–770, 2003.

[61] A. Alejo, S. Kar, A. Tebartz, H. Ahmed, S. Astbury, D. C. Carroll, J. Ding, D. Doria, A. Higginson, P. McKenna, N. Neumann, G. G. Scott, F. Wagner, M. Roth, and M. Borghesi. High resolution Thomson Parabola Spectrometer for full spectral capture of multi-species ion beams. *Review of Scientific Instruments*, 87(8):083304, 2016.

[62] G. Gillmore, D. Wertheim, and S. Crust. Effects of etching time on alpha tracks in solid state nuclear track detectors. *Science of the Total Environment*, 575:905–909, 2017.

[63] B. Dörschel, R. Bretschneider, D. Hermsdorf, K. Kadner, and H. Kühne. Measurement of the track etch rates along proton and alpha particle trajectories in CR-39 and calculation of the detection efficiency. *Radiation Measurements*, 31(1):103–108, 1999.

[64] X. Zhang, J. Zheng, J. Yan, Z. Yang, M. Su, Y. Pu, P. Yang, X. Xie, L. Chen, M. Chen, T. Huang, S. Jiang, S. Liu, and J. Yang. The application of proton spectrometers at the SG-III facility for ICF implosion areal density diagnostics. *High Power Laser Science and Engineering*, 3:e28, 2015.

[65] Y. He, X. Xi, S. Guo, B. Guo, C. He, F. Liu, X. Lan, M. Qiu, G. Wang, D. Wu, J. Wei, L. Wang, W. Yang, and D. Zhang. Calibration of CR-39 solid state track detectors with monoenergetic protons from 0.3 MeV to 2.5 MeV. *EPJ Web Conf*, 239:07006, 2020.

[66] S. Gaillard, J. Fuchs, N. Renard-Le Galloudec, and T. E. Cowan. Study of saturation of CR39 nuclear track detectors at high ion fluence and of associated artifact patterns. *Review of Scientific Instruments*, 78(1):013304, 2007.

[67] K. Takahashi, K. Kohda, J. Miyahara, Y. Kanemitsu, K. Amitani, and S. Shionoya. Mechanism of photostimulated luminescence in BaFX:Eu^{2+} (X=Cl,Br) phosphors. *Journal of Luminescence*, 31-32:266–268, 1984.

[68] M. Katto, R. Matsumoto, K. Kurosawa, W. Sasaki, Y. Takigawa, and M. Okuda. Laser beam profiler in the vacuum ultraviolet spectral range using photostimulable phosphor. *Review of Scientific Instruments*, 64(2):319–324, 1993.

[69] M. Mori, M. Kando, A. S. Pirozhkov, Y. Hayashi, A. Yogo, N. Yoshimura, K. Ogura, M. Nishiuchi, A. Sagisaka, S. Orimo, M. Kado, A. Fukumi, Z. Li, S. Nakamura, A. Noda, and H. Daido. New detection device for Thomson parabola spectrometer for diagnosis of the laser-plasma ion beam. *Plasma and Fusion Research*, 1:042, 2006.

[70] A. Mančić, J. Fuchs, P. Antici, S. A. Gaillard, and P. Audebert. Absolute calibration of photostimulable image plate detectors used as (0.5–20MeV) high-energy proton detectors. *Review of Scientific Instruments*, 79(7):073301, 2008.

[71] G. J. Williams, B. R. Maddox, H. Chen, S. Kojima, and M. Millecchia. Calibration and equivalency analysis of image plate scanners. *Review of Scientific Instruments*, 85(11):11E604, 2014.

[72] I. J. Paterson, R. J. Clarke, N. C. Woolsey, and G. Gregori. Image plate response for conditions relevant to laser–plasma interaction experiments. *Measurement Science and Technology*, 19(9):095301, 2008.

[73] F. Ingenito, P. Andreoli, D. Batani, G. Boutoux, M. Cipriani, F. Consoli, G. Cristofari, A. Curcio, R. De Angelis, G. Di Giorgio, J. Ducret, P. Forestier-Colleoni, S. Hulin, K. Jakubowska, and N. Rabhi. Comparative calibration of IP scanning equipment. *Journal of Instrumentation*, 11(05):C05012, 2016.

[74] C. G. Soares. Radiochromic film dosimetry. *Radiation Measurements*, 41:S100–S116, 2006.

[75] P. R. Bolton, M. Borghesi, C. Brenner, D. C. Carroll, C. de Martinis, F. Fiorini, A. Flacco, V. Floquet, J. Fuchs, P. Gallegos, D. Giove, J. S. Green, S. Green, B. Jones, D. Kirby, P. McKenna, D. Neely, F. Nuesslin, R. Prasad, S. Reinhardt, M. Roth, U. Schramm, G. G. Scott, S. Ter-Avetisyan, M. Tolley, G. Turchetti, and J. J. Wilkens. Instrumentation for diagnostics and control of laser-accelerated proton (ion) beams. *Physica Medica*, 30(3):255–270, 2014.

[76] H. Alva, H. Mercado-Uribe, M. Rodríguez-Villafuerte, and M. E. Brandan. The use of a reflective scanner to study radiochromic film response. *Physics in Medicine and Biology*, 47(16):2925–2933, 2002.

[77] J. Kalef-Ezra and K. Karava. Radiochromic film dosimetry: reflection vs transmission scanning. *Medical Physics*, 35(6):2308–2311, 2008.

[78] S. N. Chen, M. Gauthier, M. Bazalova-Carter, S. Bolanos, S. Glenzer, R. Riquier, G. Revet, P. Antici, A. Morabito, A. Propp, M. Starodubtsev, and J. Fuchs. Absolute dosimetric characterization of Gafchromic EBT3 and HDv2 films using commercial flat-bed scanners and evaluation of the scanner response function variability. *Review of Scientific Instruments*, 87(7):073301, 2016.

[79] J. F. Ziegler, M. D. Ziegler, and J. P. Biersack. SRIM–the stopping and range of ions in matter. *Nuclear Instruments and Methods in Physics Research Section B: Beam Interactions with Materials and Atoms*, 268(11-12):1818–1823, 2010.

[80] Philipp Weiß. Aufbau einer Experimentierkammer für medizinische Anwendungen von laserbeschleunigten Protonen. Diplomarbeit, Heinrich-Heine-Universität, Düsseldorf, 2011.

[81] O. Willi, M. Behmke, L. Gezici, B. Hidding, R. Jung, T. Königstein, A. Pipahl, J. Osterholz, G. Pretzler, A. Pukhov, M Toncian, T. Toncian, M Heyer, Oliver Jäckel, M. Kübel, G. Paulus, C. Rödel, H.-P. Schlenvoigt, W. Ziegler, and Q. Zhang. Particle and x-ray generation by irradiation of gaseous and solid targets with a 100 TW laser pulse. *Plasma Physics and Controlled Fusion*, 51(12):124049, 2009.

[82] Anna-Marie Schroer. *Investigation of ion acceleration from underdense targets using a high intensity short pulse laser.* Dissertation, Heinrich-Heine-Universität, Düsseldorf, 2018.

[83] Sven Spickermann. *Laser-Driven Ion Beam Characteristics and Dose Measurements for Medical Applications.* Dissertation, Heinrich-Heine-Universität, Düsseldorf, 2019.

[84] K. M. Schwind, E. Aktan, R. Prasad, M. Cerchez, D. Eversheim, O. Willi, and B. Aurand. An online beam profiler for laser-accelerated protons. *Review of Scientific Instruments*, 90(5):053307, 2019.

[85] Abdulraouf Kutaish. Ion beam characteristics generated by two intense laser pulses. Master thesis, Heinrich-Heine-Universität, Düsseldorf, 2020.

[86] Marco Dittrich. Beschleunigung von protonen durch zwei intensive laserpulse. Master thesis, Heinrich-Heine-Universität, Düsseldorf, 2019.

[87] A. P. L. Robinson, D. Neely, P. McKenna, and R. G. Evans. Spectral control in proton acceleration with multiple laser pulses. *Plasma Physics and Controlled Fusion*, 49(4):373–384, 2007.

[88] K. Markey, P. McKenna, C. M. Brenner, D. C. Carroll, M. M. Günther, K. Harres, S. Kar, K. Lancaster, F. Nürnberg, M. N. Quinn, A. P. L. Robinson, M. Roth, M. Zepf, and D. Neely. Spectral enhancement in the double pulse regime of laser proton acceleration. *Physical Review Letters*, 105(19):195008, 2010.

[89] J. Ferri, L. Senje, M. Dalui, K. Svensson, B. Aurand, M. Hansson, A. Persson, O. Lundh, C.-G. Wahlström, L. Gremillet, E. Siminos, T. C. DuBois, L. Yi, J. L. Martins, and T. Fülöp. Proton acceleration by a pair of successive ultraintense femtosecond laser pulses. *Physics of Plasmas*, 25(4):043115, 2018.

[90] N. Šibalić and C. S. Adams. *Rydberg Physics*. 2399-2891. IOP Publishing, 2018.

[91] T. F. Gallagher. Rydberg atoms. *Reports on Progress in Physics*, 51(2):143–188, feb 1988.

[92] P. Chaudhary, G. Milluzzo, H. Ahmed, B. Odlozilik, A. McMurray, K. M. Prise, and M. Borghesi. Radiobiology experiments with ultra-high dose rate laser-driven protons: Methodology and state-of-the-art. *Frontiers in Physics*, 9:75, 2021.

[93] Leibniz-Institut DSMZ- Deutsche Sammlung von Mikroorganismen und Zellkulturen GmbH. Cell line: Kg-1a.

[94] Leibniz-Institut DSMZ- Deutsche Sammlung von Mikroorganismen und Zellkulturen GmbH. Cell line: K-562.

[95] Leibniz-Institut DSMZ- Deutsche Sammlung von Mikroorganismen und Zellkulturen GmbH. Cell line: Ramos.

[96] Leibniz-Institut DSMZ- Deutsche Sammlung von Mikroorganismen und Zellkulturen GmbH. Cell line: Jurkat.

[97] Leibniz-Institut DSMZ- Deutsche Sammlung von Mikroorganismen und Zellkulturen GmbH. Cell line: HeLa.

[98] Leibniz-Institut DSMZ- Deutsche Sammlung von Mikroorganismen und Zellkulturen GmbH. Cell line: A-549.

[99] Eppendorf research® plus bedienungsanleitung, 2016.

[100] K. D. Harshman and P. B. Dervan. Molecular recognition of B-DNA by Hoechst 33258. *Nucleic Acids Research*, 13(13):4825–4835, 1985.

[101] M. J. Heller. DNA microarray technology: Devices, systems, and applications. *Annual Review of Biomedical Engineering*, 4(1):129–153, 2002.

[102] R. Stark, M. Grzelak, and J. Hadfield. RNA sequencing: The teenage years. *Nature Reviews Genetics*, 20(11):631–656, 2019.

[103] X. S. Wan, Z. Zhou, and A. R. Kennedy. Adaptation of the dichlorofluorescein assay for detection of radiation-induced oxidative stress in cultured cells. *Radiation Research*, 160:160 – 160 – 9, 2003.

[104] P. Wardman. Radiotherapy using high-intensity pulsed radiation beams (FLASH): A radiation-chemical perspective. *Radiation Research*, 194(6):607–617, 2020.

[105] G. Baldacchino, E. Brun, I. Denden, S. Bouhadoun, R. Roux, H. Khodja, and C. Sicard-Roselli. Importance of radiolytic reactions during high-let irradiation modalities: LET effect, role of O_2 and radiosensitization by nanoparticles. *Cancer Nanotechnology*, 10(1):3, 2019.

[106] Rneasy® micro handbook, 2014.

[107] S. Fasbender, L. Zimmermann, R.-P. Cadeddu, M. Luysberg, B. Moll, C. Janiak, T. Heinzel, and R. Haas. The low toxicity of graphene quantum dots is reflected by marginal gene expression changes of primary human hematopoietic stem cells. *Scientific Reports*, 9(1):12028, 2019.

[108] C. Behrends, C. Bäumer, N. Verbeek, J. Ehlert, R. Prasad, J. Wulff, A. Lühr, and B. Timmermann. Technical note providing proton fields down to the few-MeV level at clinical 2 pencil beam scanning facilities for radiobiological experiments. *Medical Physics*, 2021.

Danksagung

Zur Entstehung dieser Arbeit haben viele Kommilitonen und Freunde auf verschiedenste Weisen beigetragen, bei denen ich mich bedanken möchte. Beginnen möchte ich bei beiden Betreuern meiner Arbeit: Prof. Dr. Oswald Willi und Prof. Dr. Rainer Haas, die mich zur Promotion angenommen und seither unterstützt haben.

Da ich die meiste Zeit in der Arbeitsgruppe von Prof. Willi verbracht habe, möchte ich an dieser Stelle weitermachen, beginnend mit den Postdocs: Rajendra Prasad, mit dem ich den größten Teil meiner LAP-Versuche durchgeführt habe und der es neben fachlicher Unterstützung immer geschafft hat die Laune und Motivation hoch zu halten. Mirela Cerchez, die bei Fragen immer ein offenes Ohr hatte und unter anderem in mehreren Korrekturrunden viel zur Verbesserung der Arbeit beitrug und nicht zuletzt auch für die gute Kuchenversorgung. Bastian Aurand für die technische Verbesserung des Tape Targets.

Außerdem noch vielen Dank an die weiteren Doktoranden, die mich unterstützt haben. Hier möchte ich nur ein paar namentlich erwähnen. Sven Spickermann, der von physikalischer Seite her mein Vorgänger war und mich stets bei der Einarbeitung unterstützt hat. Esin Aktan, für die gute Zusammenarbeit, die gewinnbringenden Diskussionen und auch für das Rücken freihalten gegen Ende der Promotion.

Aus der Arbeitsgruppe Haas möchte ich stellvertretend Ron-Patrick Cadeddu danken. Hier lernte ich unter anderem die Gewinnung und den Umgang mit primären Zellen. An Cornelia Monzel und ihre Gruppe geht ein weiterer Dank, vor allem für die tatkräftige Unterstützung beim Aufbau des Mikroskops. Weitere Hilfe zu biologischen Fragestellungen bekam ich vom „Institut für Molekulare Medizin I“. Vielen Dank, dass ich sowohl die Laborinfrastruktur nutzen durfte als auch für die Hilfe bei Bioassays und auch für den sonstigen konstruktiven Input. Hier jeden namentlich zu nennen würde mich nur in Gefahr bringen jemanden zu vergessen. Die unzähligen Vergleichsmessungen mit Röntgenstrahlung wären ohne Dennis Sohn nicht möglich gewesen. Außerdem vielen Dank an Prof. George E. Iliakis und Michael Piel vom „Institut für Medizinische Strahlenbiologie UK Essen“. In diesem Zusammenhang

geht mein Dank auch an Carina Behrends und Christian Bäumer für die gute Zusammenarbeit mit dem Westdeutschen Protonentherapiezentrum Essen (WPE).

Zu guter Letzt möchte ich mich auch bei meiner Familie bedanken, bei meiner Frau, die mich unterstützt hat und an vielen Abenden laborbedingt auf mich verzichten musste und bei meinen Eltern, die mich mein gesamtes Studium über unterstützt haben, wie auch bei den Freunden, die mich begleitet haben.

A. Publications

The article **An experimental platform for studying the radiation effects of laser accelerated protons on mammalian cells** was published in **AIP Advances** in the context of this work. The author was involved in the performance of all the experiments shown, as well as in their evaluation; only in the evaluation of the cell data shown in Figure 11 the author was not involved. The first version of the manuscript was written by the author. The revision to the final version was done together with the co-authors, as well as with the external reviewer.

The authors involved in the publication are: J. Ehlert[1,2], M. Piel[3], F. Boege[4], M. Cerchez[1], R. Haas[2], G. E. Iliakis[3], R. Prasad[1], O. Willi[1] and C. Monzel[5]

The technical note **Providing proton fields down to the few-MeV level at clinical pencil beam scanning facilities for radiobiological experiments** was published in **Medical Physics** in the context of this work. Initial experimental trials in collaboration with the Westdeutsches Protonentherapiezentrum Essen (WPE) have shown that it is not possible to match the proton spectrum of a clinical proton emitter to that of the LAPs using absorber material alone. In order to match the spectra as closely as possible, the idea came up to use the same magnetic chicane that is also used for the LAP experiments. As input spectrum to the chicane, one needs as many protons as possible in the desired energy range. For this purpose, SRIM simulations were carried out by the author with the support of colleagues from the Willi's working group, which served as a basis for the TOPAS simulations carried out by the first author of the technical note. Furthermore, the author was

[1]Institute for Laser and Plasma Physics, Heinrich-Heine-University Düsseldorf, 40225 Düsseldorf, Germany.
[2]Department of Haematology, Oncology and Clinical Immunology, Heinrich-Heine-University Düsseldorf, Medical Faculty, 40225 Düsseldorf, Germany.
[3]Institute of Medical Radiation Biology, University Duisburg-Essen, 45122 Essen, Germany.
[4]Institute of Clinical Chemistry and Laboratory Diagnostics, Heinrich-Heine-University Düsseldorf, Medical Faculty, 40225 Düsseldorf, Germany.
[5]Experimental Medical Physics, Heinrich-Heine-University Düsseldorf, 40225 Düsseldorf, Germany

involved in the discussion and revision of the technical note.

The authors involved in the publication are: C. Behrends[6,7,8], C. Bäumer[6,7,8,9], N. Verbeek[6,8,10], J. Ehlert[1,2], R. Prasad[1,11], J. Wulf[6,8], A. Lühr[7] and B. Timmermann[6,8,9,10,12]

[6]West German Proton Therapy Centre Essen (WPE), 45122 Essen, Germany.
[7]Department of Physics, TU Dortmund University, 44227 Dortmund, Germany
[8]University Hospital Essen, West German Cancer Centre (WTZ), 45122 Essen, Germany
[9]German Cancer Consortium (DKTK), Germany
[10]Faculty of Medicine, University of Duisburg-Essen, 45122 Essen, Germany
[11]Present address: Deutsches Elektronen-Synchrotron DESY, 22607 Hamburg, Germany
[12]Department of Particle Therapy, University Hospital Essen, 45122 Essen, Germany

B. Source Codes

```
import matplotlib.pyplot as plt
import scipy
import math
import scipy.interpolate
from scipy import constants
from datetime import date

Datum = date.today()

# Mass and charge of a proton in kg or C:
m = 9.109e-31*1836
q = 1.602e-19
# Radius of the cell port:
r_z = 0.0075
Bz1 = np.loadtxt("D:\Fuer die Versuche geschriebene
    Programme\Feld2.dat")
Bz2 = np.loadtxt("D:\Fuer die Versuche geschriebene
    Programme\Feld1.dat")
# Distance from target to aperture:
blenden_abstand=0.114
# Aperture opening:
blenden_groesse=0.001
# x-coordinate of the aperture:
blenden_eingangsort_x=-0.03

# Number of energy divisions:
nen = 200
# Number of angular steps:
```

```
n_horiz=35
n_vert_angle=11

# Size of the Gap:
gap = 0.05

# Dimensions of the output array:
horiz_pixelzahl=16
vert_pixelzahl=16
pixelzahl = [horiz_pixelzahl,vert_pixelzahl]



minimal = np.zeros(pixelzahl)
minimal[:,:]=10
maximal = np.zeros(pixelzahl)
maximal[:,:]=-1
null_grad = np.zeros(pixelzahl)
null_grad[:,:]=-5
print(null_grad)

minoutput="minimum=␣\n["
maxoutput="maximum=\n["
normoutput="norm=\n["

# Energy range minimum and maximum in eV:
minen=1e6
maxen=7e6



def en_eff( energy, beta):
return energy*math.cos(beta)*math.cos(beta)

# Determination of the initial velocity of protons as a
   function of their kinetic energy:
```

```
def vstartp(Ekin):
E0p=938e6
return 299792458.*math.sqrt(1-E0p*E0p/(E0p+Ekin)/(E0p+Ekin))


def fp( y, t, Bz1, Bz2, gap): # y(0)=x, y(1)=y, y(2)=v_x, y
    (3)=v_y)
m_p=9.109e-31*1836
c_p=1.602e-19
aa = np.shape(Bz1)
xx = np.arange(aa[0])
yy = np.arange(aa[1])
Bz1_interp = scipy.interpolate.interp2d( yy, xx, Bz1,
    fill_value = 0)
Bz2_interp = scipy.interpolate.interp2d( yy, xx, Bz2,
    fill_value = 0)
Bzz = 1e-3 * Bz1_interp(y[1]/0.005+1, y[0]/0.005+5) + 1e-3 *
     Bz2_interp(y[1]/0.005+1, (y[0]-0.1-gap)/0.005+5)
return [y[2],y[3],c_p/m_p*Bzz*y[3],-c_p/m_p*Bzz*y[2]]


min_vert_angle= -math.atan(0.005/(blenden_abstand+0.2+gap))
max_vert_angle= math.atan(0.005/(blenden_abstand+0.2+gap))

winkeldichte= n_horiz/(max_vert_angle-min_vert_angle)

output=np.empty((2,nen))

energien=list(range(nen))
effektiv_energien=np.zeros((nen,n_vert_angle))
effektiv_geschwindigkeiten=np.zeros((nen,n_vert_angle))


yout = list(range(nen))
youtmm = list(range(nen))
```

```
gitteryout = list(range(nen))

yout_bestimmt = np.zeros(nen)

tt = np.linspace(0,1500/999*50e-9,1500)

# Rest energy proton in eV:
E_p = 938272081

# Loop over all energies:
for ien in range(0,nen):#-1):
print("Beginn Energieschleife",ien)
# Determine current energy:
en = minen + (maxen-minen)*ien/(nen-1)
energien[ien] = en
t_end = 1/( np.sqrt(1-E_p*E_p/((E_p+en)*(E_p+en)))*constants
    .c)
t = tt[tt < t_end]

# Loop over all vertical angles:
for i_vert_angle in range(0,n_vert_angle):#-1):
print(i_vert_angle)
if (n_vert_angle > 1):
vert_angle= min_vert_angle + (max_vert_angle-min_vert_angle)
    *i_vert_angle/(n_vert_angle-1)
else:
vert_angle = min_vert_angle
min_horiz_angle= -math.atan(blenden_groesse/(2*
    blenden_abstand))
max_horiz_angle= math.atan(blenden_groesse/(2*
    blenden_abstand))
zz=0.605*math.tan(vert_angle)
n_horiz_angle= round(winkeldichte*(max_horiz_angle-
    min_horiz_angle))
effektiv_energie= en_eff(en,vert_angle)
```

```
effektiv_energien[ien,i_vert_angle]= effektiv_energie
effektiv_geschwindigkeit= vstartp(effektiv_energie)
effektiv_geschwindigkeiten[ien,i_vert_angle]=
    effektiv_geschwindigkeit

# Loop over all horizonal angles:
for i_horiz_angle in range (0,n_horiz_angle):

if(n_horiz_angle > 1) :
horiz_angle= min_horiz_angle + (max_horiz_angle-
    min_horiz_angle)*i_horiz_angle/(n_horiz_angle-1)
else:
horiz_angle = min_horiz_angle

blenden_eingangsort_y=blenden_abstand*np.tan(horiz_angle)
# Initial conditions:
Anfangsbed = [blenden_eingangsort_x,blenden_eingangsort_y,
    math.cos(horiz_angle)*effektiv_geschwindigkeit,math.sin(
    horiz_angle)*effektiv_geschwindigkeit]
Anfangsbed = np.array(Anfangsbed)

yp = scipy.integrate.odeint(fp, Anfangsbed, t, args=(Bz1,
    Bz2, gap))

links=0
mitte=0
rechts=len(t)
zielwert=0.605
while (mitte != round((links+rechts)/2)):
mitte=round((links+rechts)/2)
if (zielwert > yp[mitte,0]):
links=mitte
if (zielwert < yp[mitte,0]):
rechts=mitte
if (zielwert == yp[mitte,0]):
```

```
links=mitte
rechts=mitte

# Create an array with the x and y values of the trajectory:
xtemp = yp[0,:]
xx=xtemp[abs(xtemp) < 0.8]
ytemp = yp[1,:]
yy = ytemp[abs(xtemp) < 0.8]
horiz_auftreff=yp[mitte, 1]

yymm=1000*horiz_auftreff
zzmm=1000*zz
gittery= round(yymm-45)
gittery=int(gittery)
gitterz= round(zzmm+7.5)
gitterz=int(gitterz)
if ((gittery > -0.1) and (gittery < 15.1) and (gitterz >
    -0.1) and (gitterz < 15.1)):
if (en/(1e6) > maximal[gittery,gitterz]):
maximal[gittery,gitterz]=en/(1e6)
geaendert=1
if(en/(1e6) < minimal[gittery,gitterz]):
minimal[gittery,gitterz]=en/(1e6)
geaendert=1

links=0
mittejochende=0
rechts=len(t)
zielwert=0.2+gap
while (mittejochende != round((links+rechts)/2)):
mittejochende=round((links+rechts)/2)
if (zielwert > yp[mittejochende,0]):
links=mittejochende
if (zielwert < yp[mittejochende,0]):
rechts=mittejochende
```

```
if (zielwert == yp[mittejochende,0]):
links=mittejochende
rechts=mittejochende
if (((vert_angle > 0) or (vert_angle == 0)) and ((
    horiz_angle > 0) or (horiz_angle == 0)) and (
    yout_bestimmt[ien] == 0)):
yout[ien]= yp[mittejochende,1]
youtmm[ien]=1000*yout[ien]
gitteryout[ien]=round(youtmm[ien]-45)
yout_bestimmt[ien]=1
plt.plot(yp[:,0],yp[:,1])
print("Ende horizontale Winkelschleife")

output[0,ien]=yout[ien]
output[1,ien]=en

plt.show()
plt.close()



# A 16x16 grid for the energy in MeV of the incoming
    particles:
for ien in range (0,nen):#-1):
print, "Beginn Energieschleife2"
for z in range (0,16):
if ((gitteryout[ien] > -0.1) and (gitteryout[ien] < 15.1)):
null_grad[gitteryout[ien],z]= energien[ien]/1e6



for y in range (0,16):
for z in range (0,16):
minoutput=minoutput+str(round(minimal[z,y],2))
if(z < 15):
minoutput=minoutput+", "
```

```
if(y < 15):
minoutput=minoutput+";\n"
minoutput=minoutput+"]\n"

for y in range(0,16):
for z in range (0,16):
normoutput=normoutput+str(round(null_grad[z,y],2))
if (z < 15):
normoutput=normoutput+", "
if (y < 15): normoutput=normoutput+";\n"
normoutput=normoutput+"]\n"

for y in range(0,16):
for z in range(0,16):
maxoutput=maxoutput+str(round(maximal[z,y],2))
if (z < 15):
maxoutput=maxoutput+", "
if (y < 15): maxoutput=maxoutput+";\n"
maxoutput=maxoutput+"]\n"


print( minoutput)
print( normoutput)
print( maxoutput)

file_ = open("D:\Fuer die Versuche geschriebene Programme\
    MaxNormMin\Minimum_%d_%d_%d_%s_gap%d.dat"%(nen, n_horiz,
    n_vert_angle, Datum, gap*100), 'w')
file_.write(minoutput)
file_.close()

file_ = open("D:/Fuer die Versuche geschriebene Programme/
    MaxNormMin/Norm_%d_%d_%d_%s_gapInCM%d.dat" %(nen,
    n_horiz, n_vert_angle, Datum, gap*100), 'w')
file_.write(normoutput)
```

```
file_.close()

file_ = open('D:\Fuer die Versuche geschriebene Programme\
    MaxNormMin\Maximum_%d_%d_%d_%s_gap%d.dat'%(nen,  n_horiz,
     n_vert_angle, Datum, gap*100), 'w')
file_.write(maxoutput)
file_.close()
```

C. Eukaryote Total RNA Pico

Assay Class: Eukaryote Total RNA Pico
Data Path: C:\...Eukaryote Total RNA Pico_DE13701230_2018-10-16_08-50-59.xad

Created: 10/16/2018 8:50:58 AM
Modified: 10/16/2018 9:13:55 AM

Electrophoresis File Run Summary

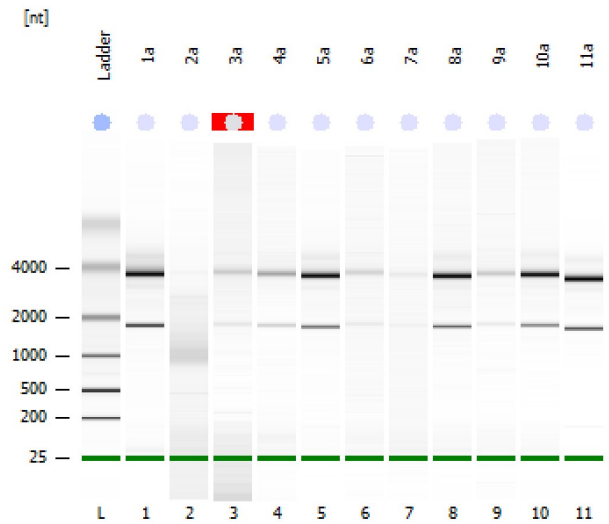

Instrument Information:

Instrument Name: DE13701230 Firmware: C.01.069
Serial#: DE13701230 Type: G2938B

Assay Information:

Assay Origin Path: C:\Program Files (x86)\Agilent\2100 bioanalyzer\2100 expert\assays\RNA\Eukaryote Total RNA Pico Series II.xsy
Assay Class: Eukaryote Total RNA Pico
Version: 2.6
Assay Comments: Total RNA Analysis pg sensitivity (Eukaryote)

Chip Information:

Chip Lot #: WC20BK30
Reagent Kit Lot #: 1751
Chip Comments: Diese Analyse wurde durchgefuehrt von Sandra Plante.

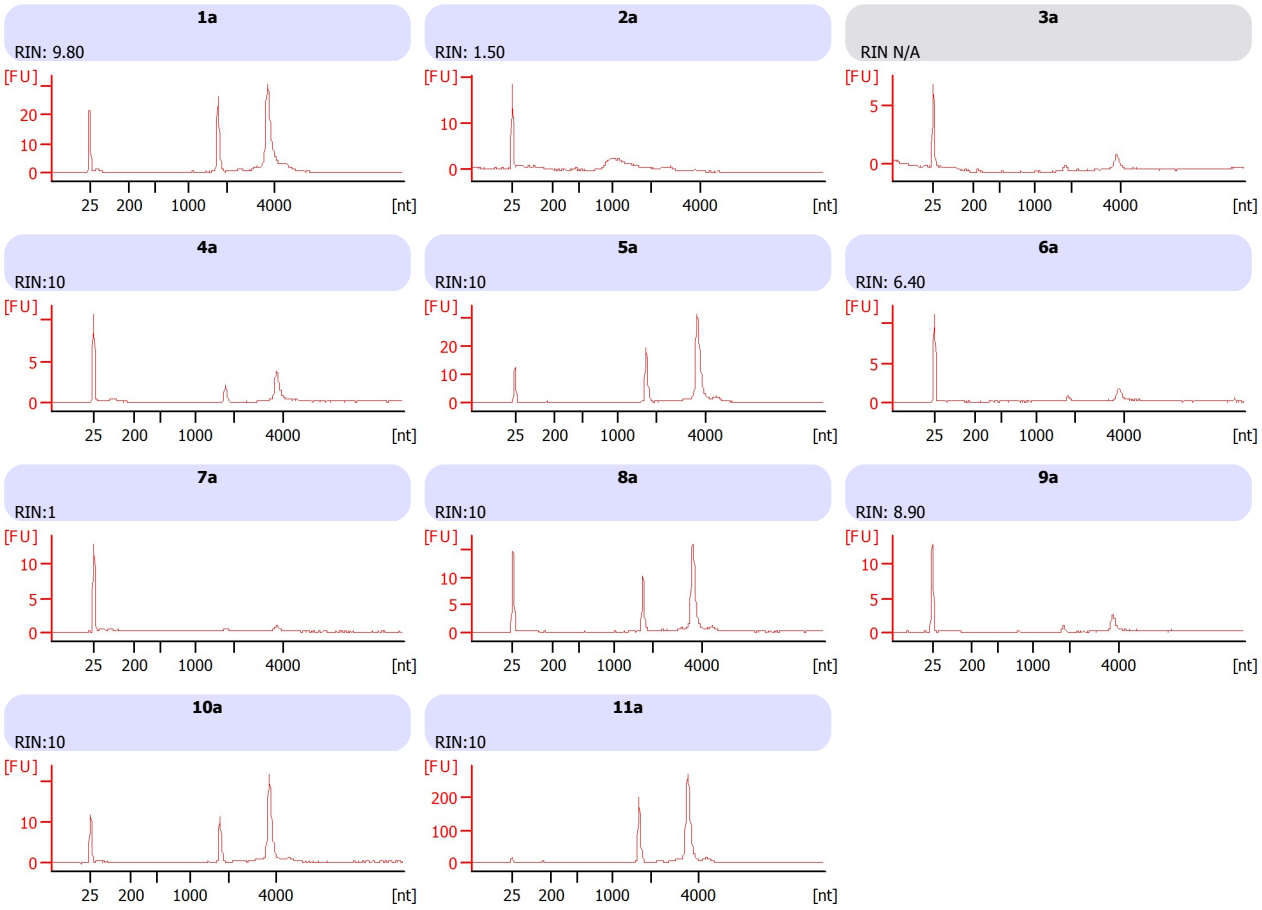

Assay Class: Eukaryote Total RNA Pico
Data Path: C:\...Eukaryote Total RNA Pico_DE13701230_2018-10-16_08-50-59.xad

Created: 10/16/2018 8:50:58 AM
Modified: 10/16/2018 9:13:55 AM

Electrophoresis File Run Summary (Chip Summary)

Sample Name	Sample Comment	Status	Result Label	Result Color
1a		✔	RIN: 9.80	
2a		✔	RIN: 1.50	
3a		✔	RIN N/A	
4a		✔	RIN:10	
5a		✔	RIN:10	
6a		✔	RIN: 6.40	
7a		✔	RIN:1	
8a		✔	RIN:10	
9a		✔	RIN: 8.90	
10a		✔	RIN:10	
11a		✔	RIN:10	
Ladder		✔	All Other Samples	

Chip Lot #	Reagent Kit Lot #
WC20BK30	1751

Chip Comments :

Diese Analyse wurde durchgefuehrt von Sandra Plante.

Assay Class: Eukaryote Total RNA Pico
Data Path: C:\...Eukaryote Total RNA Pico_DE13701230_2018-10-16_08-50-59.xad

Created: 10/16/2018 8:50:58 AM
Modified: 10/16/2018 9:13:55 AM

Electropherogram Summary

Ladder

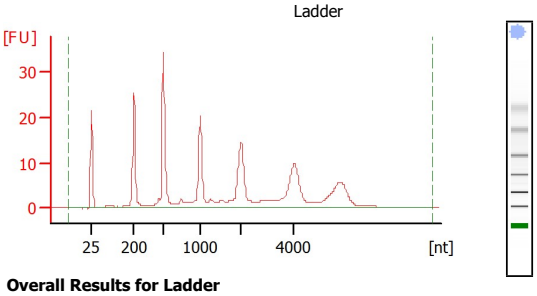

Overall Results for Ladder

RNA Area:	267.9
RNA Concentration:	1,000 pg/µl
Result Flagging Color:	
Result Flagging Label:	All Other Samples

1a

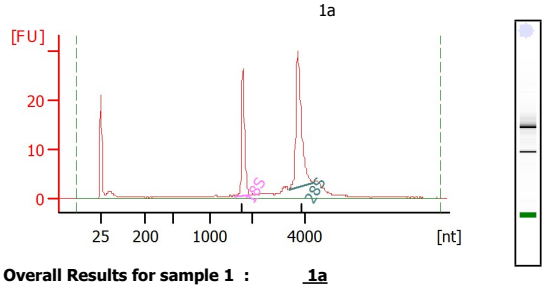

Overall Results for sample 1 : 1a

RNA Area:	144.2
RNA Concentration:	538 pg/µl
rRNA Ratio [28s / 18s]:	1.7
RNA Integrity Number (RIN):	9.8 (B.02.09)
Result Flagging Color:	
Result Flagging Label:	RIN: 9.80

Fragment table for sample 1 : 1a

Name	Start Size [nt]	End Size [nt]	Area	% of total Area
18S	1,587	1,959	28.4	19.7
28S	3,405	4,320	49.0	34.0

2a

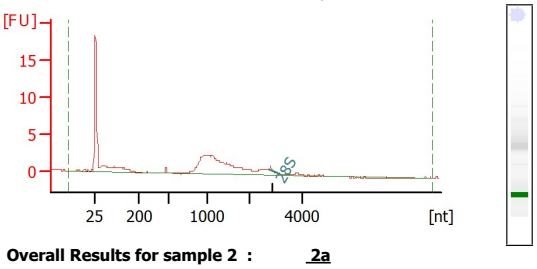

Overall Results for sample 2 : 2a

RNA Area:	43.5
RNA Concentration:	162 pg/µl
rRNA Ratio [28s / 18s]:	0.0
RNA Integrity Number (RIN):	1.5 (B.02.09)
Result Flagging Color:	
Result Flagging Label:	RIN: 1.50

Fragment table for sample 2 : 2a

Name	Start Size [nt]	End Size [nt]	Area	% of total Area
28S	2,738	3,025	0.4	0.9

3a

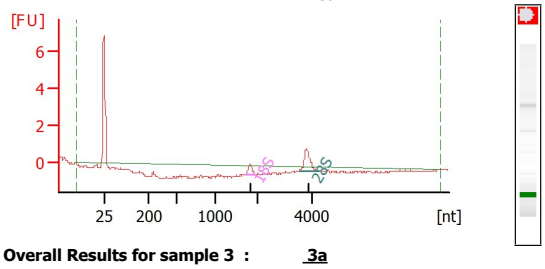

Overall Results for sample 3 : 3a

RNA Area:	1.4
RNA Concentration:	5 pg/µl
rRNA Ratio [28s / 18s]:	2.5
RNA Integrity Number (RIN):	N/A (B.02.09)
Result Flagging Color:	
Result Flagging Label:	RIN N/A

Fragment table for sample 3 : 3a

Name	Start Size [nt]	End Size [nt]	Area	% of total Area
18S	1,697	1,949	0.9	61.5
28S	3,528	4,251	2.2	155.9

Assay Class: Eukaryote Total RNA Pico
Data Path: C:\...Eukaryote Total RNA Pico_DE13701230_2018-10-16_08-50-59.xad

Created: 10/16/2018 8:50:58 AM
Modified: 10/16/2018 9:13:55 AM

Electropherogram Summary Continued ...

4a

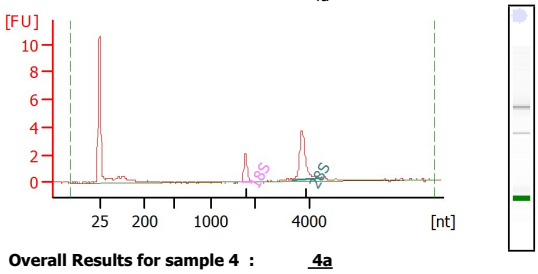

Overall Results for sample 4 : 4a

RNA Area:	15.5
RNA Concentration:	58 pg/µl
rRNA Ratio [28s / 18s]:	2.7
RNA Integrity Number (RIN):	10 (B.02.09)
Result Flagging Color:	
Result Flagging Label:	RIN:10

Fragment table for sample 4 : 4a

Name	Start Size [nt]	End Size [nt]	Area	% of total Area
18S	1,694	1,919	2.3	14.8
28S	3,399	4,386	6.1	39.2

5a

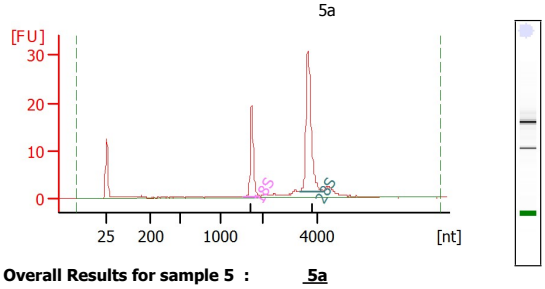

Overall Results for sample 5 : 5a

RNA Area:	106.0
RNA Concentration:	396 pg/µl
rRNA Ratio [28s / 18s]:	2.3
RNA Integrity Number (RIN):	10 (B.02.09)
Result Flagging Color:	
Result Flagging Label:	RIN:10

Fragment table for sample 5 : 5a

Name	Start Size [nt]	End Size [nt]	Area	% of total Area
18S	1,562	1,939	20.1	19.0
28S	3,341	4,227	45.3	42.8

6a

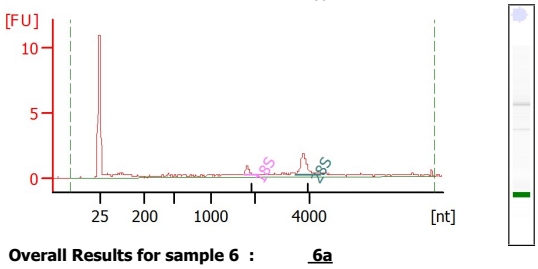

Overall Results for sample 6 : 6a

RNA Area:	21.8
RNA Concentration:	81 pg/µl
rRNA Ratio [28s / 18s]:	3.2
RNA Integrity Number (RIN):	6.4 (B.02.09)
Result Flagging Color:	
Result Flagging Label:	RIN: 6.40

Fragment table for sample 6 : 6a

Name	Start Size [nt]	End Size [nt]	Area	% of total Area
18S	1,746	2,130	0.9	4.2
28S	3,494	4,386	2.9	13.2

7a

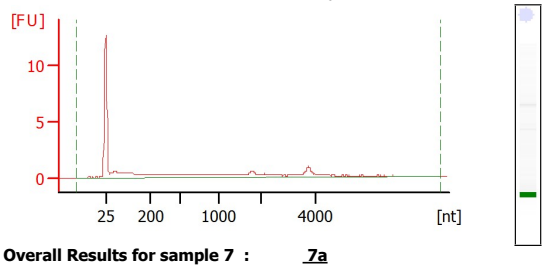

Overall Results for sample 7 : 7a

RNA Area:	27.4
RNA Concentration:	102 pg/µl
rRNA Ratio [28s / 18s]:	0.0
RNA Integrity Number (RIN):	1 (B.02.09)
Result Flagging Color:	
Result Flagging Label:	RIN:1

Assay Class: Eukaryote Total RNA Pico
Data Path: C:\...Eukaryote Total RNA Pico_DE13701230_2018-10-16_08-50-59.xad

Created: 10/16/2018 8:50:58 AM
Modified: 10/16/2018 9:13:55 AM

Electropherogram Summary Continued ...

8a

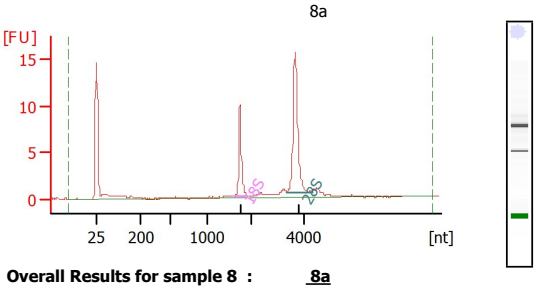

Overall Results for sample 8 : 8a

RNA Area:	50.7
RNA Concentration:	189 pg/µl
rRNA Ratio [28s / 18s]:	2.2
RNA Integrity Number (RIN):	10 (B.02.09)
Result Flagging Color:	
Result Flagging Label:	RIN:10

Fragment table for sample 8 : 8a

Name	Start Size [nt]	End Size [nt]	Area	% of total Area
18S	1,620	1,933	10.1	19.8
28S	3,336	4,274	22.4	44.0

9a

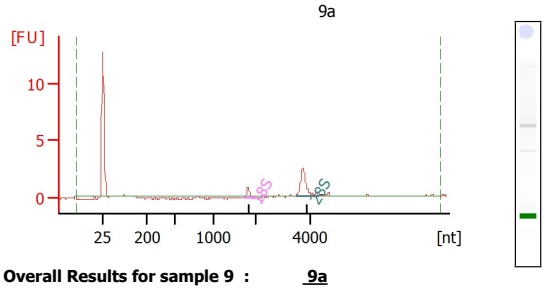

Overall Results for sample 9 : 9a

RNA Area:	6.1
RNA Concentration:	23 pg/µl
rRNA Ratio [28s / 18s]:	3.1
RNA Integrity Number (RIN):	8.9 (B.02.09)
Result Flagging Color:	
Result Flagging Label:	RIN: 8.90

Fragment table for sample 9 : 9a

Name	Start Size [nt]	End Size [nt]	Area	% of total Area
18S	1,701	1,999	1.3	21.5
28S	3,507	4,343	4.1	66.4

10a

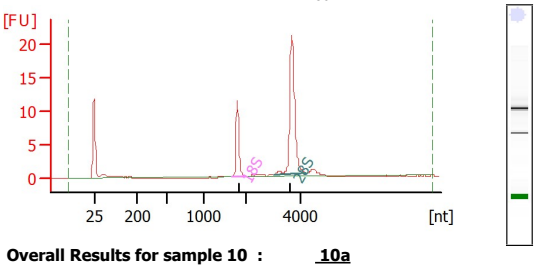

Overall Results for sample 10 : 10a

RNA Area:	54.9
RNA Concentration:	205 pg/µl
rRNA Ratio [28s / 18s]:	2.7
RNA Integrity Number (RIN):	10 (B.02.09)
Result Flagging Color:	
Result Flagging Label:	RIN:10

Fragment table for sample 10 : 10a

Name	Start Size [nt]	End Size [nt]	Area	% of total Area
18S	1,672	1,979	11.9	21.7
28S	3,070	4,241	31.9	58.2

11a

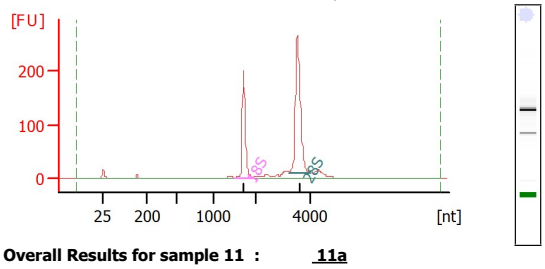

Overall Results for sample 11 : 11a

RNA Area:	871.3
RNA Concentration:	3,253 pg/µl
rRNA Ratio [28s / 18s]:	1.9
RNA Integrity Number (RIN):	10 (B.02.09)
Result Flagging Color:	
Result Flagging Label:	RIN:10

Fragment table for sample 11 : 11a

Name	Start Size [nt]	End Size [nt]	Area	% of total Area
18S	1,484	1,895	216.9	24.9
28S	3,231	4,025	406.6	46.7

Assay Class: Eukaryote Total RNA Pico
Data Path: C:\...Eukaryote Total RNA Pico_DE13701230_2018-10-16_08-50-59.xad

Created: 10/16/2018 8:50:58 AM
Modified: 10/16/2018 9:13:55 AM

Gel Image

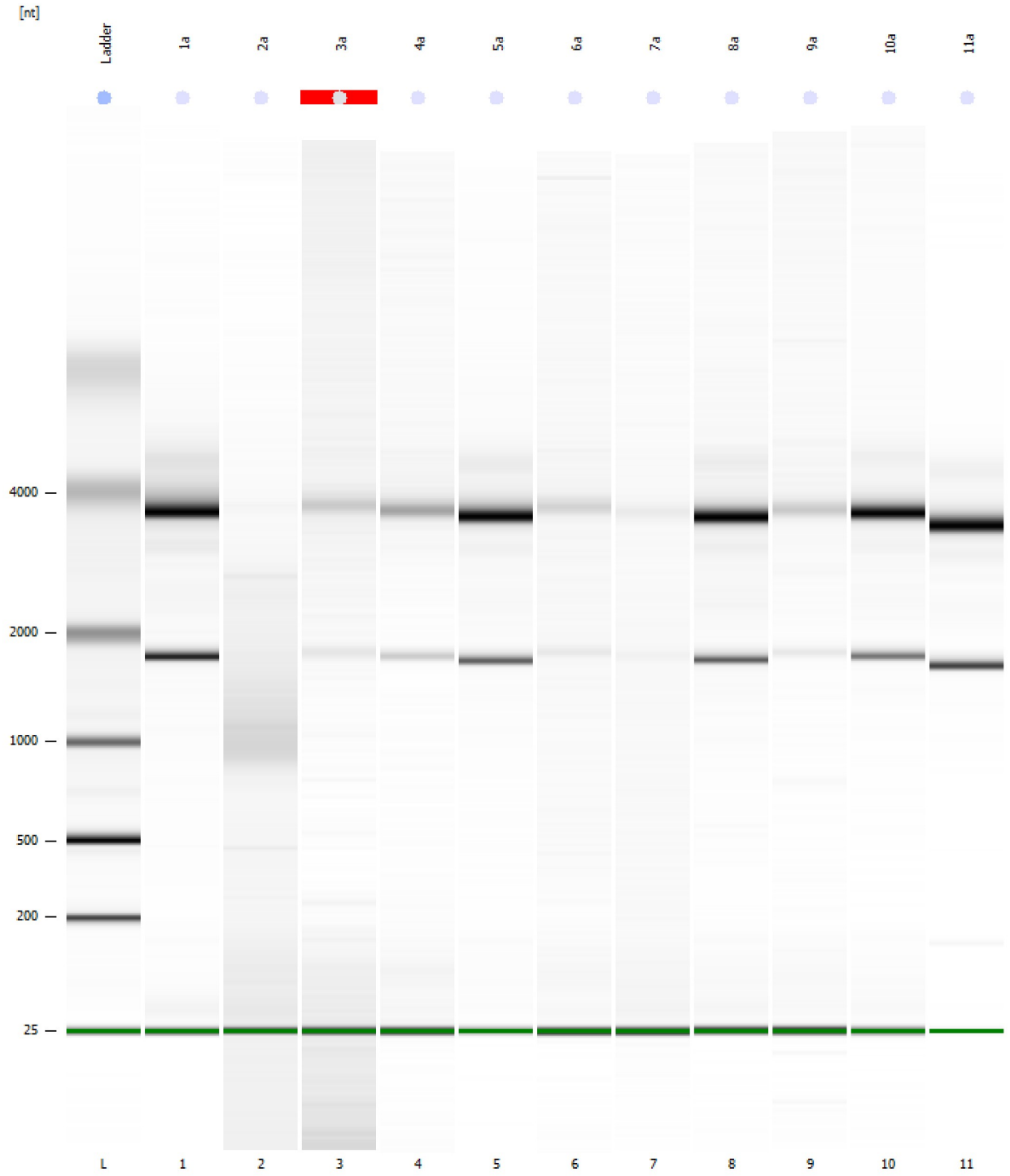

Assay Class: Eukaryote Total RNA Pico
Data Path: C:\...Eukaryote Total RNA Pico_DE13701230_2018-10-16_09-30-29.xad

Created: 10/16/2018 9:30:28 AM
Modified: 10/16/2018 9:52:30 AM

Electrophoresis File Run Summary

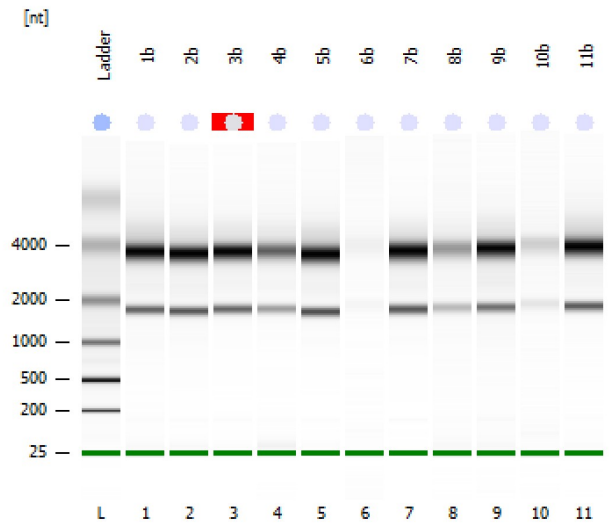

Instrument Information:

Instrument Name:	DE13701230	Firmware:	C.01.069
Serial#:	DE13701230	Type:	G2938B

Assay Information:

Assay Origin Path:	C:\Program Files (x86)\Agilent\2100 bioanalyzer\2100 expert\assays\RNA\Eukaryote Total RNA Pico Series II.xsy
Assay Class:	Eukaryote Total RNA Pico
Version:	2.6
Assay Comments:	Total RNA Analysis pg sensitivity (Eukaryote)

Chip Information:

Chip Lot #:	WC20BK30
Reagent Kit Lot #:	1751
Chip Comments:	Diese Analyse wurde durchgefuehrt von Sandra Plante.

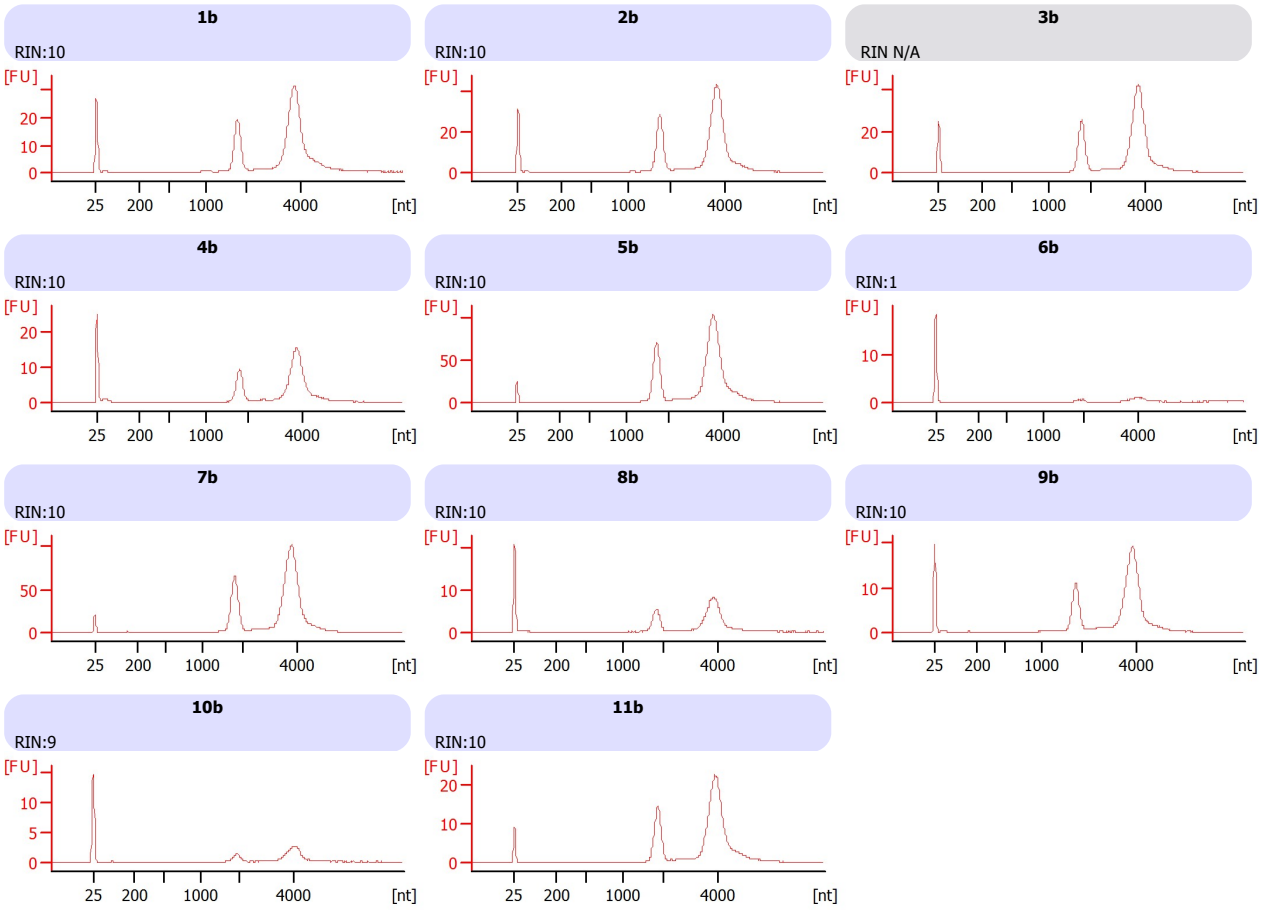

Assay Class: Eukaryote Total RNA Pico
Data Path: C:\...Eukaryote Total RNA Pico_DE13701230_2018-10-16_09-30-29.xad

Created: 10/16/2018 9:30:28 AM
Modified: 10/16/2018 9:52:30 AM

Electrophoresis File Run Summary (Chip Summary)

Sample Name	Sample Comment	Status	Result Label	Result Color
1b		✔	RIN:10	
2b		✔	RIN:10	
3b		✔	RIN N/A	
4b		✔	RIN:10	
5b		✔	RIN:10	
6b		✔	RIN:1	
7b		✔	RIN:10	
8b		✔	RIN:10	
9b		✔	RIN:10	
10b		✔	RIN:9	
11b		✔	RIN:10	
Ladder		✔	All Other Samples	

Chip Lot #	Reagent Kit Lot #
WC20BK30	1751

Chip Comments :

Diese Analyse wurde durchgefuehrt von Sandra Plante.

Assay Class: Eukaryote Total RNA Pico
Data Path: C:\...Eukaryote Total RNA Pico_DE13701230_2018-10-16_09-30-29.xad

Created: 10/16/2018 9:30:28 AM
Modified: 10/16/2018 9:52:30 AM

Electropherogram Summary

Ladder

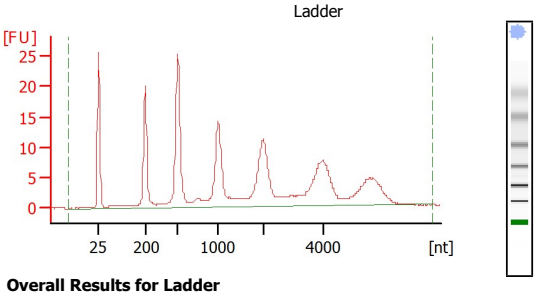

Overall Results for Ladder

RNA Area:	279.3
RNA Concentration:	1,000 pg/µl
Result Flagging Color:	
Result Flagging Label:	All Other Samples

1b

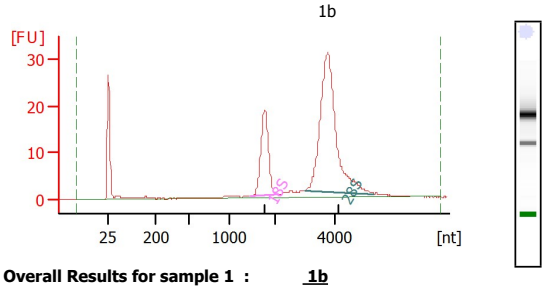

Overall Results for sample 1 : 1b

RNA Area:	237.5
RNA Concentration:	850 pg/µl
rRNA Ratio [28s / 18s]:	2.8
RNA Integrity Number (RIN):	10 (B.02.09)
Result Flagging Color:	
Result Flagging Label:	RIN:10

Fragment table for sample 1 : 1b

Name	Start Size [nt]	End Size [nt]	Area	% of total Area
18S	1,450	2,149	48.7	20.5
28S	2,980	5,301	137.8	58.0

2b

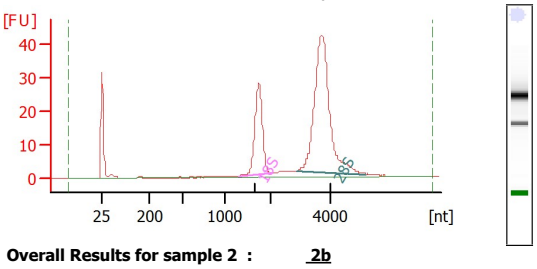

Overall Results for sample 2 : 2b

RNA Area:	314.2
RNA Concentration:	1,125 pg/µl
rRNA Ratio [28s / 18s]:	2.5
RNA Integrity Number (RIN):	10 (B.02.09)
Result Flagging Color:	
Result Flagging Label:	RIN:10

Fragment table for sample 2 : 2b

Name	Start Size [nt]	End Size [nt]	Area	% of total Area
18S	1,321	2,078	71.7	22.8
28S	2,864	5,125	180.5	57.5

3b

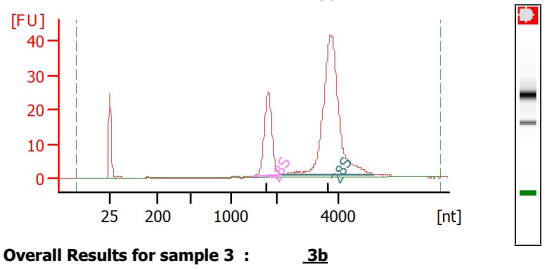

Overall Results for sample 3 : 3b

RNA Area:	283.5
RNA Concentration:	1,015 pg/µl
rRNA Ratio [28s / 18s]:	2.9
RNA Integrity Number (RIN):	N/A (B.02.09)
Result Flagging Color:	
Result Flagging Label:	RIN N/A

Fragment table for sample 3 : 3b

Name	Start Size [nt]	End Size [nt]	Area	% of total Area
18S	1,456	2,139	64.0	22.6
28S	2,163	5,179	183.1	64.6

Assay Class: Eukaryote Total RNA Pico
Data Path: C:\...Eukaryote Total RNA Pico_DE13701230_2018-10-16_09-30-29.xad

Created: 10/16/2018 9:30:28 AM
Modified: 10/16/2018 9:52:30 AM

Electropherogram Summary Continued ...

4b

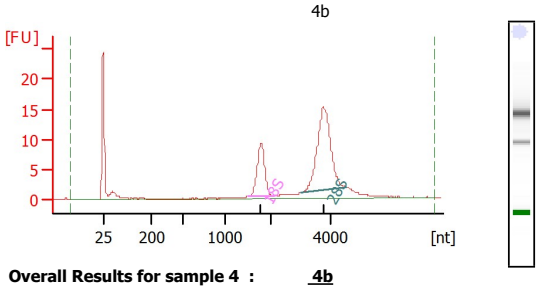

Overall Results for sample 4 : 4b

RNA Area:	116.7
RNA Concentration:	418 pg/µl
rRNA Ratio [28s / 18s]:	2.4
RNA Integrity Number (RIN):	10 (B.02.09)
Result Flagging Color:	
Result Flagging Label:	RIN:10

Fragment table for sample 4 : 4b

Name	Start Size [nt]	End Size [nt]	Area	% of total Area
18S	1,526	2,126	23.5	20.2
28S	2,989	4,522	55.3	47.4

5b

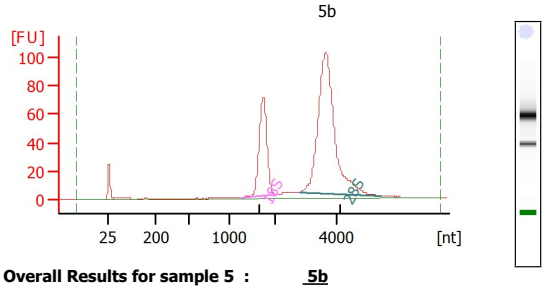

Overall Results for sample 5 : 5b

RNA Area:	804.6
RNA Concentration:	2,881 pg/µl
rRNA Ratio [28s / 18s]:	2.5
RNA Integrity Number (RIN):	10 (B.02.09)
Result Flagging Color:	
Result Flagging Label:	RIN:10

Fragment table for sample 5 : 5b

Name	Start Size [nt]	End Size [nt]	Area	% of total Area
18S	1,274	2,052	190.3	23.7
28S	2,820	5,502	479.0	59.5

6b

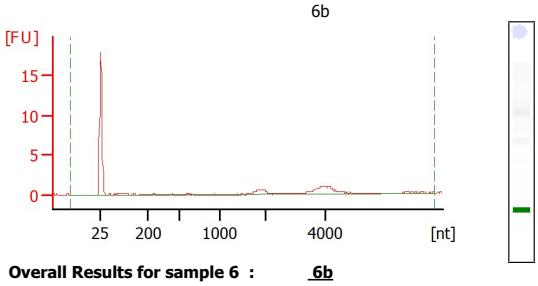

Overall Results for sample 6 : 6b

RNA Area:	7.9
RNA Concentration:	28 pg/µl
rRNA Ratio [28s / 18s]:	0.0
RNA Integrity Number (RIN):	1 (B.02.09)
Result Flagging Color:	
Result Flagging Label:	RIN:1

7b

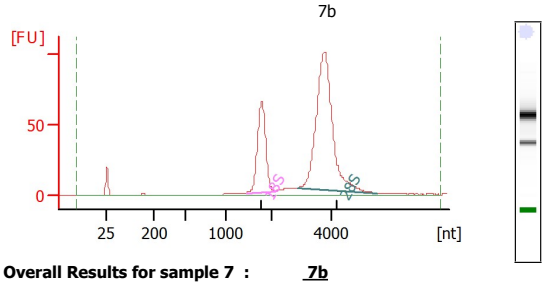

Overall Results for sample 7 : 7b

RNA Area:	780.6
RNA Concentration:	2,795 pg/µl
rRNA Ratio [28s / 18s]:	2.5
RNA Integrity Number (RIN):	10 (B.02.09)
Result Flagging Color:	
Result Flagging Label:	RIN:10

Fragment table for sample 7 : 7b

Name	Start Size [nt]	End Size [nt]	Area	% of total Area
18S	1,442	2,111	184.5	23.6
28S	2,888	5,580	468.3	60.0

Assay Class: Eukaryote Total RNA Pico
Data Path: C:\...Eukaryote Total RNA Pico_DE13701230_2018-10-16_09-30-29.xad

Created: 10/16/2018 9:30:28 AM
Modified: 10/16/2018 9:52:30 AM

Electropherogram Summary Continued ...

8b

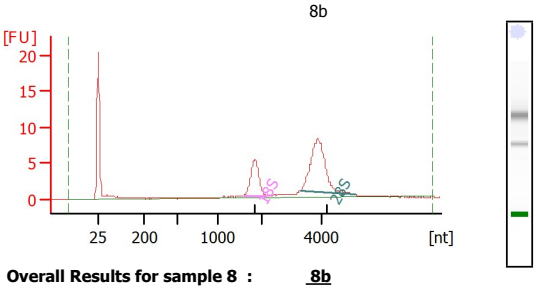

Overall Results for sample 8 : 8b

RNA Area:	65.0
RNA Concentration:	233 pg/µl
rRNA Ratio [28s / 18s]:	2.2
RNA Integrity Number (RIN):	10 (B.02.09)
Result Flagging Color:	
Result Flagging Label:	RIN:10

Fragment table for sample 8 : 8b

Name	Start Size [nt]	End Size [nt]	Area	% of total Area
18S	1,580	2,135	14.6	22.4
28S	3,273	5,092	32.5	50.0

9b

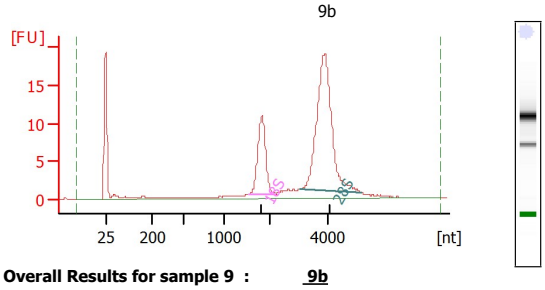

Overall Results for sample 9 : 9b

RNA Area:	144.3
RNA Concentration:	517 pg/µl
rRNA Ratio [28s / 18s]:	2.8
RNA Integrity Number (RIN):	10 (B.02.09)
Result Flagging Color:	
Result Flagging Label:	RIN:10

Fragment table for sample 9 : 9b

Name	Start Size [nt]	End Size [nt]	Area	% of total Area
18S	1,536	2,221	28.7	19.9
28S	3,054	5,091	79.5	55.1

10b

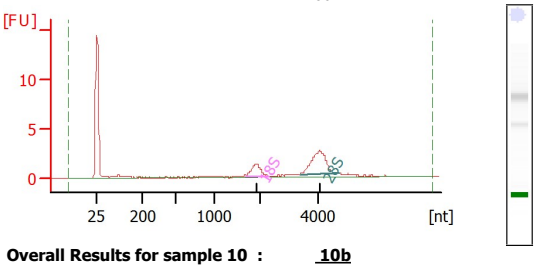

Overall Results for sample 10 : 10b

RNA Area:	22.7
RNA Concentration:	81 pg/µl
rRNA Ratio [28s / 18s]:	2.5
RNA Integrity Number (RIN):	9 (B.02.09)
Result Flagging Color:	
Result Flagging Label:	RIN:9

Fragment table for sample 10 : 10b

Name	Start Size [nt]	End Size [nt]	Area	% of total Area
18S	1,691	2,308	3.9	17.0
28S	3,381	4,679	9.8	42.9

11b

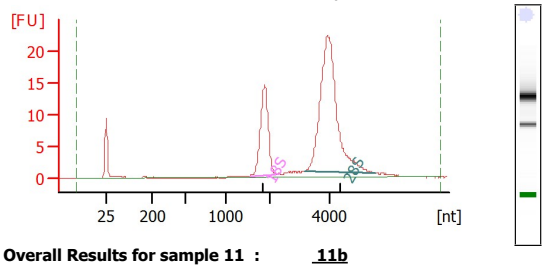

Overall Results for sample 11 : 11b

RNA Area:	173.0
RNA Concentration:	619 pg/µl
rRNA Ratio [28s / 18s]:	2.7
RNA Integrity Number (RIN):	10 (B.02.09)
Result Flagging Color:	
Result Flagging Label:	RIN:10

Fragment table for sample 11 : 11b

Name	Start Size [nt]	End Size [nt]	Area	% of total Area
18S	1,539	2,172	38.6	22.3
28S	3,187	5,512	102.6	59.3

Assay Class: Eukaryote Total RNA Pico
Data Path: C:\...Eukaryote Total RNA Pico_DE13701230_2018-10-16_09-30-29.xad

Created: 10/16/2018 9:30:28 AM
Modified: 10/16/2018 9:52:30 AM

Gel Image

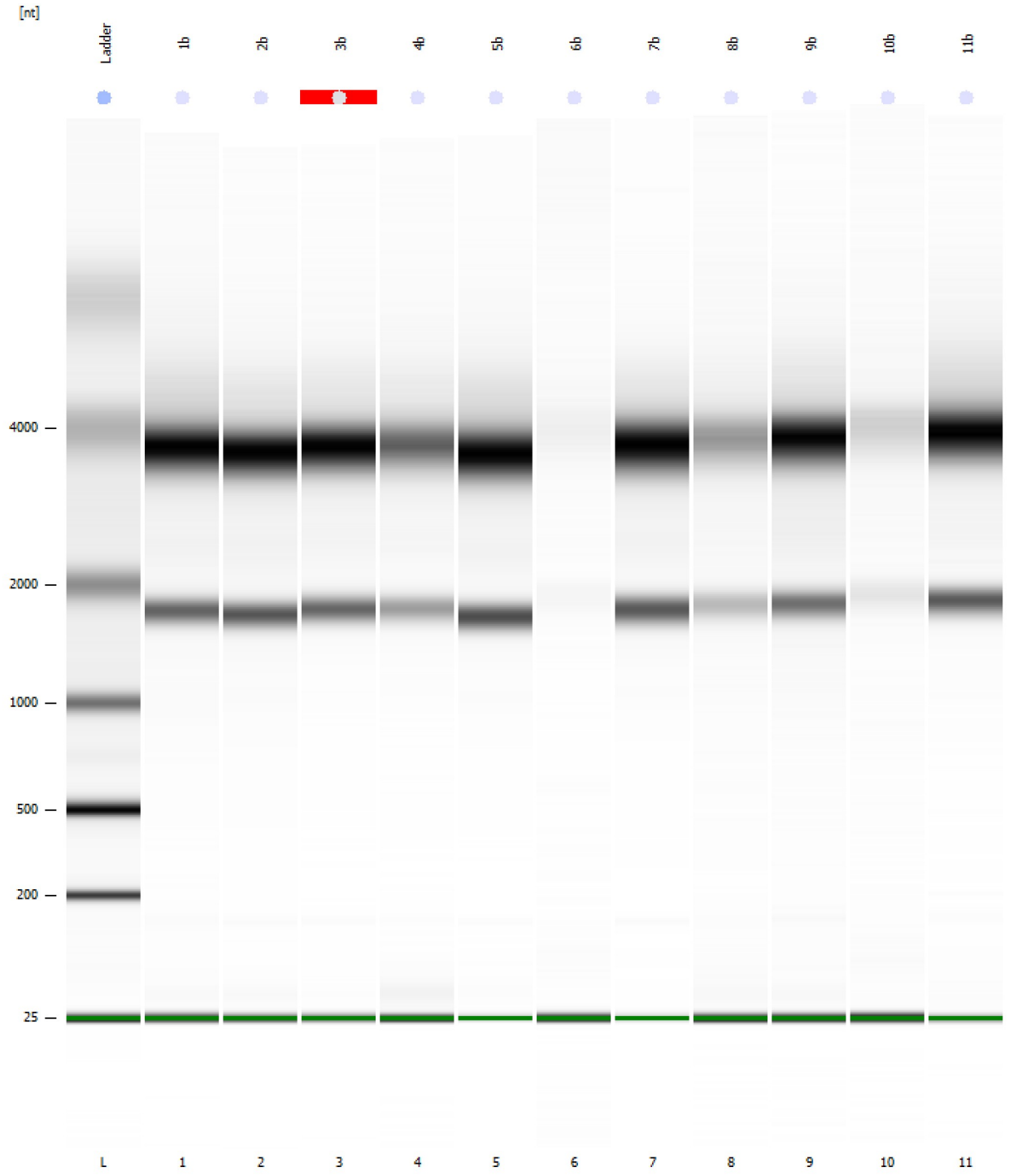

Assay Class: Eukaryote Total RNA Pico
Data Path: C:\...Eukaryote Total RNA Pico_DE13701230_2018-10-16_10-08-33.xad

Created: 10/16/2018 10:08:32 AM
Modified: 10/16/2018 10:30:35 AM

Electrophoresis File Run Summary

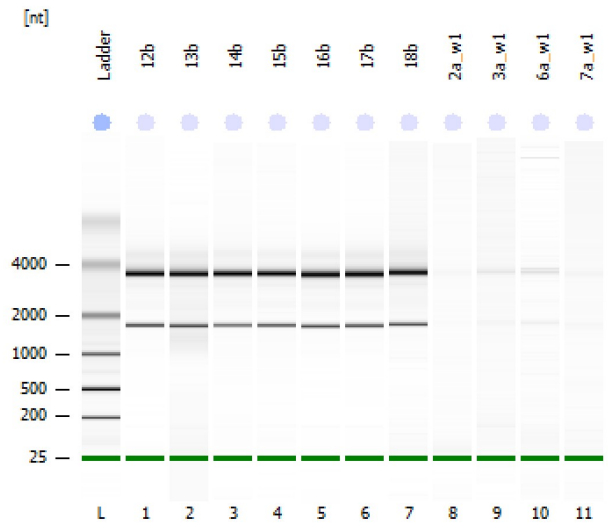

Instrument Information:

Instrument Name:	DE13701230	Firmware:	C.01.069
Serial#:	DE13701230	Type:	G2938B

Assay Information:

Assay Origin Path:	C:\Program Files (x86)\Agilent\2100 bioanalyzer\2100 expert\assays\RNA\Eukaryote Total RNA Pico Series II.xsy
Assay Class:	Eukaryote Total RNA Pico
Version:	2.6
Assay Comments:	Total RNA Analysis pg sensitivity (Eukaryote)

Chip Information:

Chip Lot #:	WC20BK30
Reagent Kit Lot #:	1751
Chip Comments:	Diese Analyse wurde durchgefuehrt von Sandra Plante.

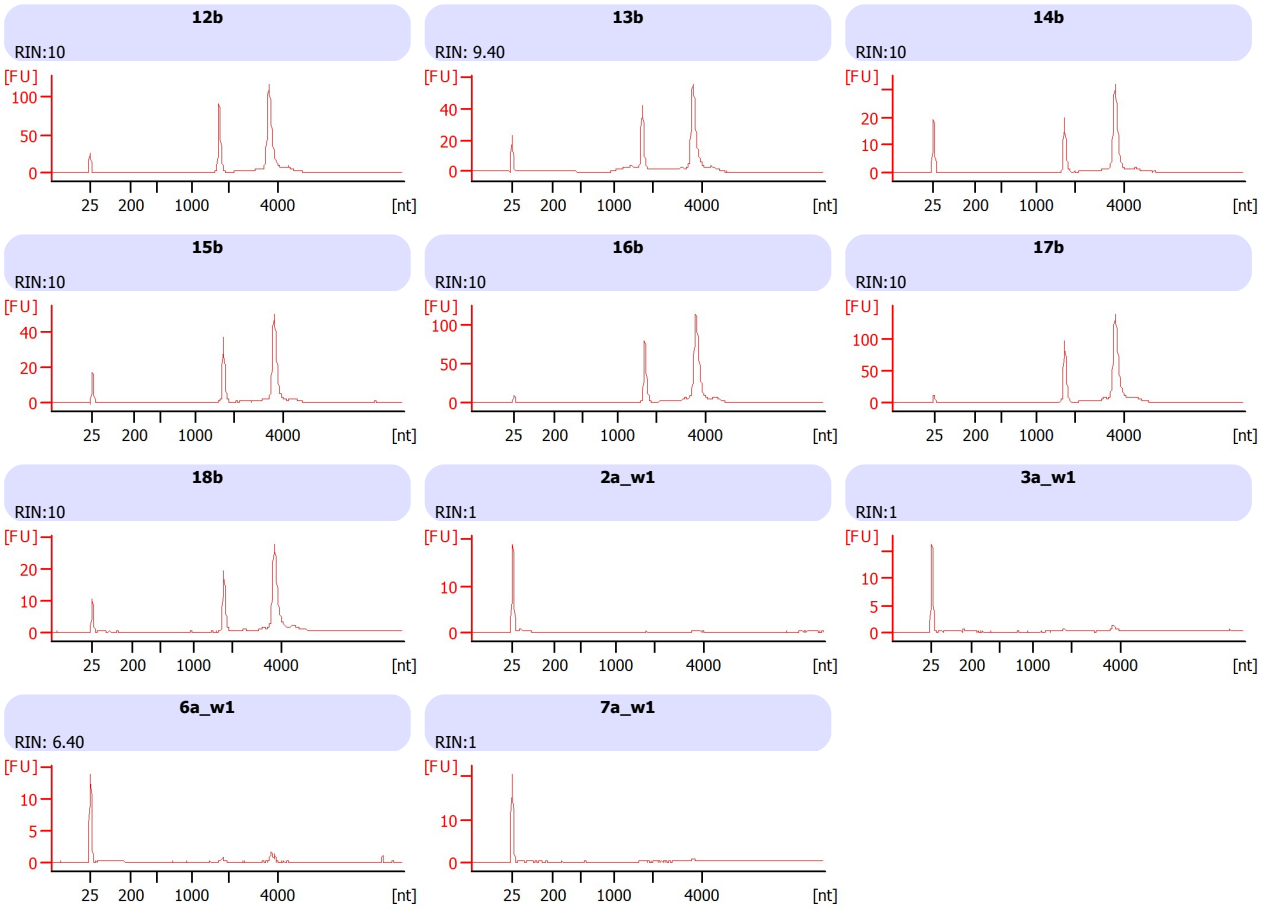

Assay Class: Eukaryote Total RNA Pico
Data Path: C:\...Eukaryote Total RNA Pico_DE13701230_2018-10-16_10-08-33.xad

Created: 10/16/2018 10:08:32 AM
Modified: 10/16/2018 10:30:35 AM

Electrophoresis File Run Summary (Chip Summary)

Sample Name	Sample Comment	Status	Result Label	Result Color
12b		✔	RIN:10	
13b		✔	RIN: 9.40	
14b		✔	RIN:10	
15b		✔	RIN:10	
16b		✔	RIN:10	
17b		✔	RIN:10	
18b		✔	RIN:10	
2a_w1		✔	RIN:1	
3a_w1		✔	RIN:1	
6a_w1		✔	RIN: 6.40	
7a_w1		✔	RIN:1	
Ladder		✔	All Other Samples	

Chip Lot #	Reagent Kit Lot #
WC20BK30	1751

Chip Comments :

Diese Analyse wurde durchgefuehrt von Sandra Plante.

Assay Class: Eukaryote Total RNA Pico
Data Path: C:\...Eukaryote Total RNA Pico_DE13701230_2018-10-16_10-08-33.xad

Created: 10/16/2018 10:08:32 AM
Modified: 10/16/2018 10:30:35 AM

Electropherogram Summary

Ladder

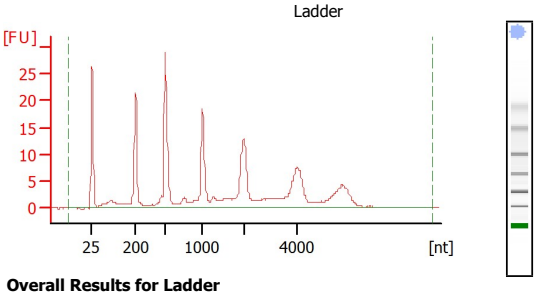

Overall Results for Ladder

RNA Area:	249.1
RNA Concentration:	1,000 pg/µl
Result Flagging Color:	
Result Flagging Label:	All Other Samples

12b

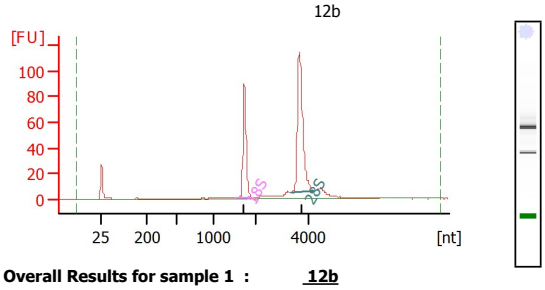

Overall Results for sample 1 : 12b

RNA Area:	407.4
RNA Concentration:	1,636 pg/µl
rRNA Ratio [28s / 18s]:	1.8
RNA Integrity Number (RIN):	10 (B.02.09)
Result Flagging Color:	
Result Flagging Label:	RIN:10

Fragment table for sample 1 : 12b

Name	Start Size [nt]	End Size [nt]	Area	% of total Area
18S	1,553	1,933	99.0	24.3
28S	3,343	4,189	182.1	44.7

13b

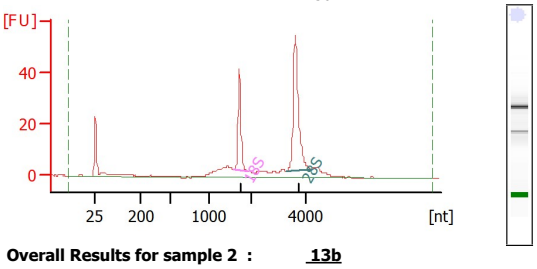

Overall Results for sample 2 : 13b

RNA Area:	241.8
RNA Concentration:	971 pg/µl
rRNA Ratio [28s / 18s]:	2.0
RNA Integrity Number (RIN):	9.4 (B.02.09)
Result Flagging Color:	
Result Flagging Label:	RIN: 9.40

Fragment table for sample 2 : 13b

Name	Start Size [nt]	End Size [nt]	Area	% of total Area
18S	1,588	1,920	43.1	17.8
28S	3,321	4,212	87.4	36.2

14b

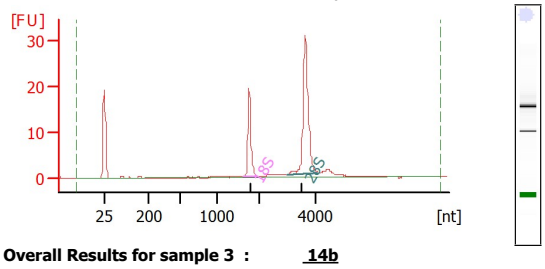

Overall Results for sample 3 : 14b

RNA Area:	98.2
RNA Concentration:	394 pg/µl
rRNA Ratio [28s / 18s]:	2.3
RNA Integrity Number (RIN):	10 (B.02.09)
Result Flagging Color:	
Result Flagging Label:	RIN:10

Fragment table for sample 3 : 14b

Name	Start Size [nt]	End Size [nt]	Area	% of total Area
18S	1,600	1,931	21.1	21.4
28S	2,995	4,111	49.1	49.9

Assay Class: Eukaryote Total RNA Pico
Data Path: C:\...Eukaryote Total RNA Pico_DE13701230_2018-10-16_10-08-33.xad

Created: 10/16/2018 10:08:32 AM
Modified: 10/16/2018 10:30:35 AM

Electropherogram Summary Continued ...

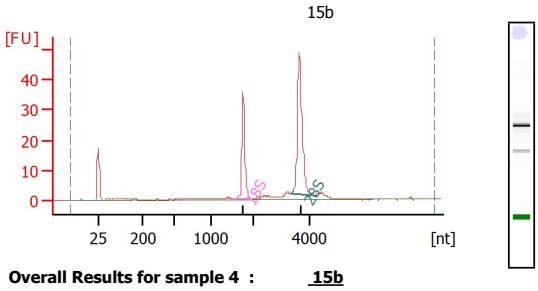

Overall Results for sample 4 : 15b

RNA Area:	151.4
RNA Concentration:	608 pg/µl
rRNA Ratio [28s / 18s]:	1.9
RNA Integrity Number (RIN):	10 (B.02.09)
Result Flagging Color:	
Result Flagging Label:	RIN:10

Fragment table for sample 4 : 15b

Name	Start Size [nt]	End Size [nt]	Area	% of total Area
18S	1,566	1,922	37.9	25.0
28S	3,345	4,178	71.9	47.5

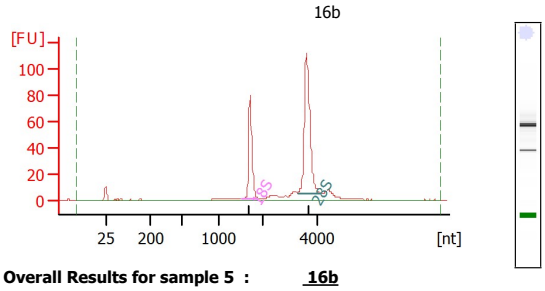

Overall Results for sample 5 : 16b

RNA Area:	394.3
RNA Concentration:	1,583 pg/µl
rRNA Ratio [28s / 18s]:	2.0
RNA Integrity Number (RIN):	10 (B.02.09)
Result Flagging Color:	
Result Flagging Label:	RIN:10

Fragment table for sample 5 : 16b

Name	Start Size [nt]	End Size [nt]	Area	% of total Area
18S	1,527	1,908	92.0	23.3
28S	3,273	4,141	184.8	46.9

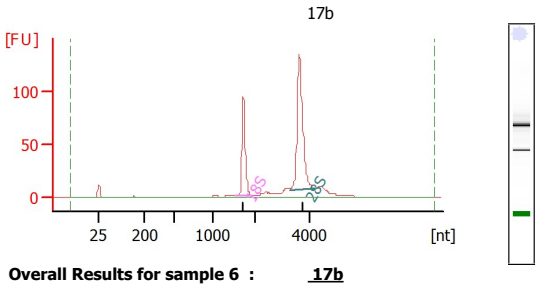

Overall Results for sample 6 : 17b

RNA Area:	503.9
RNA Concentration:	2,023 pg/µl
rRNA Ratio [28s / 18s]:	2.0
RNA Integrity Number (RIN):	10 (B.02.09)
Result Flagging Color:	
Result Flagging Label:	RIN:10

Fragment table for sample 6 : 17b

Name	Start Size [nt]	End Size [nt]	Area	% of total Area
18S	1,550	1,914	113.7	22.6
28S	3,303	4,201	223.7	44.4

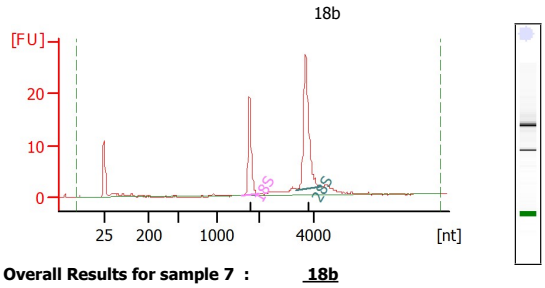

Overall Results for sample 7 : 18b

RNA Area:	98.6
RNA Concentration:	396 pg/µl
rRNA Ratio [28s / 18s]:	2.0
RNA Integrity Number (RIN):	10 (B.02.09)
Result Flagging Color:	
Result Flagging Label:	RIN:10

Fragment table for sample 7 : 18b

Name	Start Size [nt]	End Size [nt]	Area	% of total Area
18S	1,599	1,991	21.6	21.9
28S	3,373	4,249	42.9	43.5

Assay Class: Eukaryote Total RNA Pico
Data Path: C:\...Eukaryote Total RNA Pico_DE13701230_2018-10-16_10-08-33.xad

Created: 10/16/2018 10:08:32 AM
Modified: 10/16/2018 10:30:35 AM

Electropherogram Summary Continued ...

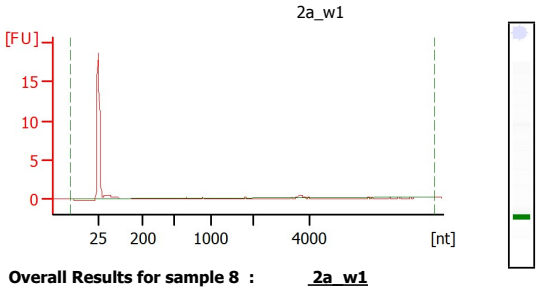

Overall Results for sample 8 : 2a_w1

RNA Area:	4.6
RNA Concentration:	19 pg/µl
rRNA Ratio [28s / 18s]:	0.0
RNA Integrity Number (RIN):	1 (B.02.09)
Result Flagging Color:	
Result Flagging Label:	RIN:1

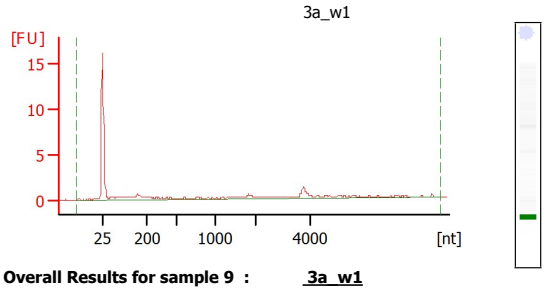

Overall Results for sample 9 : 3a_w1

RNA Area:	23.3
RNA Concentration:	93 pg/µl
rRNA Ratio [28s / 18s]:	0.0
RNA Integrity Number (RIN):	1 (B.02.09)
Result Flagging Color:	
Result Flagging Label:	RIN:1

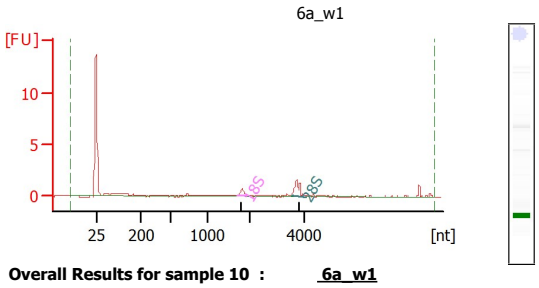

Overall Results for sample 10 : 6a_w1

RNA Area:	10.1
RNA Concentration:	40 pg/µl
rRNA Ratio [28s / 18s]:	2.8
RNA Integrity Number (RIN):	6.4 (B.02.09)
Result Flagging Color:	
Result Flagging Label:	RIN: 6.40

Fragment table for sample 10 : 6a_w1

Name	Start Size [nt]	End Size [nt]	Area	% of total Area
18S	1,722	1,934	0.8	7.9
28S	3,545	4,090	2.3	22.4

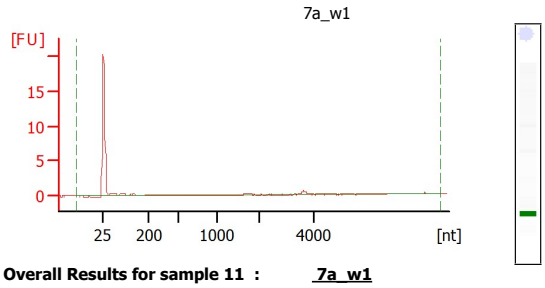

Overall Results for sample 11 : 7a_w1

RNA Area:	6.1
RNA Concentration:	24 pg/µl
rRNA Ratio [28s / 18s]:	0.0
RNA Integrity Number (RIN):	1 (B.02.09)
Result Flagging Color:	
Result Flagging Label:	RIN:1

Assay Class: Eukaryote Total RNA Pico
Data Path: C:\...Eukaryote Total RNA Pico_DE13701230_2018-10-16_10-08-33.xad

Created: 10/16/2018 10:08:32 AM
Modified: 10/16/2018 10:30:35 AM

Gel Image

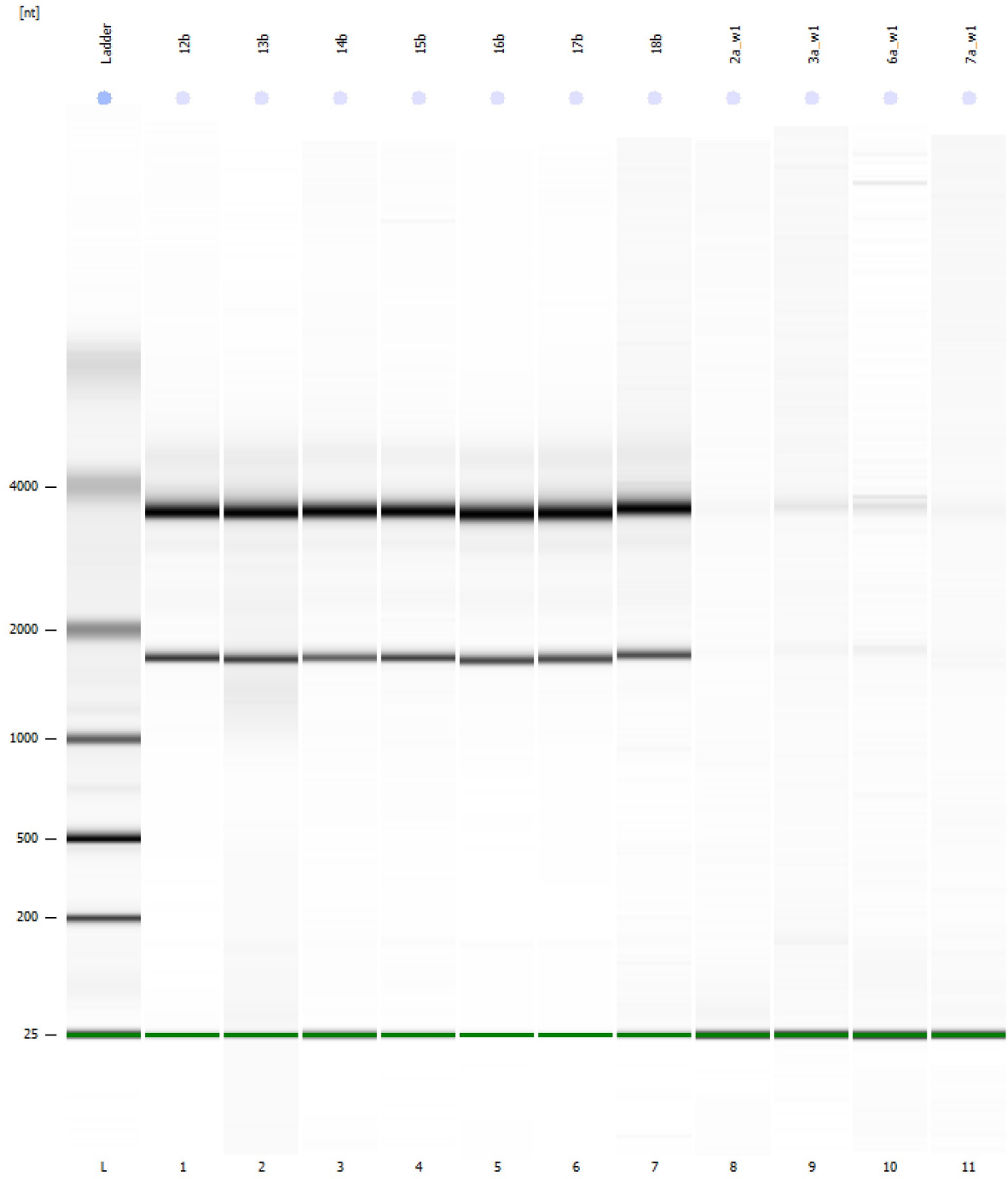

Eidesstattliche Versicherung

Ich versichere an Eides Statt, dass die Dissertation von mir selbständig und ohne unzulässige fremde Hilfe unter Beachtung der „Grundsätze zur Sicherung guter wissenschaftlicher Praxis an der Heinrich-Heine-Universität Düsseldorf“ erstellt worden ist.

Ort, Datum	Unterschrift